University of Bath

PHD

Optical and magneto-optical studies of wide-bandgap semiconductors

Griffin, Ivan John

Award date:
2000

Awarding institution:
University of Bath

Link to publication

Alternative formats
If you require this document in an alternative format, please contact:
openaccess@bath.ac.uk

Copyright of this thesis rests with the author. Access is subject to the above licence, if given. If no licence is specified above, original content in this thesis is licensed under the terms of the Creative Commons Attribution-NonCommercial 4.0 International (CC BY-NC-ND 4.0) Licence (https://creativecommons.org/licenses/by-nc-nd/4.0/). Any third-party copyright material present remains the property of its respective owner(s) and is licensed under its existing terms.

Take down policy
If you consider content within Bath's Research Portal to be in breach of UK law, please contact: openaccess@bath.ac.uk with the details. Your claim will be investigated and, where appropriate, the item will be removed from public view as soon as possible.

Download date: 05. May. 2023

Optical and magneto-optical studies of wide-bandgap semiconductors

submitted by Ivan John Griffin
for the degree of PhD
of the University of Bath
2000

This thesis may be made available for consultation within
the University Library and may be photocopied or lent to other libraries
for the purpose of consultation.

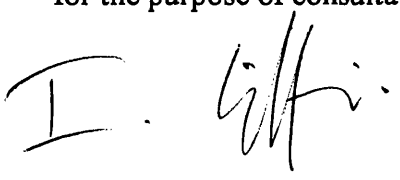

COPYRIGHT

Attention is drawn to the fact that copyright of this thesis rests with its author.
This copy of the thesis has been supplied on condition that anyone who consults
it is understood to recognize that its copyright rests with its author and that no
quotation from the thesis and no information derived from it may be published
without the prior written consent of the author.

UMI Number: U133281

All rights reserved

INFORMATION TO ALL USERS
The quality of this reproduction is dependent upon the quality of the copy submitted.

In the unlikely event that the author did not send a complete manuscript
and there are missing pages, these will be noted. Also, if material had to be removed,
a note will indicate the deletion.

UMI U133281
Published by ProQuest LLC 2013. Copyright in the Dissertation held by the Author.
Microform Edition © ProQuest LLC.
All rights reserved. This work is protected against
unauthorized copying under Title 17, United States Code.

ProQuest LLC
789 East Eisenhower Parkway
P.O. Box 1346
Ann Arbor, MI 48106-1346

UNIVERSITY OF BATH
LIBRARY
45 2 0 JUN 2001
PHD

to my family and Fong

Contents

Abstract

The nature of excitonic localisation in binary, ternary and quaternary wide-bandgap II-VI and III-V semiconductor alloys has been investigated using photoluminescence, resonant vibrational Raman scattering and spin-flip Raman scattering spectroscopies. Despite the importance of wide-bandgap alloys in optoelectronic applications, details of their microstructure, doping and bandstructure remain incompletely understood. In this study doping and compensation issues have been examined in the binary alloy ZnSe and the magnetic field dependent behaviour of electrons and holes bound to neutral impurity centres has been established. In ternary alloys the sensitivity of the hole to strain was exploited to identify unambiguously simultaneously observed electron and hole signals. Modelling the anisotropic hole dependence on the magnetic field direction enabled the residual strain in lattice-matched epilayers to be precisely determined, together with impurity related bandstructure parameters. The $k \cdot p$ approximation was applied successfully to the alloy systems and employed throughout the study in the interpretation of the spectroscopic results, thus providing an important test of the bandstructure theory. The predicted compositional dependence of the electron gyromagnetic ratio was satisfactory, enabling discrimination between different sets of bandstructure parameters published in the literature. However, as with other semiconductors the hole dependence proved more problematic. Magneto-optical measurements revealed evidence of excitons weakly localised by potential fluctuations. Modelling these results with a suitable Hamiltonian enabled the electron-hole exchange interaction to be determined. Significantly, analogous results were obtained in both ZnMgSSe and AlGaInP quaternary alloy systems, inferring that the behaviour is a general feature of disordered alloys. Further, in MBE-grown AlGaInP the exchange splitting was found to be linearly dependent on the degree of localisation, implying the existence of an excitonic mobility edge. A simple model accounting for this linear dependence required a two-dimensional confining potential; this may therefore be related to excitonic localisation at disc-like antiphase boundaries previously reported for AlGaInP, although further work is required to investigate this possibility.

Acknowledgements

First and foremost I would like to thank my supervisors Dr Daniel Wolverson and Professor J. John Davies for their thorough and patient supervision. I am deeply indebted to Mohamed Emam-Ismail who was a stalwart in troubled times and who began the phosphide work that I continued, contributing to this thesis the angle dependent data for the epilayer specimen with substrate removed. I am also extremely grateful to Oleg Karimov for his contribution to the high field measurements on the ZnSe:Li crystal, reported in appendix D. Many contributions of a more indirect nature were made by Catherine Orange, Chris Blades, Ingrid Petri, Peter Klar, Limei Chen, Diego Oriato and Jim Partridge. Finally, I wish to thank Bob Draper and Harry Bone for their excellent technical support on all matters practical.

This work was funded by the Engineering and Physical Sciences Research Council who also provided my research studentship. Additional personal support was provided by the Esther Parkin Fund.

Preface

Improvement in epitaxial growth techniques during the latter part of the last century heralded a renaissance in semiconductor physics. The advent of techniques such as Molecular Beam Epitaxy (MBE) and Metal Organic Vapour Phase Epitaxy (MOVPE), capable of delivering high purity, high quality crystalline epitaxial material with unprecedented control of interfaces and doping, precipitated rapid progress in both the industrial application and the fundamental physics of semiconductors. Previous to this most effort had been channelled into the understanding of binary semiconductors; however, it became clear that ternary and quaternary alloys had much to offer in terms of both practical device application and fundamental research. Wide-bandgap semiconductor alloys are of central importance to the development of light-emitting devices, in the visible spectral region, for optoelectronic application. This investigation is primarily focused on the nature of exciton localisation in wide-bandgap semiconductor alloys, which predominantly occurs due to the presence of neutral impurities centres or via potential fluctuation introduced by isovalent impurities. To achieve this, two wide-bandgap semiconductor material systems are investigated: ZnSe-based alloys, including ZnSe as a binary semiconductor, and phosphide-based alloys. Wide-bandgap semiconductors are attracting enormous technological interest both because of their potential use in devices capable of operating at high power level and high temperature and because of considerable technological importance of optical materials active in the visible spectral range. In the blue-green region II-VI ZnSe-based semiconductor alloys are among the most promising materials for fabrication of short wavelength devices, whilst phosphide-based alloys offer the largest direct bandgap of the III-V semiconductor and are capable of operating in the green-red region.

The electrical characteristics of a semiconductor have a direct bearing on device performance. The electrical properties of semiconductors are controlled by small amounts of impurity atoms introduced during growth or by post-growth treatment. These impurities form shallow impurity levels in the forbidden gap either just below the conduction-band or just above the valence-band. Thermal ionization of these centres promotes electrons or holes respectively into the conduction or valence - bands. These promoted charge carriers dramatically alter electrical conductivity, rendering semi-insulating material into either majority electron or hole carrier, respectively denoted n or p-type. In recent years controlled carrier concentrations in

the range 10^{15} to 10^{19} cm^{-3} have readily been achieved using MBE and MOVPE for optimal growth conditions. Materials containing both donor and acceptors are described as compensated. Compensation reduces the net affective carrier concentration. Compensating centres may be deliberately introduced, for example, in the production of high resistance material, may inadvertently be incorporated or self-compensation may take place. In an effort to better understand the doping process growers may intentionally introduce compensating centres, this is known as co-doping, to assist in the study of compensation. Compensation is an important issue in semiconductor physics and occurs to a lesser or greater extent in all the materials investigated in this thesis.

High quality binary material is characterized by narrow excitonic features, just beneath the fundamental band-edge. Among the wide-bandgap II-VI materials ZnSe has been one of the most extensively studied in the past. However, difficulty in controlling the conductivity by doping with donor and acceptor impurities has presented a serious obstacle to the use of ZnSe in commercially viable devices. ZnSe has been beset by compensation difficulties. Donor self-compensation was an early issue, however, this problem was largely resolved with the introduction of MBE and MOVPE growth techniques, which feature low-temperature non-equilibrium growth. As a result n-type doping has reached acceptable levels for device fabrication, however, p-type doping remains problematic. Of the potential candidates for p-type dopants in ZnSe only nitrogen has yielded sufficient doping levels for utilization in laser technology. However, this is not without difficulty, since the effective nitrogen acceptor concentration saturates due to an efficient self-compensation process. The limited success of the alternative p-type dopants is not fully understood.

Alloys offer a tunable range of bandgaps, coupled with the ability of lattice matching to commercially viable semiconductor substrates. These properties are extremely desirable for device application. In comparison to binary semiconductors alloys have received much less attention and little is known about the compositional dependence of their fundamental parameters. The behaviour of the alloys differs significantly from that of their binary constituents. The presence of isovalent impurities drastically changes the radiative recombination processes, resulting in a pronounced broadening of the excitonic emission bands observed in the luminescence spectra and the smearing of the band-edge density of states. These phenomena have been attributed to the radiative recombination of excitons localized by potential fluctuations caused

by compositional variations. A further departure is the propensity of alloys to exhibit spontaneous long and short-range order. The properties of ordered systems are of fundamental interest and also have important consequences on device performance. Long-range ordering reduces the bandgap and therefore must be avoided in the production of the shortest wavelength devices. Furthermore, partial ordering results in structural inhomogeneities which has a detrimental effect on device performance. Conversely, long-range ordering offers the attractive possibility of producing herterostructures without changing the composition during growth and the introduction of polarization anisotropy, that results from the reduced symmetry of the naturally formed superlattices, may lead to polarization sensitive optical devices. The phenomenon of short-range ordering has received little attention and its effects on the alloy bandstructure is not well understood.

Ultimately, the materials examined will form integral parts of functional devices. It is therefore essential to have some familiarity with the fundamentals of optical device operation. Material and physical requirements impose stringent restrictions on the fabrication of semiconductor devices. Unlike conventional lasers, in which the transitions occur between discrete energy levels, optical transitions within semiconductor lasers are primarily determined by the band properties of the material. A semiconductor laser is, in essence, a p-n junction diode in which optical radiation is produced by the injection of minority carriers into an active region, where radiative recombination takes place. The emitted light is confined and guided by the structure of the junction itself, which functions as a dielectric waveguide. The fundamental requirements are for the use of direct bandgap semiconductors in which a sufficiently large number of minority carriers can be generated, such that the number of stimulated photons exceeds the number absorbed and optical gain occurs. Furthermore, since the frequency of emission is determined by the bandgap of the active region a semiconductor must be chosen that matches the desired operating frequency required for the device. In practice structured devices greatly improve device performance. The most common configuration is that of the double heterostructure laser, in which a thin layer of narrower bandgap material is sandwiched between a wider bandgap material. The inner layer forms the active region, whilst the outer layers provide the confining or cladding layer. The heterostructure laser has a low threshold current density at room temperature, because of the carrier confinement provided by the energy barriers of the higher bandgap

semiconductors surrounding the active region, and the optical confinement provided by the abrupt reduction of the refractive index outside the active region provide efficient waveguiding. In addition the active region can be made smaller than the diffusion length of the injected carrier, thereby obtaining a more uniform gain. Further carrier confinement may be achieved by the incorporation of a quantum well into the active region. The structural integrity of the device is usually provided by a high quality binary semiconductor substrate. Upon this substrate successive epitaxial layers, with different alloy compositions and doping levels, are deposited to form the device. To avoid degradation in device performance, due to interface traps, it is essential that the epilayer and substrate are lattice matched. One of the most important problems connected with the growth of quantum well heterostructures is the structural disorder at the interfaces of the heterostructures, which includes interface roughness and interfacial alloying. Such structural disorder has significant adverse effects on the device performance.

Characterization of the material and device structures produced using epitaxial growth techniques provided essential information for both the refinement and deeper understanding of the growth techniques themselves, as well as, being instrumental in basic research and industrial process management. Optical characterization embracing techniques, such as: photoluminescence (PL), photoreflectivity (PR), photoluminescence excitation (PLE), vibrational Raman spectroscopy, optically detected magnetic resonance (ODMR), spin-flip Raman scattering (SFRS) and infrared (i.r) spectroscopy, provide nondestructive contactless measurements. These techniques have received wide application in the study of semiconductors and in the semiconductor industry. As previously stated this thesis is primarily concerned with the issue of excitonic localisation. Several methods have been employed to investigate exciton localisation, the most direct being PL and PLE. However, in many alloy systems the potential fluctuations responsible for localisation lead to considerable inhomogeneous broadening of the PL and PLE spectral features. Furthermore, in the study of excitonic systems magneto-optical measurements are very powerful, because in a magnetic field all the degenerate levels split into sublevels, each with its own characteristic oscillator strength and polarization. SFRS, the principal investigative technique employed in this work is capable of obtaining the important magnetic field dependent information, that is of direct relevance to the understanding of excitonic transitions, on a finer level than the inhomogeneously

broadened PL and PLE linewidth. SFRS has been applied with considerable success in binary materials and is particularly well suited to the study of excitonic features, since the scattering intensity is strongly enhanced in a small spectral range corresponding to the excitonic transition under investigation and direct measurement of the gyromagnetic ratio assists in the identification of the centre, thus enabling fundamental bandstructure parameters to be readily determined. Moreover, the technique is extremely sensitive to small strains and, in terms of optical spectroscopy, is in a unique position to determine the strain state of the alloy systems, for which the strain is expected to be small. Thus SFRS is expected to be well suited to the study of excitonic localisation in binary, ternary and quaternary alloy systems.

The thesis is constructed around the excitation probed, rather than material-by-material, since it is felt that this emphasizes the universality of the phenomena investigated, as opposed to highlighting specific differences between individual semiconductors. The thesis consists of five chapters followed by an overall conclusion. The first chapter introduces the theoretical background necessary to understand the magneto-optical measurements performed. The second chapter provides the reader with details of the experimental procedures and equipment. The experimental results and their interpretation are given in the last three chapters; dealing in turn with electron, hole and excitonic related excitation. Each of the experimental result chapters are subdivided into sections, which deal with pertinent material or excitation related issues; a summary concludes each section. Finally, there is an overall conclusion. Four appendices are included. The first two appendices give group tables and sample details. In the two remaining appendices additional experimental results are presented that could not be satisfactorily accommodated in the main body of the thesis. These are the vibrational Raman spectra for the quaternary phosphide-based material and an intriguing set of incomplete measurements on bulk lithium doped ZnSe crystals.

Chapter 1

The purpose of this first chapter is to introduce the key concepts in the physics of semiconductor solid solutions and to provide the necessary theoretical framework required to interpret the spectroscopic results presented in the remainder of the thesis. The chapter is divided into three subsections. The relevant crystal structures, microstructures and electronic bandstructure are discussed in the first section. In the second section the principal theoretical methods and interactions necessary for the interpretation of the magneto-optical measurements are identified and developed. In the final section Raman spectroscopy is discussed, with particular emphasis being placed on spin-flip Raman scattering and the appropriate selection rules for impurity bound excitons.

1.1.1 Structural properties

Most binary semiconductor compounds crystallize at ambient conditions in the zinc-blende structure. The zinc-blende structure, figure 1.1, consists of two interpenetrating face-centred cubic (fcc) sublattices displaced from each other by one-quarter body diagonal. The cations (metal atoms) are located on one sublattice, whilst the anions (non-metal atoms) occupy sites on the other sublattice. The local symmetry of each ion in the zinc-blende lattice is tetrahedral, that is, with the ion of one sublattice situated at the centre of a tetrahedron composed of four equidistant nearest neighbours from the other sublattice. The zinc-blende crystal is therefore invariant under the symmetry operations of the T_d point group, appendix A. Figure

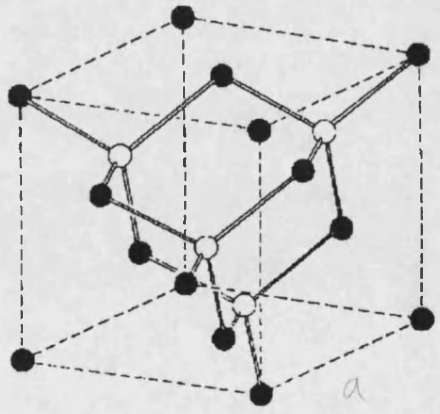

Figure 1.1 Zinc-blende crystal structure, where a is the lattice constant[1].

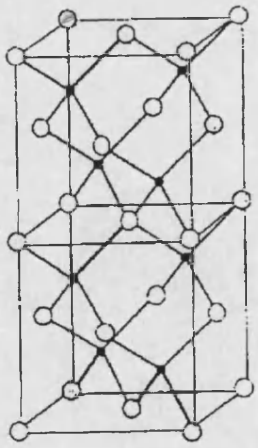

Figure 1.2 Crystal structure of CuPt-type ordered material[2]

1.2 shows the CuPt-type crystal structure, important in many ordered III-V alloys. The CuPt structure has the reduced point group symmetry C_{v3}.

Binary compounds alone offer only a limited range of material properties, such as, bandgaps and lattice parameters, see points in figure 1.3. For technological applications, however, properties intermediate to those offered by individual binary compounds are often sought. The traditional way of achieving these desired intermediate properties has been to form a "solid solution", composed from two or more binary compounds. These alloys have material parameters that are intermediate between those of the constituents, as indicated by the solid lines in figure 1.3.

The ternary and quaternary alloys under consideration in this study are often treated using the virtual crystal approximation (VCA). The VCA enables material properties to be interpolated according to a weighted average, of the form $\Phi_{alloy} = x\Phi_A + (1-x)\Phi_B$, where A and B are the binary end members, x is the concentration of A and Φ is a material parameter, such as, bandgap, atomic potential or lattice constant. The latter case is known as Vegard's law[3]. Results from extended X-ray absorption fine-structure spectroscopy (EXAFS)[4] reveal that, on a microscopic scale, bond lengths may deviate considerably from the average virtual crystal bond length. Further, in disordered GaInP it has been shown[5] that the substituted cations tend to retain their fcc arrangement with a VCA lattice constant, whilst the anions tend to arrange themselves in their local environment to minimize the strain caused by the bond distortions. However, measurements of the lattice constant using standard X-ray diffraction techniques indicate that Vegard's law is obeyed by most semiconductors alloys on a macroscopic scale[6]. The bandgap variation determined using VCA[7] consistently overestimates experimental measurements[8]. This is because the random nature of the alloy introduces new physics, not accounted for by the VCA. The variation in the bandgap energy with composition can be expressed:

$$E_0(x) = a + bx + cx(1 - x) \qquad (1.1)$$

where a is the measured bandgap at $x = 0$ and $(a + b)$ is the measured bandgap at $x = 1$. The bowing parameter c measures the deviation from linearity and represents the response of the bandstructure to the random chemical distribution and fluctuations in the lattice spacing. Alternative theoretical approaches, which address the issue of alloy disorder[5,8,9], tend to yield good agreement with experimental values of the bowing parameter.

In a perfect chemically random solid solution anions and cations occupy sites on their respective sublattices with no correlation to the occupation of other sites on the sublattice. For example, in $Ga_{0.5}In_{0.5}P$ the anion fcc sublattice is populated entirely by P atoms, whilst Ga and In atoms would be located on the cation sublattice randomly. This perfect chemical randomness implies the complete absence of long and short range order; however, it does introduce the existence of potential fluctuations, and hence band tailing[10]. Two classes of macroscopic deviations from randomness are widely observed in semiconductor alloys[11]: long and short range atomic ordering. The latter may result in clustering of like atoms and is driven by atomic size mismatch, but is reduced in epitaxially grown material due to the non-equilibrium growth conditions and the substrate strain[11]. Long-range atomic ordering is most prevalent in the III-V alloys examined in this thesis. These alloys exhibit CuPt-type ordering[12], figure 1.2. CuPt-type ordering is driven by surface reconstruction during the deposition of the epilayer, rather than bulk thermodynamic effects during growth[11]. Further discussion of ordering will take place in section 3.3.

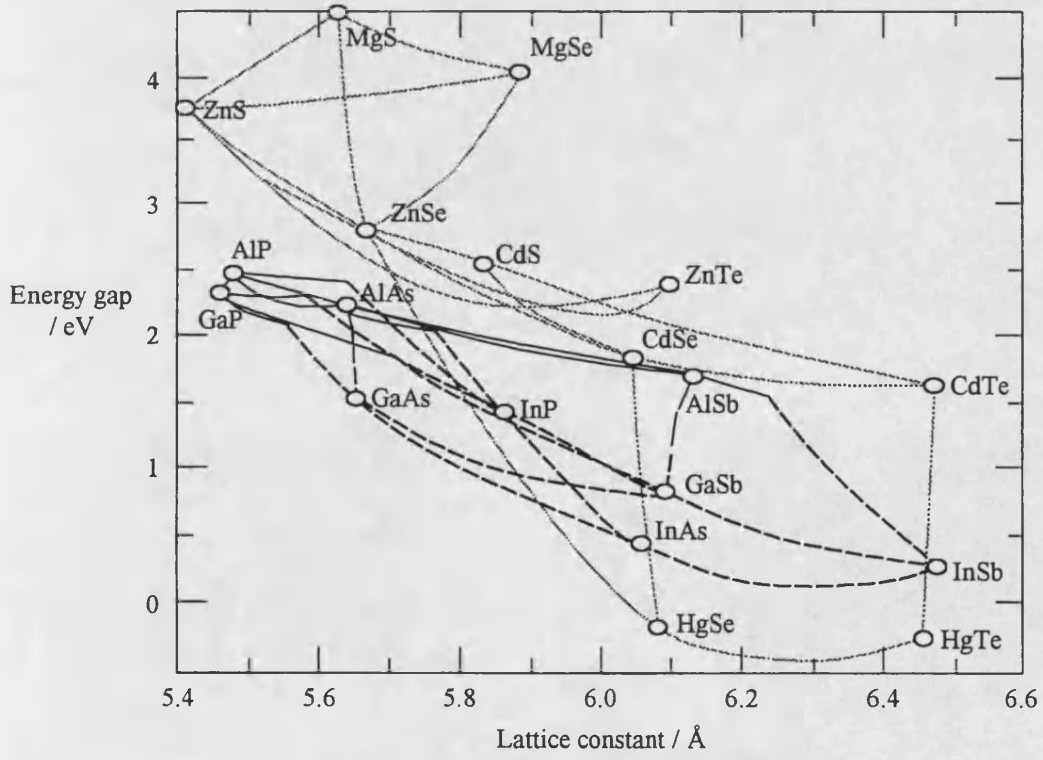

Figure 1.3 Plot of lattice parameter against bandgap energy at 300 K. Dashed and solid lines correspond to *X*-gap and direct gap transitions.

1.1.2 Electronic bandstructure

Excitations within the crystal are completely characterized by their dispersion relation $E(\mathbf{k})$. The electronic bandstructure of a semiconductor is principally determined by the symmetrised nearly-free electron wavefunctions, transforming according to the irreducible representations of the symmetry group of the crystal. However, the spin-orbit interaction and the ionic character of the constituents make significant contributions to the precise nature of the electronic bandstructure of individual

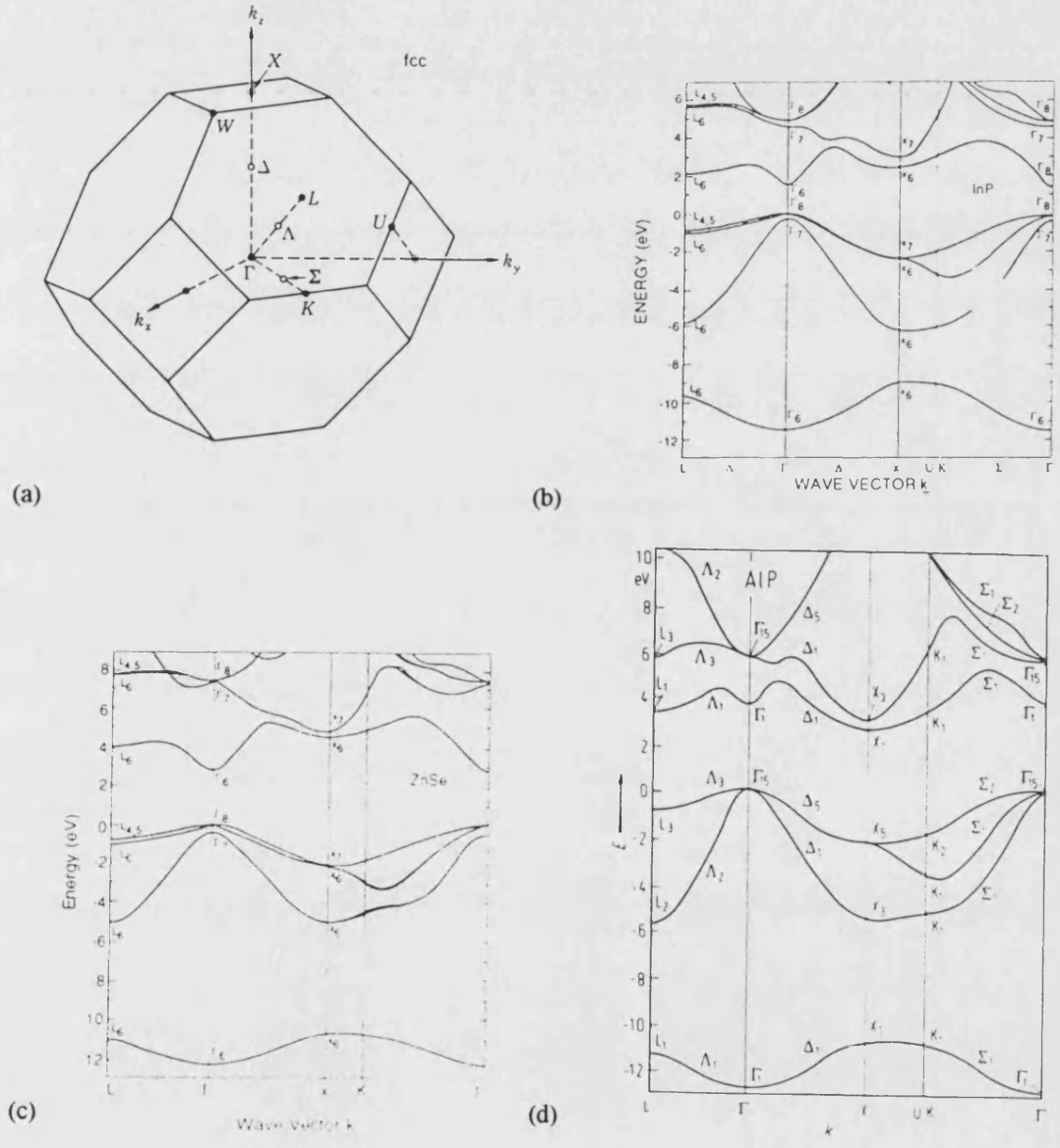

Figure 1.4 *a)* The first Brillouin zone of the fcc lattice[1]. The points of high symmetry are labelled by Roman letters and the lines connecting these points are labelled with Greek letters. The zone centre is always denoted by Γ. The calculated electronic bandstructures[13] for InP, ZnSe and AlP, including spin-orbit coupling, are shown respectively in figures *b*, *c* and *d*. The bandstructure diagrams are labelled using the double group notation, see Appendix A.

semiconductors. Calculated electronic bandstructures for InP, ZnSe and AlP are shown in figure 1.4, together with the first Brillouin zone of a zinc-blende structure.

The electronic configuration of the isolated atoms from which semiconductors are composed can be divided into core and valence electrons, with the outermost valence electrons in either s-type or p-type orbitals. In crystalline solids the discrete energy levels of isolated atoms form bands; however, these bands retain their s-like and p-like character. The uppermost valence-band is formed from p-like orbitals and is, therefore, triply degenerate (not including spin), with Γ_5 symmetry. This degeneracy is partially lifted by the spin-orbit interaction, which splits the valence-band into a doubly degenerate band with Γ_8 symmetry and a spin-split off band with Γ_7, similarly for the conduction-band. The degenerate Γ_8 valence-bands are characterized by two effective masses m^*, light and heavy hole, determined by the curvature of the bands:

$$\frac{1}{m^*} = \frac{1}{\hbar^2}\frac{d^2E}{dk^2} \tag{1.2}$$

Typically, the spin-orbit splitting is comparable to that of the constituent atoms of the semiconductor, scaling with their atomic number. In alloys it is predominantly determined by the anion, reflecting the larger influence of the anion on the p-like valence-band states, see table 1.1 below.

Usually, the lowest conduction-band is formed from s-like orbitals and has Γ_1 symmetry or in the double notation Γ_6, if spin is included. In practically all semiconductors the valence-band maxima are situated at the Γ point. If the conduction-band minimum is also situated at the Γ point, see figure 1.4 *b* and *c*, momentum can be conserved when light is absorbed or emitted, since the wavevector of the photon is small compared to that of the electron, and the probability of transition between the conduction and valence -bands is greatly enhanced. This is known as the k-selection rule, $\Delta k = 0$. The allowed transitions are then described as 'direct' or 'vertical'. All II-VI alloys have direct bandgap transitions and, with the exception of AlP, all of the III-V binary alloys examined in this thesis also have direct transitions. AlP is an 'indirect' material with the conduction-band minimum situated at the X point, see figure 1.4 *d*. Therefore, in order to conserve crystal momentum, phonons or other agents must participate in the scattering process, thus reducing the transition probability. This leads to a composition dependent direct-indirect transition in the phosphide-based alloys containing aluminium.

1.2.1 The $k \cdot p$ method

The spectroscopic techniques employed in this investigation probe excitations at the Γ point. The $k \cdot p$ method enables the bandstructure to be accurately determined about the high symmetry points and, naturally, being a perturbative method it works best for small values of k. The method requires only a small number of experimentally determined bandgaps and optical matrix elements and is therefore particularly useful for interpreting optical spectra. In addition, useful analytical expressions describing band dispersion, effective masses and effective g-factors may also be obtained.

Following reference [14] the one-electron Schrödinger equation in a periodic potential $V(r)$ is given by

$$\mathrm{H}\psi_{\mathrm{n}}(\mathbf{r}) = \left[\frac{\mathrm{p}^2}{2\mathrm{m}} + \mathrm{V}(\mathbf{r})\right]\psi_{\mathrm{n}}(\mathbf{r}) = \mathrm{E}_{\mathrm{n}}(\mathbf{k})\psi_{\mathrm{n}}(\mathbf{r}) \tag{1.3}$$

where the Bloch solution in the reduced zone scheme is

$$\psi_{nk}(\mathbf{r}) = u_{nk}(r)\, e^{(i\mathbf{k}.\mathbf{r})} \tag{1.4}$$

n is the band index, k is restricted to the first Brillouin zone, and u_{nk} has the periodicity of the lattice. Remembering that $p = -i\hbar\nabla$ and substituting ψ_{nk} into equation (1.3) an equation in u_{nk} is obtained in the form:

$$\mathrm{H}\psi_{nk}(\mathbf{r}) = \left[\frac{p^2}{2m} + \frac{\hbar\mathbf{k}\cdot\mathbf{p}}{m} + \frac{\hbar^2k^2}{2m} + V(\mathbf{r})\right]u_{nk}(\mathbf{r}) = E_n(\mathbf{k})u_{nk}(\mathbf{r}) \tag{1.5}$$

Once E_{n0} and u_{n0} are known the terms $\hbar\mathbf{k}\cdot\mathbf{p}/m$ and $\hbar^2k^2/2m$ can be treated as perturbations in (1.5) using either degenerate or nondegenerate perturbation theory. The eigenfunctions u_{nk} and the eigenvalues E_{nk} at points neighbouring k_o can be expanded to typically second-order in k, in terms of the unperturbed wavefunctions u_{n0} and energies E_{n0} by treating the terms involving k in (1.5) as perturbations.

$$u_{nk} = u_{n0} + \frac{\hbar}{m}\sum_{n'\neq n}\frac{\langle u_{n0}|\mathbf{k}\cdot\mathbf{p}|u_{n'0}\rangle u_{n'0}}{E_{n0} - E_{n'0}} \tag{1.6}$$

and

$$E_n(k) = E_{n0} + \frac{\hbar^2}{2m}k^2 + \frac{\hbar^2}{m^2}\sum_{n'\neq n}\frac{\left|\langle u_{n0}|\mathbf{k}\cdot\mathbf{p}|u_{n'0}\rangle\right|^2}{E_{n0} - E_{n'0}} \tag{1.7}$$

For small values of k the energy E_{nk} can be expressed as

$$E_n(\mathbf{k}) = E_{n0} + \frac{\hbar^2k^2}{2m^*} \tag{1.8}$$

where m^* is the effective mass of the band. Comparing equations (1.7) and (1.8), the following expression for the effective mass is obtained:

$$\frac{1}{m^*} = \frac{1}{m} + \frac{2}{m^2 k^2} \sum_{n' \neq n} \frac{\left| \langle u_{n0} | \mathbf{k} \cdot \mathbf{p} | u_{n'0} \rangle \right|^2}{E_{n0} - E_{n'0}} \tag{1.9}$$

This expression can be used to calculate the effective mass of a nondegenerate band, such as, the conduction-band. The conduction-band effective mass m^*_c can be estimated[15] including contributions from only the nearest valence-bands

$$\frac{m_0}{m_c^*} = 1 + \frac{1}{3} \frac{E_p^2}{m_0} \left(\frac{2}{E_0} + \frac{1}{E_0 + \Delta_0} \right) \tag{1.10}$$

where the valence-band maximum is chosen to be the E = 0 eV point. The direct bandgap transition E_0 is between the Γ_8 valence-band, the Γ_6 conduction-band and the spin-orbit splitting Δ_0 is between the Γ_8 and Γ_7 the valence-bands, see figure 1.4, and E_p is the energy momentum matrix element, expressed in energy units. The bandstructure parameters are given in table 1.1 below. Similar analysis results in an analogous expression to (1.8) for the effective gyromagnetic ratio[16-18]

$$\frac{g_c}{g_0} = 1 + \frac{1}{im_0} \sum_{n' \neq n} \frac{\langle u_{n0} | k_x \cdot p_x | u_{n'0} \rangle \langle u_{n'0} | k_y \cdot p_y | u_{n0} \rangle - \langle u_{n0} | k_y \cdot p_y | u_{n'0} \rangle \langle u_{n'0} | k_x \cdot p_x | u_{n0} \rangle}{E_{n0} - E_{n'0}} \tag{1.11}$$

which yields the following three-band approximation of the effective g-factor[18]:

$$\frac{g_c}{g_0} = 1 - \frac{E_P}{3} \left(\frac{1}{E_0} - \frac{1}{E_0 + \Delta_0} \right) \tag{1.12}$$

where g_0(= 2.0023) is the gyromagnetic ratio for the free electron. This expression provides reasonable estimates for the g-value of ternary alloy $Ga_{0.52}In_{0.48}P$, 1.60, which compares favourably to the experimentally obtain 1.62 ± 0.005[19] and 1.66 ± 0.05[20], given the limited knowledge of their bandstructure parameters. However, greater accuracy can be achieved in describing ZnSe and ZnS, because of a better knowledge of their bandstructure parameters, using expression (1.13) below.

	ZnSe	ZnS	InP	GaP	AlP
E_0 / eV	2.82	3.78	1.43	2.87	3.63
Δ_0 / eV	0.42	0.074	0.108	0.08	0.07
E_p / eV	24.3	15.3	20.4	22.2	17.7
m_c^*	0.108	0.2	0.067(0.073)	0.12(0.15)	0.17(0.22)
g_c	1.26(1.12)[22]	1.95(1.89)[23]	1.33(1.20)[24]	1.86	1.94

Table 1.1 Low temperature bandstructure parameters[13,21]. The results of three-band $k \cdot p$ calculation for m_c^* and g_c obtained using expressions (1.10) and (1.12), the measured values are given in parenthesis.

The influence of the more remote bands can be accounted for by extending the previous analysis to a five-band third-order ***k·p*** approximation. This is done so using the following expression[25]:

$$\frac{g_c}{g_0} = \left[1 - \frac{E_P}{3}\left(\frac{1}{E_0} - \frac{1}{E_0 + \Delta_0}\right)\right] - \left[\frac{E_P'}{3}\left(-\frac{1}{E(\Gamma_8^c) - E_0} + \frac{1}{E(\Gamma_7^c) - E_0}\right) + C'\right] + \left[\frac{2}{9}\frac{\sqrt{E_P E_P'}\,\Delta^-}{E(\Gamma_7^c) - E_0}\left(\frac{1}{E_0} + \frac{2}{E_0 + \Delta_0}\right)\right] \quad (1.13)$$

The first term is derived from a three-band ***k·p*** approximation[18] in which only the mixing of the Γ_6^c conduction-band and the Γ_8^v and Γ_7^v valence-bands are considered. Subsequent refinements have led to the inclusion of the more remote Γ_8^c and Γ_7^c conduction-bands in a five-band model[17], resulting in the second term, and the introduction of the off-diagonal spin-orbit coupling term Δ^- arising through third-order perturbation, yielding the third term[25,26].

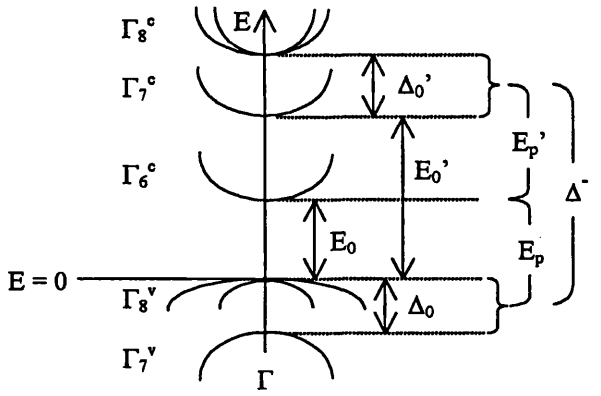

Figure 1.5 Schematic representation of the zone centre conduction and valence -band states required in the five-band ***k·p*** model, compare with figure 1.4 *b* and *c*. The notation is according to reference [27].

The above third-order model, equation (1.13), in conjunction with the parameters listed in table 1.2 predicts a value of g_{ZnSe} = 1.12, in good agreement with the experimentally determined value, see table 1.1. Therefore, the above expression is expected to be useful in the interpretation of SFRS spectra from II-VI alloys.

	E_0	E_p	E'_P	$E(\Gamma_7^c)$	$E(\Gamma_8^c)$	Δ_0	Δ^-
ZnSe	2.82	24.27	9.826	7.33	7.42	0.42	-0.046
ZnS	3.78	15.28	6.702	5.7	5.774	0.074	0.012

Table 1.2 Band parameters[28] for bulk ZnSe and ZnS. All parameters expressed in eV.

1.2.2 Spin-orbit interaction

The similarity of the valence-band wavefunctions at the zone centre to atomic p-wavefunctions may be utilized in order to symmetrise the valence-band states with spin-orbit coupling included. The orbital angular momentum $\boldsymbol{l}$ is coupled to the electron spin $\boldsymbol{s}$ via the spin-orbit interaction. Since the valence-band wavefunctions are p-like ($\boldsymbol{l}$=1) at the zone centre they are strongly influenced by the spin-orbit interaction. The wavefunctions X, Y and Z transform as atomic p-wavefunctions under the operations of the group O_h at the Γ point. The electron spin is 1/2 and the spin wavefunctions are denoted by α and β corresponding to spin-up and spin-down, respectively. The spin-orbit Hamiltonian may be expressed in terms of $\boldsymbol{l}$, $\boldsymbol{s}$ and a scaling parameter λ:

$$H_{so} = \lambda \boldsymbol{l}\cdot\boldsymbol{s} \tag{1.14}$$

The total angular momentum $J = l + s$, where the allowed values of J are 3/2 and 1/2. Expressing the wavefunctions in the J basis $|J, m_j\rangle$ enables the valence-band Hamiltonian to be diagonalised with the spin-orbit interaction included.

$$\left.\begin{aligned}
|3/2, 3/2\rangle &= 1/\sqrt{2}\,|(X+iY)\alpha\rangle \\
|3/2, 1/2\rangle &= 1/\sqrt{6}\,|(X+iY)\beta - 2Z\alpha\rangle \\
|3/2, -1/2\rangle &= 1/\sqrt{6}\,|(X-iY)\alpha + 2Z\beta\rangle \\
|3/2, -3/2\rangle &= -1/\sqrt{2}\,|(X-iY)\beta\rangle
\end{aligned}\right\} \Gamma_8 \tag{1.15}$$

$$\left.\begin{aligned}
|1/2, 1/2\rangle &= 1/\sqrt{3}\,|(X+iY)\beta + Z\alpha\rangle \\
|1/2, -1/2\rangle &= 1/\sqrt{3}\,|(X-iY)\alpha - Z\beta\rangle
\end{aligned}\right\} \Gamma_7 \tag{1.16}$$

The spin-orbit interaction splits the j = 3/2 (Γ_8) states from the j = 1/2 (Γ_7) valence-bands states. The spin-orbit splitting Δ_0 is equal to $3\lambda/2$. The conduction-band wavefunctions transform as atomic s-wavefunctions and may be represented as follows

$$|1/2, 1/2\rangle = |S\alpha\rangle \qquad |1/2, -1/2\rangle = i|S\beta\rangle \tag{1.17}$$

1.2.2 Valence-band dispersion

In order to understand the optical band-edge phenomena examined in this thesis it is essential to describe correctly both the conduction and valence -band minima. As seen in the previous section the conduction-band dispersion can successfully be accounted for using $\boldsymbol{k}\cdot\boldsymbol{p}$ theory. However, the application of this method to the warped energy surfaces of the degenerate valence-band presented a greater theoretical challenge. It transpires that the valence-band dispersion can successfully be described using an effective $\boldsymbol{k}\cdot\boldsymbol{p}$ Hamiltonian, involving five linearly independent parameters. These Luttinger parameters enable the effective masses of the valence-band to be determined through γ_1 and γ_2, and the warping of the valence-bands can be related to γ_3. A further two parameters, κ and q, are required to describe the interaction of the valence-band with the magnetic field, these will be discussed in section 1.2.5.

For large spin-orbit coupling the fourfold degenerate Γ_8 band-edge states may be considered separately from the spin-split off band Γ_7. The dispersion near the Γ point for the Γ_8 band is described by the Luttinger Hamiltonian[29]

$$H_L = \frac{1}{m}\left(\left(\gamma_1 + \frac{5\gamma_2}{2}\right)\frac{k^2}{2} - \gamma_2\sum_i (k_i^2 J_i^2) - 2\gamma_3 \sum_{\substack{ij \\ i\neq j}} \{k_i, k_j\}\{J_i, J_j\}\right) \tag{1.18}$$

where γ_1, γ_2 and γ_3 are the Kohn-Luttinger parameters, J is the angular momentum operator for $J = 3/2$ and $\{J_i,J_j\} = (J_iJ_j + J_jJ_i)/2$. The Luttinger Hamiltonian can be written in the 4x4 matrix form in the basis $(|3/2\rangle, |1/2\rangle, -|1/2\rangle, -|3/2\rangle)^T$:

$$H_L = -\frac{\hbar^2}{2m}\begin{bmatrix} F & H & R & 0 \\ H^* & G & 0 & R \\ R^* & 0 & G & -H \\ 0 & R^* & -H^* & F \end{bmatrix} \tag{1.19}$$

where F, G, H and R can be expressed in terms of γ_1, γ_2 and γ_3, such that:

$$\begin{aligned} F &= (\gamma_1+\gamma_2)(k_x^2+k_y^2)+(\gamma_1-2\gamma_2)k_z^2 \\ G &= (\gamma_1-\gamma_2)(k_x^2+k_y^2)+(\gamma_1+2\gamma_2)k_z^2 \\ H &= -2i\sqrt{3}\,\gamma_3(k_x-ik_y)k_z \\ R &= \sqrt{3}\left[(k_x^2-k_y^2)-2i\gamma_3 k_x k_y\right] \end{aligned} \tag{1.20}$$

1.2.4 Strain interaction

Strain directly affects the electronic bandstructure of semiconductors by altering the atomic spacing and thereby modifying the atomic potential felt by the electrons. Strain is invariably introduced into heteroepitaxial grown material, even in lattice matched systems. Since the spectroscopic results obtained from heteroepitaxial material are presented in this work, strain is expected to be of direct relevance in the interpretation of the spectra. It is therefore essential to understand in some detail the influence of strain on the conduction and valence -bands.

It has long since been established[30] that epitaxial growth of a material whose lattice constant is close, but not equal, to the lattice constant of the substrate material can result in the coherent incorporation of strain into the epilayer, such that, the in-plane lattice constant of the epilayer a_L matches that of the substrate a_s. This is known as pseudomorphic growth. Heteroepitaxial growth frequently leads of the incorporation of biaxial strain in the epilayer. The biaxial strain in zinc-blende material lowers the crystal symmetry from T_d to D_{2d}, altering the bandgap and splitting the light and heavy hole states. For cubic material with no torsion the biaxial strain in the plane of the epilayer $\varepsilon_{\|}$ is given by[31,32]

$$\varepsilon_{\|} = \varepsilon_{xx} = \varepsilon_{yy} = \frac{a_s - a_L}{a_L} \tag{1.21}$$

and with a free surface the strain $\varepsilon_{\perp}$ in the (001) growth direction is

$$\varepsilon_{\perp} = -\varepsilon_{\|} / \sigma \tag{1.22}$$

where σ is Poisson's ratio, equal to the ratio of the stiffness constants $c_{11}/2c_{12}$.

The effect of strain on the Γ_8 band extremum can be expressed by the Bir-Pikus strain Hamiltonian[33]

$$H_{BP} = -a\sum_i \varepsilon_{ii} - b\sum_i \varepsilon_{ii}(J_i^2 - \tfrac{1}{3}J^2) - 2/\sqrt{3}d\sum_{\substack{ij \\ i\neq j}} \varepsilon_{ij}\{J_i, J_j\} \tag{1.23}$$

with ε_{ij} the strain-tensor components (i,j = x,y,z). The hydrostatic deformation potential a, the shear deformation potentials b and d, correspond to strain-tensors with Γ_1, Γ_3 and Γ_5 symmetries, respectively. The matrix form of H_{BP} differs from that of the 4x4 H_L matrix in the replacement of F by f, G by g, H by h and R by r, such that[34]:

$$f = a(\varepsilon_{xx}+\varepsilon_{yy}+\varepsilon_{zz}) - b\left[\varepsilon_{zz} - \frac{1}{2}(\varepsilon_{xx}+\varepsilon_{yy})\right] \qquad g = a(\varepsilon_{xx}+\varepsilon_{yy}+\varepsilon_{zz}) + b\left[\varepsilon_{zz} - \frac{1}{2}(\varepsilon_{xx}+\varepsilon_{yy})\right]$$
$$h = -d(\varepsilon_{xz} - i\,\varepsilon_{yz}) \qquad r = \frac{\sqrt{3}}{2}b(\varepsilon_{yy} - \varepsilon_{xx}) + id\,\varepsilon_{xy} \tag{1.24}$$

The 4x4 strain Hamiltonian for the valence-band may be simplified considerably in the presence of a biaxial strain. The strain Hamiltonian may be rewritten in terms of the elastic stiffness constants c_{11} and c_{12} in the simplified form, in the $|J,m_j\rangle$ basis:

$$H=\begin{pmatrix} f' & 0 & 0 & 0 \\ 0 & g' & 0 & 0 \\ 0 & 0 & g' & 0 \\ 0 & 0 & 0 & f' \end{pmatrix} \tag{1.25}$$

where

$$f'=\left[2a\left(\frac{c_{11}-c_{12}}{c_{11}}\right)+b\left(\frac{c_{11}+2c_{12}}{c_{11}}\right)\right]\varepsilon_{\|} \qquad g'=\left[2a\left(\frac{c_{11}-c_{12}}{c_{11}}\right)-b\left(\frac{c_{11}+2c_{12}}{c_{11}}\right)\right]\varepsilon_{\|} \tag{1.26}$$

The hydrostatic deformation potential a of the in-plane strain alters the distance between the valence-band states and the conduction-band, whilst the shear deformation potential b separates the light-hole band (m_J = 1/2) from the heavy-hole band (m_J = 3/2) with respect to the centre of gravity of the Γ_8 band. In biaxial compression the bandgap increases and the heavy-hole states are the highest lying states, whilst in biaxial tension the bandgap is reduced and the light-hole states become the highest. The Γ_6 conduction-band strain Hamiltonian is given by

$$H_c=\begin{pmatrix} 2a\left(\frac{c_{11}-c_{12}}{c_{11}}\right)\varepsilon_{\|} & 0 \\ 0 & 2a\left(\frac{c_{11}-c_{12}}{c_{11}}\right)\varepsilon_{\|} \end{pmatrix} \tag{1.27}$$

indicating that the conduction-band states are not split by strain, but are raised in energy by compression and lowered by tension. Figure 1.6 shows schematically the effect of biaxial strain on the bandstructure at the Γ point for a zinc-blende type crystal.

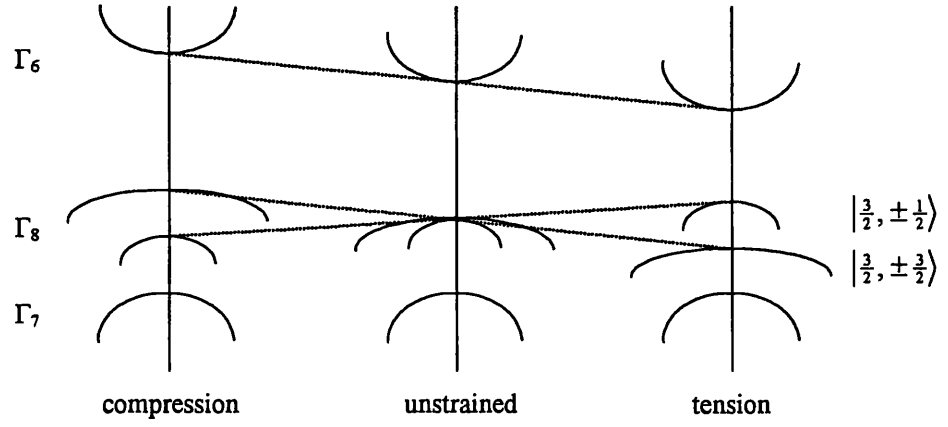

Figure 1.6 Schematic representation of the effects of in-plane biaxial strain on the electronic bandstructure at the Γ point of a zinc-blende semiconductor grown in the (001) direction.

Three factors determine the net biaxial strain experienced by the epilayer in heteroepitaxy: i) the lattice mismatch between the substrate and epilayer; ii) the difference in their respective coefficients of thermal expansion α; and iii) the thickness of the epilayer.

		GaAs	ZnSe	InP	GaP	AlP
α / x10^6 K^{-1}		5.8[35]	6.8[35]	4.75[36]	4.98[37]	4.5[38]
Lattice constant / Å		5.6533	5.6693	5.8687	5.4506	5.4672
Elastic stiffness	c_{11}	11.81	8.88	10.22	14.12	13.2
/10^{11} dyn cm^{-2}	c_{12}	5.32	5.27	5.76	6.253	6.30

Figure 1.3 Parameters required for strain calculations. Obtained from reference [13] unless otherwise stated. All values at 300 K.

In the case of a ZnSe epilayer on a GaAs substrate the lattice mismatch is comparatively small, see figure 1.3, and introduces a compressive biaxial strain of -0.28 % at room temperature. This is counteracted by a tensile strain induced by the difference in thermal contraction of the epilayer and substrate on cooling the sample from the growth temperature, since α_{ZnSe} is larger than α_{GaAs} the ZnSe epilayer contracts more. The lattice mismatch induced strain is constant until a certain critical thickness h_c is reached[39]. Beyond h_c misfit dislocations are formed, increasing in density, until the epilayer becomes completely relaxed, with only the thermally induced strain remaining. Thus, a ZnSe epilayer on a GaAs exhibits the full range of strain states, depending on the layer thickness and the temperature at which the measurements are performed. Thinner layers tend to be dominated by the compressive biaxial lattice mismatch strain and therefore the heavy-hole states are highest, whilst thicker layers are dominated by biaxial tensile strain induced due to the difference in thermal expansion coefficients and therefore the light-hole states are highest. Experimental findings concerning the strain states of ZnSe epilayers on GaAs substrates are reported in section 4.2.

The strain state of the AlGaInP material examined in this work is somewhat simpler to determine. The composition of the AlGaInP alloys were chosen to be latticed matched at the growth temperature and therefore the strain induced is due to the difference in the thermal expansion coefficients between the GaAs substrate and the AlGaInP epilayer. The GaAs substrate is expected to contract more than the AlGaInP

epilayer, producing a net biaxial compression of the AlGaInP epilayer. Thus, the heavy-hole band is most significant in terms of the optical characteristics of the phosphide-based material deposited on GaAs substrates.

1.2.5 Zeeman interaction

To interpret the magneto-optical spectra it is essential to understand the interaction of the conduction and valence -bands with the magnetic field. In the presence of a magnetic field B the spin degeneracy of the electronic bands are lifted. This is known as the Zeeman effect. For the s = 1/2 spin states of the Γ_6 conduction-band the Zeeman Hamiltonian is simply given by

$$H_c = g\mu_B \boldsymbol{s} \cdot \boldsymbol{B} \tag{1.27}$$

However, the spin Hamiltonian describing the fourfold degenerate Γ_8 valence-band for free holes is more complicated[29]

$$H_v = \mu_B\left(\kappa(J \cdot B) + q\sum_i J_i^3 B_i\right) \tag{1.28}$$

where μ_B is the Bohr magneton, κ and q are the dimensionless spin Hamiltonian parameter, the B_is are the components of the magnetic field and the J_is are the 4×4 spin matrices, with the z direction perpendicular to the growth plane, typically in the (001) direction. The coefficient q is small[33], therefore, to a first approximation H_v is independent of the magnetic field direction and the hole g-factor $g_h \sim -2\kappa$. To determine the Zeeman splitting of the degenerate acceptor impurity levels κ and q are replaced by their respective acceptor valence-band counterparts $\tilde{\kappa}$ and $\tilde{q}$. The constant $\tilde{q}$ is not necessarily small and the Zeeman splitting of the acceptor centre may become anisotropic with respect to the magnetic field direction. The anisotropic effects introduced by the strain Hamiltonian and by q will be examined in more detail in section 4.2.

1.2.6 Excitonic interaction

The promotion of an electron from a fully occupied valence-band to the conduction-band creates a vacant state in the valence-band. This vacant state may be treated as a positively charged quasi-particle, known as a hole. The electron and hole may be bound together through their mutual coulombic attraction, forming an electron-hole pair or exciton[40]. The exciton may be treated within the framework of the effective

mass approximation using the hydrogenic model. The surrounding medium significantly affects the exciton and is accounted for by the inclusion of the macroscopic dielectric constant ε and the effective masses of the electron m_e^* and hole m_h^*. The resultant exciton binding energy E_b is therefore considerably reduced from that of the hydrogenic Rydberg (R_y = 13.6 eV)[41]:

$$E_b = \frac{\mu}{m_0}\frac{1}{\varepsilon^2}\frac{R_y}{n^2} \tag{1.29}$$

here n is the principal quantum number and the reduced mass μ is given by $1/\mu = 1/m_e^* + 1/m_h^*$. The excitonic Bohr radius a^* is correspondingly increased by:

$$a^* = \frac{m_0}{\mu}\varepsilon a_0 \tag{1.30}$$

and may be as much as two orders of magnitude larger than the lattice constant; justifying the use of the macroscopic dielectric constant.

The cubic exchange Hamiltonian describing the eightfold degenerate 1s-exciton state, arising form the Γ_6 conduction-band and the Γ_8 valence-band, with a vanishingly small exciton translational wavevector is given by[42]:

$$H_{exch} = \delta_0 + \delta_1 J \cdot s + \delta_2 \sum_i s_i J_i^3 \tag{1.31}$$

where δ_0, δ_1 and δ_2 are coupling parameters. The magnitude of the exchange splitting δ_1 depends on the overlap between the electron and hole wavefunctions and, hence, increases as the intra-pair separation decreases. The angular momentum of the electron (s=1/2) and hole (J=3/2) combine to form states with total exciton angular momentum $F = s + J$, such that, $F = 1$ and $F = 2$. Writing the states in the exciton basis:

$$|F, m_F\rangle = \Sigma_i \left| m_j^i, m_s^i \right\rangle \tag{1.32}$$

This basis diagonalizes the δ_1 exchange interaction into an 8x8 matrix.

$$\left.\begin{aligned}
|2,2\rangle &= \left|\tfrac{3}{2},\tfrac{1}{2}\right\rangle \\
|2,1\rangle &= \tfrac{\sqrt{3}}{2}\left|\tfrac{1}{2},\tfrac{1}{2}\right\rangle + \tfrac{1}{2}\left|\tfrac{3}{2},-\tfrac{1}{2}\right\rangle \\
|2,0\rangle &= \tfrac{1}{\sqrt{2}}\left|\tfrac{1}{2},-\tfrac{1}{2}\right\rangle + \tfrac{1}{\sqrt{2}}\left|-\tfrac{1}{2},\tfrac{1}{2}\right\rangle \\
|2,-1\rangle &= \tfrac{\sqrt{3}}{2}\left|-\tfrac{1}{2},-\tfrac{1}{2}\right\rangle + \tfrac{1}{2}\left|-\tfrac{3}{2},\tfrac{1}{2}\right\rangle \\
|2,-2\rangle &= \left|-\tfrac{3}{2},-\tfrac{1}{2}\right\rangle
\end{aligned}\right\} \quad F = 2 \tag{1.33}$$

$$\left.\begin{aligned}
|1,1\rangle &= \tfrac{\sqrt{3}}{2}\left|\tfrac{3}{2},-\tfrac{1}{2}\right\rangle - \tfrac{1}{2}\left|\tfrac{1}{2},\tfrac{1}{2}\right\rangle \\
|1,0\rangle &= \tfrac{1}{\sqrt{2}}\left|\tfrac{1}{2},-\tfrac{1}{2}\right\rangle - \tfrac{1}{\sqrt{2}}\left|-\tfrac{1}{2},\tfrac{1}{2}\right\rangle \\
|1,-1\rangle &= -\tfrac{\sqrt{3}}{2}\left|-\tfrac{3}{2},\tfrac{1}{2}\right\rangle + \tfrac{1}{2}\left|-\tfrac{1}{2},-\tfrac{1}{2}\right\rangle
\end{aligned}\right\} \quad F = 1 \tag{1.34}$$

The electron and hole belong to the representations Γ_6 and Γ_8, respectively. The direct product $\Gamma_6 \otimes \Gamma_8$ gives $\Gamma_3 \oplus \Gamma_4 \oplus \Gamma_5$. The threefold degenerate $F = 1$ corresponds to Γ_5 representation, while $F = 2$ belongs to a reducible representation $\Gamma_3 \oplus \Gamma_4$. This reducible representation may be further split by the exchange interaction δ_2[42] or the crystal-field interaction[43].

The transition from the $F = 1$ states to the $F = 0$ ground states are electric-dipole allowed, whereas transitions from the $F = 2$ states are forbidden. However, these ideal selection rules breakdown in the presence of additional perturbations, such as the application of an external magnetic field or the introduction of impurities or defects. In the absence of an external magnetic field the oscillator strength of the $F = 2$ states is zero; however, the oscillator strength increases quadratically[42] with the application of the field, due to the mixing of the states, until saturation is reached. These selection rules are appropriate for describing weakly localised excitons and therefore have an important bearing on the interpretation of the spectroscopic results presented in chapter 5.

1.3.1 Raman scattering

Raman spectroscopy encompasses a variety of specialised techniques involving several different types of excitation, however, central to all is the inelastic interaction of light and matter. In this section the subject of Raman spectroscopy is initially introduced by the familiar case of vibrational excitation. The discussion will then be extended to the principal investigative technique employed in this study, namely, spin-flip Raman scattering (SFRS). Finally, appropriate selection rules will be determined for the spin-flip of carriers bound to neutral impurity centres.

Light incident on the surface of a semiconductor is almost entirely transmitted, reflected or absorbed. There is no change in the frequency of the scattered photons associated with these interactions. However, a minute fraction of the incident photons suffer inelastic interactions within the crystal. These interactions produce scattered photons whose frequencies differ slightly from those of the incident photons. These inelastic interactions of the crystal with light have become collectively known as Raman scattering.

The most commonly regarded form of Raman scattering involves the inelastic scattering of a photon by the creation or annihilation of a phonon[44,45]. This effect was discovered by C. V. Raman in 1928[46] and the phenomenon bears his name today. The effect is made possible due to the strain dependence of the electronic polarisability. Thermal vibrations of the atoms lead to the modulation of the electric field associated with their binding. This changes the local polarisation within the crystal and results in the frequency modulation of the incident light. Assuming the polarisability, η, associated with the phonon mode may be written in terms of the phonon amplitude, u, as a power series[1]:

$$\eta = \eta_0 + \eta_1 u + \eta_2 u^2 \tag{1.35}$$

For a phonon with amplitude variation $u(t) = u_0 \cos \Omega t$ and an electric field varying as $E(t) = E_0 \cos \omega t$, the electric-dipole moment is

$$\eta_1 E_0 u_0 \cos \omega t \cos \Omega t = \tfrac{1}{2} \eta_1 E_0 u_0 [\cos (\omega + \Omega)t + \cos (\omega - \Omega)t] \tag{1.36}$$

Inelastically scattered light can be emitted with a frequency of $\omega - \Omega$, known as Stokes shifted, or $\omega + \Omega$, known as anti-Stokes, corresponding to the emission or absorption of a phonon of frequency Ω, respectively. From this semi-classical picture emerge the phonon energy and momentum conservation rules:

$$\omega_s = \omega_i \pm \Omega \tag{1.37}$$

$$q_s = q_i \pm K$$

where ω_i and ω_s are the incident and scattered photon frequencies, q_i and q_s are the incident and scattered photon wavevectors and Ω and K are the phonon frequency and wavevector, respectively.

1.3.2 Spin-flip Raman scattering

Spin-flip Raman scattering involves the inelastic scattering of light by charge carriers. During the scattering process the spin orientation of the charge carrier is reversed. This may be illustrated by consideration of the spin-flip of an electron bound to a neutral donor, one of the most frequently observed processes, figure (1.7). The application of a magnetic field lifts the spin degeneracy of the conduction-band. An electron is optically excited to an intermediate excitonic state and returns to the donor ground state with the opposite spin. The resultant change in angular momentum is carried away by the photon.

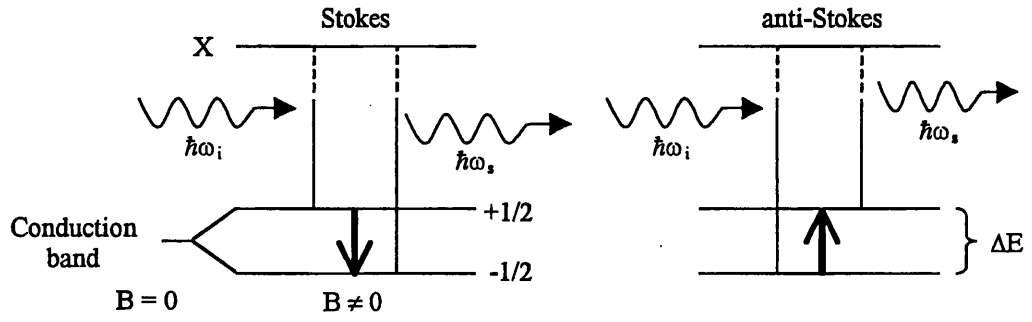

Figure 1.7 Electron Stokes and anti-Stokes spin-flip processes via an intermediate excitonic state X. The orientation of the electron spin is indicated by the arrow and the incident and scattered photon energies are $\hbar\omega_i$ and $\hbar\omega_s$, respectively.

The difference in energy between the incident ω_i and the scattered ω_s light, $\hbar(\omega_s - \omega_i)$, is a direct measure of the splitting between the states and, therefore, of the Zeeman energy. The effective gyromagnetic ratio is readily determined from

$$\Delta E = |g|\mu_B B \tag{1.38}$$

where $\mu_B \approx 0.4668$ cm^{-1}/ T and, more generally, g is the appropriate g-value for the electrons or holes. Thus, the splitting of the states, and hence the Raman shift, is directly proportional to the magnetic field strength B.

Fundamental to the success of the SFRS technique is the strong dependence of the scattering cross-section on the excitation energy, as this leads to high selectivity and strong enhancement of the signal intensity. The scattering cross-section for the SFRS process is given by[47]:

$$\frac{d\sigma}{d\Omega} = f^2 \left(\frac{e^2}{mc^2}\right)^2 \frac{\omega_s}{\omega_i} \frac{(\hbar\omega_i)^2}{(E_I - \hbar\omega_i)^2 + (\Gamma/2)^2} \tag{1.39}$$

here, f is the oscillator strength and Γ is a phenomenological damping term. From the form of equation (1.39) it is clear that strong resonant enhancement of the spin-flip signal takes place when $\hbar\omega_i$ approaches the energy E_I of the excited state and optimum enhancement is obtained when the excitation energy coincides precisely with the excited state on the centre under investigation, in practice to within 1 meV or less. The scattering intensity may be increase by several orders of magnitude at resonance. Exploitation of this resonant enhancement is the motivation for the use of tuneable excitation sources in the experiments, see section 2.4.

An example of a SFRS spectrum is shown in figure (1.8) below. The figure shows the electron SFRS in resonance with a neutral donor bound exciton from an MOVPE-grown ZnSe epilayer at 6 Tesla. The central feature is due to the elastically scattered

laser light, whilst the features shifted from the laser line by +3.2 and –3.2 cm^{-1} are the Stokes and anti-Stokes electron SFRS signals, respectively. The g-value determined, in accordance with equation (1.38), from the magnetic field dependence, figure 1.9, is 1.12 ± 0.03.

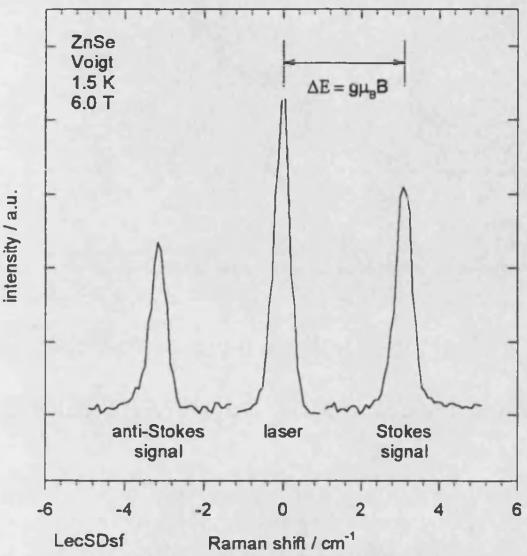

Figure 1.8 Electron SFRS in resonance with donor centre from an MOVPE-grown ZnSe epilayer. The central feature is due to elastically scattered laser light, symmetrically disposed about this line are the Stokes and anti-Stokes SFRS signals.

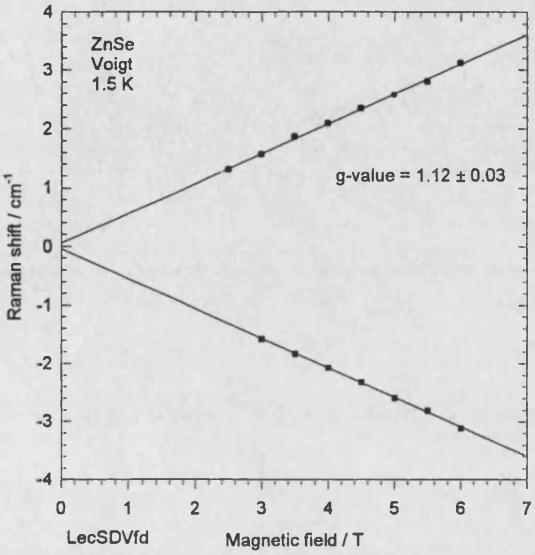

Figure 1.9 The magnetic field dependence of fitted Stokes(circles) and anti-Stokes(squares) signals. Effective g-factor determined from the gradient of the regression fit (solid line), using equation (1.34) is 1.12 ± 0.03.

As shown in section 1.2.1 the magnitude of the electron gyromagnetic ratio is related to the band parameters and may be determined through $\boldsymbol{k \cdot p}$ perturbation theory. However, the three-band term alone has not proved satisfactory in the determination of gyromagnetic ratio for wide-bandgap II-VI alloys[28]. The three-band term yields a g-value for the ZnSe conduction-band of g = 1.26, according to table 1.1, which differs from the measured g-value by more than the experimental uncertainty. Therefore, as expected it was essential to consider the contribution from the more remote bands for the wide-bandgap material ZnSe.

SFRS has been successfully applied to the study of excitonic feature binary material. The technique has been of particular importance in contributing to the understanding of doping issues, especially in the case of p-type ZnSe, where the technique has been used to study the compensation process that limits the effective acceptor concentration, it was instrumental in the identification of new defect states[48] and the determination of the strain-spin Hamiltonian parameters[49]. SFRS has also been applied to the study of excitons localised at defects, interface roughness and layer

thickness fluctuations. Examples include: i) epitaxial ZnSSe and ZnMgSe[28]; ii) studies of g-factors, fundamental scattering mechanisms and selection rules for acceptors-bound excitons and excitons localised by interface disorder in GaAs/AlGaAs quantum wells[50,51]; iii) the study of electron g-factors anisotropy in ZnSSe/ZnSe quantum wells[52]; iv) the determination of the electron g-factor anisotropy and its variation with quantum well thickness in the GaAs/AlAs system[53]; v) a systematic study of electron, hole and exciton g-factors for quantum well excitons and different barrier materials in CdTe/CdMgTe quantum wells[27]; vi) the study of monolayer insertions in CdSe/ZnSe[54,55]; vii) excitonic features in quantum dots formed by Stranski-Krastanov growth in InAs/GaAs[56] and InP/InGaP[19]; and viii) strongly confined excitons at CdS dots in the CdS/glass system[57]. Thus, SFRS has a proven ability in the investigation of excitonic features in binary and structured materials; it should therefore be well suited to the study of excitonic features in alloys discussed in this thesis.

1.3.3 SFRS selection rules

The interband transition probability is the product of an optical matrix element and the density of states. The interband transition rate is given by Fermi's golden rule:

$$W = \frac{2\pi}{\hbar} \sum_{f,i} \left| \langle f | H_I | i \rangle \right|^2 \delta\left(E_f - E_i + \hbar\omega\right) \tag{1.40}$$

where f and i are the transition final and initial states with energies E_f and E_i, respectively, and H_I is the interaction Hamiltonian. It is the matrix element H_I that determines whether a transition is allowed or forbidden. Thus, the selection rules for optical transitions can be derived by evaluation of the appropriate electric-dipole matrix elements. Within the electric-dipole approximation the momentum matrix element between the band-edge wavefunctions equations (1.15) and (1.17) is given by:

$$\left| \langle f | \hat{\mathbf{e}} \cdot \mathbf{p} | i \rangle \right|^2 \tag{1.41}$$

By symmetry the only non-vanishing combinations of the spatial part of the matrix element by are

$$\langle X | p_x | S \rangle = \langle Y | p_y | S \rangle = \langle Z | p_z | S \rangle \tag{1.42}$$

From this and the orthogonality of the spin functions a selection rule for component of the angular momentum in the direction of the magnetic field m is obtained. For

polarizations parallel to the magnetic field, $\Delta m = 0$ and, for polarizations perpendicular to the magnetic field, $\Delta m = \pm 1$.

In the presence of a magnetic field light with π-polarization does not change the component of angular momentum along the magnetic field direction of the electronic states, whereas light of σ-polarization changes the component of angular momentum along the direction of the magnetic field by $\pm$ 1. The momentum of the particles must be conserved in the scattering process. The spin components along the magnetic field direction of the electrons in the initial and final states differ by 1, thus the polarization state of the incident and scattered light must be different, either π and σ or σ and π.

The selection rules for bound excitonic spin-flip may now be determined. Excitons bound to either neutral donors (D^0X) or acceptors (A^0X) form an intermediate state in the scattering process. In SFRS at D^0X, the spins of the two electrons are aligned anti-parallel, so the spin levels of the excited state correspond to those of the hole of the exciton. Conversely for A^0X SFRS it is the holes that spin pair and the excited excitonic states are those of the electron. The allowed optical transitions are given in figure 1.10. Stokes scattering for D^0X occurs via transitions $2 \rightarrow 4$ and $3 \rightarrow 5$, whilst for A^0X it is $2 \rightarrow 3$ and $4 \rightarrow 5$. The order of the transitions is reversed for anti-Stokes scattering.

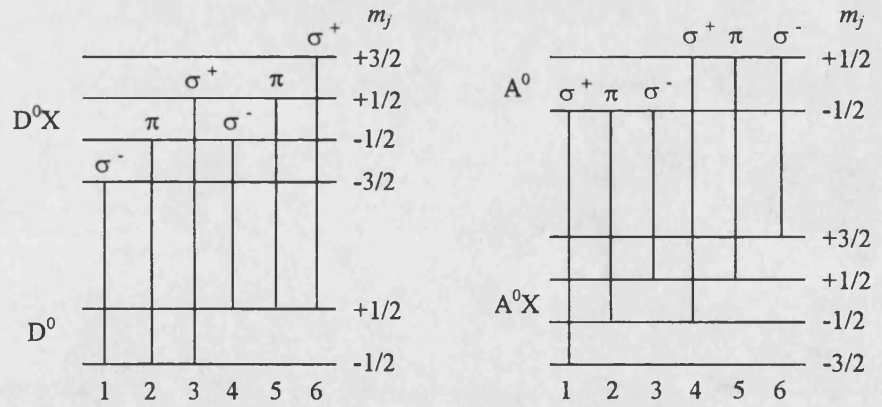

Figure 1.10 Allowed optical transitions and polarization states (σ and π) for neutral donor and acceptor bound excitons in the presence of a finite magnetic field.

1.4 References

[1] C. Kittel *'Introduction to Solid State Physics'* (J. Wiley and Sons, New York, 1986)

[2] F. Scholz, C. Geng. M. Burkard, H.-P. Gauffel, H. Schweizer, R. Wirth, A. Moritz and A. Hangleteiter, Physica E **2** (1998) 8

[3] L. Vegard, Z. Phys. **5** (1921) 17

[4] Jr. J.C. Mikkelson and J.B. Boyce, Phys. Rev. Lett. **49** (1982) 1412

[5] A.-B. Chen and A. Sher, *'Semiconductor Alloys: Physics and Materials Engineering'*, (Plenum Press, New York and London 1995)

[6] S. Adachi, *'Physical Properties of III-V Semiconductor Compounds'*, (J. Wiley and Sons, New York, 1992)

[7] J.A.Van Vechten and T.K. Bergstresser, Phys. Rev. B **1** (1970) 3351

[8] S.-H. Wei and A. Zunger, Phys. Rev. B **39** (1988) 3279

[9] J.E. Bernard and A. Zunger, Phys. Rev. B **34** (1986) 5992

[10] S.D. Baranovskii and A.L. Efros, Sov. Phys. Semicond. **12** (1978) 1328

[11] A. Zunger and S. Mahajan, Atomic Ordering and Phase Separation in Epitaxial III-V Alloys in Handbook on Semiconductors, Eds. T. Moss and S. Mahajan, vol. 3, ch. 19, (Elsevier Science, Amsterdam, 1994)

[12] A. Gomyo, T. Suzuki and S. Iijima, Phys. Rev. Lett. **60** (1988) 2645

[13] Landolt-Börnstein 1982 *'Numerical Data and Functional Relationships in Science and Technology'*, (Springer)

[14] P. Y. Yu and M. Cardona *'Fundamentals of Semiconductors'* (Springer-Verlag, Berlin, 1996)

[15] E. O. Kane J. Phys. Chem. Solids **1** (1957) 249

[16] M. Cardona, J. Phys. Chem. Solids **24** (1963) 1543

[17] C. Hermann and C. Weisbuch, Phys. Rev. B **15** (1977) 823

[18] L. M. Roth, B. Lax and S. Zwerdling Phys. Rev. **114** (1959) 90

[19] A.A. Sirenko, T. Ruf, A. Kurtenbach and K. Eberl, in Physics of Semiconductors, Wurzburg 1996, Ed. M. Scheffler and R. Zimmermann, (World Scientific, Singapore 1996) p. 1385

[20] I.J. Griffin, D. Wolverson, J.J. Davies, M. Emam-Ismail, J. Heffernan, A.H. Kean, S.W. Bland and G. Duggan, Semicond. Sci. Technol. **15** (2000) to be published

[21] A.T. Meney, A.D. Prins, A.F. Phillips, J.L. Sly, E.P. O'Reilly, D.J. Dunstan, and A.R. Adams and A. Valster, IEEE J. Quantum Electronics **1** (1995) 1077

[22] J. E. Nicholls, J. J. Davies, N. R. J. Poolton, R. Mach and G. O. Müller, J. Phys. C: Sol. Stat. Phys. **18** (1985) 455

[23] J.R. James, B. C. Cavenett, J. E. Nicholls, J. J. Davies and D. J. Dunstan, J. Lumin. **12/13** 447 1976)

[24] M. Oestreich, S. Hallstein, A.P.Herberle, K. Eberl, E. Bauser and W.W. Ruhle, Phys. Rev. B **53** (1996) 7911

[25] M. Willatzen, M. Cardona and N. E. Christensen, Phys. Rev. B **51** (1995) 17992

[26] M. Cardona, Phys. Rev. B **34** (1986) 7402

[27] A. A. Sirenko, T. Ruf, M. Cardona, D. R. Yakovlev, W. Ossau, A. Waag and G. Landwehr, Phys. Rev. B **56** (1997) 2114

[28] D. Wolverson, J.J. Davies, C. Orange, K. Ogata, Sz. Fujita, Sg. Fujita, K. Nakano, H. Okuyama, S. Itoh, B. Jobst and D. Hommel, Phys. Rev. B **60** (1999) 13555

[29] J. M. Luttinger Phys. Rev. **102** (1956) 1030

[30] F.C. Frank and J.H. van der Merwe Proc. Roy. Soc. A **198** 205 (1949)

[31] K. Ohkawa, T. Mitsuyu and O. Yamazaki, Phys. Rev. B **38** (1988) 12465

[32] J. Gutowski, N. Presser and G. Kudlek, Phys. Stat. Sol. (a) **120** (1990) 11

[33] G. L. Bir and G. E. Pikus, '*Symmetry and Strain Induced Effects in Semiconductors*' (J. Wiley and Sons, New York, 1974)

[34] J. Singh, '*Physics of Semiconductors and their Heterostructures*' (McGraw-Hill, Singapore, 1993)

[35] N. Shibata, A. Ohki, S. Zembutsu and A. Katsui, Jpn. J. Appl. Phys. **27** (1988) L487

[36] K. Haruna, H. Maeta, K. Ohashi and T. Koike, J. Phys. C. **20** (1987) 5275

[37] K. Haruna, H. Maeta, K. Ohashi and T. Koike, J. Phys. C. **19** (1986) 5149

[38] H. G. Grimmeiss and B. Monemar, Phys. Stat. Sol. (a) **5** (1971) 109

[39] K. Wolf, S. Jilka, A. Rosenauer, G. Schütz, H. Stanzl, T. Reisinger and W. Gebhardt, Appl. Phys. **28** (1995) A120

[40] G.H. Wannier, Phys. Rev. **52** 191 (1937)

[41] D.L. Dexter and R.S. Knox, '*Excitons*' (Interscience Publishers 1965)

[42] K. Cho, S. Suga, W. Dreybrodt and F. Willmann Phys. Rev. B **11** (1975) 1512

[43] P.J. Dean and R.A. Faulkner, Phys. Rev. **185** (1969) 1064

[44] R. Loudon, Advan. Phys. **13** (1964) 423

[45] M. Cardona and G. Güntherodt, '*Topics in Applied Physics*' **50** Light Scattering in Solids II (Springer-Verlag, Berlin, 1982)

[46] C. V. Raman, Ind. J. Phys. **2** (1928) 619

[47] Y. Yafet, Phys. Rev. **152** (1966) 858

[48] C. Orange, B. Schlichtherle, D. Wolverson, J. J. Davies, T. Ruf, K. Ogata and Sg. Fujita, Phys. Rev. B **55** (1997) 1607

[49] D. Wolverson, P. J. Boyce, C. M. Townsley, B. Schlichtherle and J. J. Davies, J. Cryst. Growth **159** (1995) 229

[50] V.F. Sapega, M. Cardona, K. Ploog, E.L. Ivchenko and D.N. Mirlin, Phys. Rev. B **45** (1992) 4320

[51] V.F. Sapega, T. Ruf, M. Cardona K. Ploog, E.L. Ivchenko and D.N. Mirlin, Phys. Rev. B **50** (1994) 2510

[52] J.J. Davies, D. Wolverson, I.J. Griffin, O.Z. Karimov, C. Orange, D. Hommel and M. Behringer, Phys. Rev B **62** (2000) 10329

[53] A.A. Sirenko, T. Ruf, K. Eberl, , M. Cardona, A.A. Kiselev, E.L. Ivchenko and K. Ploog, in Proc 12th Int. Conf. Appl. High Magnetic Fields in Semicon. Phys., Wurzburg 1996, Ed. G. Landwehr and W. Ossau (World Scientific, Singapore 1997) p. 561

[54] O.Z. Karimov, D. Wolverson, J. J. Davies, T. Ruf and L.N. Tenishev, Phys. Stat. Sol.(a) **215** (1999) 373

[55] T. Ruf, O.Z. Karimov, D. Wolverson, J. J. Davies, A.N. Reznitsky, A.A. Klochikhin, S.Yu. Verbin, L.N. Tenishev, S.A. Permogorov and S.V. Ivanov, Physica B **273-274** (1999) 911

[56] A.A. Sirenko, T. Ruf, N.N. Ledentsov, A.Y. Egorov, P.S. Kop'ev, V.M. Ustinov and A.E. Zhukov, Sol. Stat. Comms.**97** (1996) 169

[57] A.A. Sirenko, V.I. Belitsky, T. Ruf, M. Cardona, A.I. Ekimov, C. Trallero-Giner, Phys. Rev. B **58** (1998) 2077

Chapter 2 – Experimental setup

The nature of SFRS imposes stringent requirements on the excitation source and detection system. In this chapter, details of the experimental Raman systems used in the undertaking of this work are given. In addition experimental details of the light analysis, angle resolved measurements, substrate removal, dyes and fitting procedure will also be discussed. Particularly pertinent to the investigation of wide-bandgap semiconductors examined in this thesis was a tuneable continuous-wave source with emission spanning, almost, the entire visible spectrum. To take full advantage of the dramatic enhancement effect that occurs when the laser is in resonance with selected optical transitions, as discussed in section 1.3.2, requires laser tuneability better than 0.3 meV. A specialized spectrometer with good stray light rejection is essential for observing Raman signals close to the laser line. Furthermore, low temperatures are required to avoid ionization of the centres under investigation and, since the Raman shift of the signal is often linearly dependent on the strength of the magnetic field and the intensity of some signals were field dependent, strong magnetic fields were also required.

2.1 Experimental system

All the requirements stipulated above were satisfied by the two experimental systems used during this investigation. The bulk of the spectra presented in this thesis were obtained using the system presently residing at the University of Bath, whilst the high field measurements were performed at the Max Planck Institute in Stuttgart.

A schematic view of the experimental system used in Bath for PL and SFRS studies is shown in figure 2.1. The system uses a split-coil superconducting magnet[1] in which the sample was immersed in superfluid helium at the nominal temperature of 1.5 K. The maximum field available was 6 Tesla. Continuous wave excitation in the visible region was provided by one of two dye lasers pumped by an argon-ion laser. The excitation light was passed through a polarizing element before being focused on the sample, over an area of about 0.25 mm^2. The light incident on the sample was in a quasi-backscattering geometry, see inset. Moderate excitation powers, 10 to 20 mW, were used to minimize sample heating, whilst ensuring a good signal-to-noise ratio. Light scattered by the sample was collected by a convex lens and was collimated into a parallel beam which passed through analysing elements before being focused on the entrance slit of the spectrometer.

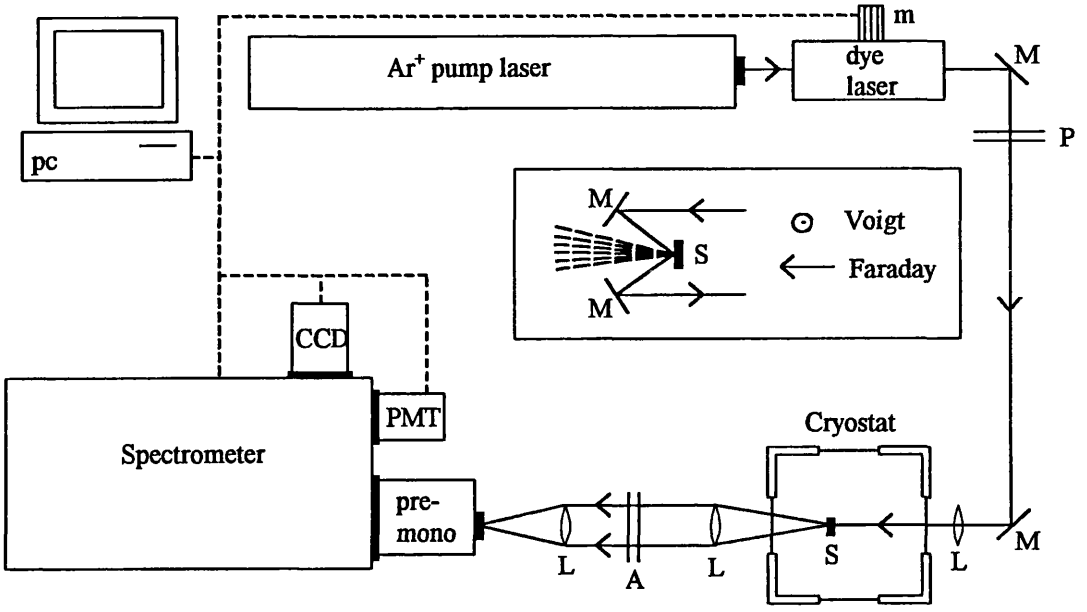

Figure 2.1 Schematic representation of the experimental set-up for the spin-flip Raman system used in Bath. The solid line indicates the beam path, the dashed line shows the data acquisition and device control system. The component labels are as follows: mirror M, polarizer P, sample S, analyzer A, motor m and lens L. The inset shows the back-scattering geometry set-up.

The triple grating spectrometer[2] consisted of two separately controllable stages; a subtractive double stage acting as a band pass filter and a dispersive stage. Scattered light from the sample was dispersed using a spectrometer with a 1800 lines per millimetre grating and a of focal length one metre and was subsequently detected using either a cooled charged-coupled device[3] (CCD) detector or a GaAs photomultiplier photon counting system. The limit of resolution of the CCD detector was determined by the pixel size and was ~0.5 cm^{-1} and 0.2 cm^{-1} respectively, in the blue and red spectral region. This could be improved to 0.3 cm^{-1} for wavelengths less than 450 nm if the second order diffracted light from the diffraction grating was used, with a consequent reduction of intensity by a factor of ten. For higher resolution studies the photomultiplier[4,5] was used. This yielded a detection resolution limit of 0.1 cm^{-1}. However, the ultimate resolution of the Bath system was determined by the dye laser linewidth of 0.3 cm^{-1}.

Spectral features as close as 2 cm^{-1} to the laser line were resolved. This was possible due to the strong resonant enhancement of the SFRS signals, yielding count rates of up to 10^4 photons per second for excitation powers of 10 to 20 mW, and good stray light rejection. Three factors contribute to the good stray light rejection achieved by the system. The M-shaped beam path backscattering arrangement directs most of the

elastically scattered light away from the spectrometer. The favourable selection rules allow the use of crossed polarising elements in Voigt geometry, which enable the Raman scattered light to be transmitted, whilst rejecting the laser light. The subtractive double stage acts as a band pass filter.

The Stuttgart system consists of a solenoid superconducting magnet capable of 14 T. The sample space was cooled by helium gas exchange, enabling temperatures of 5 K to be reached. The detection system constituted a double grating spectrometer and a conventional single-photon counting detector. The spectral resolution of the entire system was approximately 0.1 cm^{-1}.

2.2 Analysis of incident and scattered light

The laboratory axes are defined by *x*, *y* and *z*, for epilayers the normal to the crystallographic [001] direction was parallel to *z*, with *y* parallel to [110]. The laser beam was incident almost parallel to $-z$ and the emitted light was detected in the back-scattering direction, *z*. The magnetic field could be oriented either along *y* (Voigt geometry) or *z* (Faraday geometry).

As discussed in section 1.3.2 the spin-flip of an electron in a scattering process requires the angular momentum of the outgoing photon to differ by unity from the incoming one. The selection rules are satisfied if the incoming light is σ polarized and the outgoing light is π polarized. This process is described by the notation $z(\pi,\sigma)\bar{z}$[6], where the first and last symbols represent the direction of the incoming and scattered photons with respect to the laboratory coordinates, whilst the symbols within the parenthesis on the left and right hand sides inside indicate the sense of polarization of the electric field vector of the incident and scattered light. For electron spin-flip the incident light was passed through a half-wave plate and then a polarizer to ensure that it was linearly polarized in either σ(x) or π(y) polarization. The scattered light was passed through an analyser which transmitted linearly polarized light. For holes with their greater angular momentum and the possibility of mixing between heavy and light hole states, the selection rules are more complicated[7]. In Faraday geometry the incident and scattered light passed through quarter-wave plates to convert between linear and circular polarizations.

Note that according to the selection rules the circular polarizations σ^+ and σ^- cannot be distinguished from each other in Voigt geometry, and π transitions cannot be

observed in Faraday geometry. However, breakdown of the selection rules is possible under SFRS resonance conditions. Further, observation of forbidden SFRS signals in a particular geometry may, in part, be due to the collection of scattered light over a large solid angle, which contains wavevector components from other geometries.

2.3 Angle dependence and substrate removal

Angle resolved measurements can be used to investigate the induced anisotropy in SFRS with respect to the direction of the magnetic field. The specimens were mounted on a sample holder that permitted rotation about the x-axis. Intermediate angles between the field and the growth axis were measured in two stages 0° to 50° in Faraday geometry and 40° to 90° in the Voigt configuration. Thus by means of specimen rotation, all field directions between [001] and [110] were accessible.

A change in the strain state in the epilayer could be induced by gluing the epilayer onto a glass slide using a low melting point wax, then removing the GaAs substrate by etching. The following solution was used to selectively etch away the GaAs substrate, leaving the AlGaInP epilayer glued to the glass slide: 41 ml of 1 molar sodium hydroxide (NaOH) with 9 ml of 30% hydrogen peroxide (H_2O_2). Previously, the etchant had proved to be very successful for removing the GaAs substrate from the ZnSe epilayer[8].

2.4 Dyes

In order to resonantly excite the excitonic region of the wide-bandgap semiconductors examined in this thesis emission spanning almost the entire visible spectrum was required, considerable patience and effort was necessary to achieve this spectral range using the dye lasers. Continuous wave excitation in the visible region was provided by one of two dye lasers: the Coherent C599a and the Spectra-Physics S375. These dye lasers were pumped using either a multi-line ultra-violet or a multi-line visible output of an argon-ion laser. The following dyes were used: Stilbene 1 (S1), Stilbene 3 (S3), Coumarin 102 (C102), Pyrromethene 556 (P556), Rhodamine 110 (R110), Rhodamine 6G (R6G) and DCM. The new dye P556 with its characteristic high efficiency 37 % (whilst dyes typically have efficiencies of 15 to 25 %) largely superseded R110. Lack of a suitable pump source prevented dye laser emission in the region 500 to 527 nm, where a krypton ion pump is required. Individual dye tuning ranges, intensities and recipes obtained using the Bath set-up are given in figure 2.2

and table 2.1. The tuning ranges obtained compared favourably with those quoted in the Coherent dye data sheet[9]; however, measured output powers were usually 50 % of the quoted value.

Dyes	Pump (dye laser)	Peak (nm)	Range (nm)	Recipe
Stilbene 1	All lines UV (C599a)	425	(401-437)[a]	predissolve 2g in 200ml EG + 700ml EG
Stilbene 3	All lines UV (C599a)	435	411-468[b]	predissolve 1g in 50ml BA + 1.21ml EG
Coumarin 102 (mix of C480 & C450)	All lines UV (C599a)	475	465-499	predissolve 1g C480 & 1g C450 in 300ml BA completely disolve in ultrasonic bath, 700ml EG
Pyrromethene 556	488nm (C599a)	546	(531[c]-585)[d]	2g in 1 litre EG
Rhodamine 110	All lines visible (S375)	565	545-590	predissolve 0.75g in MeOH + 950 ml EG
Rhodamine 6G	All lines visible (S375)	595	575-633	1g per litre EG, predissolved in MeOH
DCM	All lines visible (S375)	640	615-680	0.5g per litre EG, predissolved in MeOH

Table 2.1 Details of dyes. Optics according to manuals unless otherwise stated: [a] with S3 optics; [b] with C102 output coupler; [c] with C102 output coupler externally mounted; [d] R110 optics. EG(ethylene glycol); BA(benzyl alcohol); MeOH (methanol).

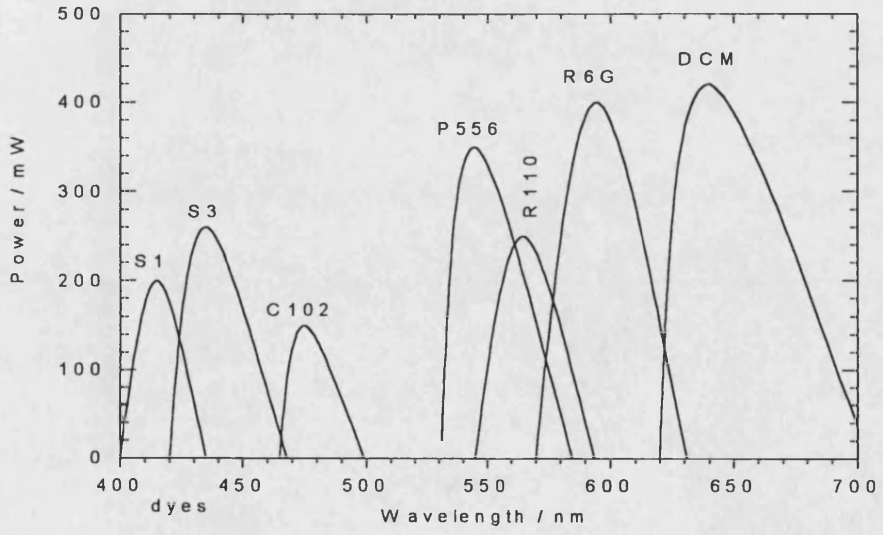

Figure 2.2 Dye ranges and output powers obtained in this investigation using Bath experimental arrangement. Output power quoted is for fresh dye at 3 W UV or 4.5 W visible.

The alignment procedures for the C599a and the S375 dye laser are adequately described in their respective manuals[10,11]. However, it is extremely useful to know the correct pump and fold mirror spot shapes. For optimal performance of the C599a dye laser it is strongly recommended that the spots are brought into focus at 2 m from the fold mirror, not 0.64 m as suggested in the manual. At this revised focal distance the spots form crowned vertical ellipses approximately 4mm high, figure 2.3. In the case of the S375 dye laser the alignment procedure suggested in the manual was adhered to. The fold and pump mirror spots were both circular.

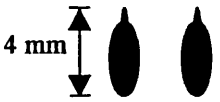

Figure 2.3 Correctly focused C599a dye laser spots 4mm high at 2 m from the fold mirror.

2.5 Fitting procedure

Figure 2.4 shows the various steps involved in the fitting procedure for the deconvolution of overlapping SFRS signals. The figure shows the Stokes portion of a SFRS spectrum from a p-type GaInP sample in a tilted magnetic field of 6 Tesla. The complex background consists of the foot of the laser line, PL and acoustic phonon scattered light. This background cannot be measured independently of the SFRS signal, see figure 2.5, since the underlying recombination pathways may change with excitation energy, magnetic field strength and polarization geometry, it was therefore necessary to subtract the fitted background for each individual spectra. The SFRS signals could then be fitted. The overall fit and the fitted peaks are presented in the low portion of figure 2.4. Whenever possible the anti-Stokes peak positions were also employed to facilitate the fitting procedure. The overall experimental uncertainty obtained from fitted field dependent measurements were, typically, 0.08 cm^{-1} for an isolated SFRS feature under favourable conditions and a maximum of 0.30 cm^{-1} if deconvolution was required. Linewidth and intensity information will be specifically examined in sections 3.1, 4.2 and 5.1 for electron, hole and excitonic features, respectively.

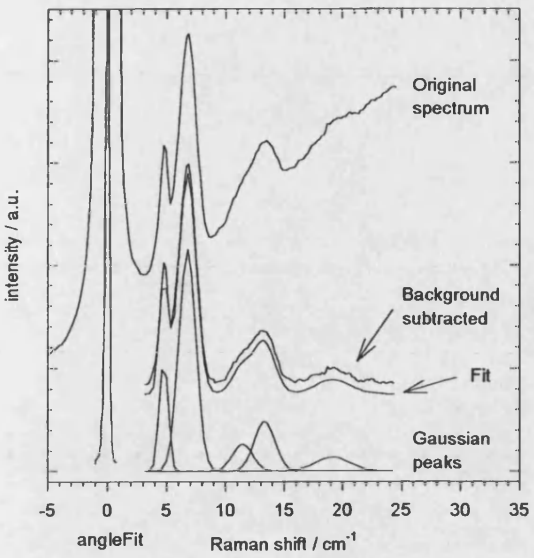

Figure 2.4 Example of fitting procedure. Stokes portion of an SFRS spectrum from a p-type GaInP sample in a tilted magnetic field of 6 Tesla.

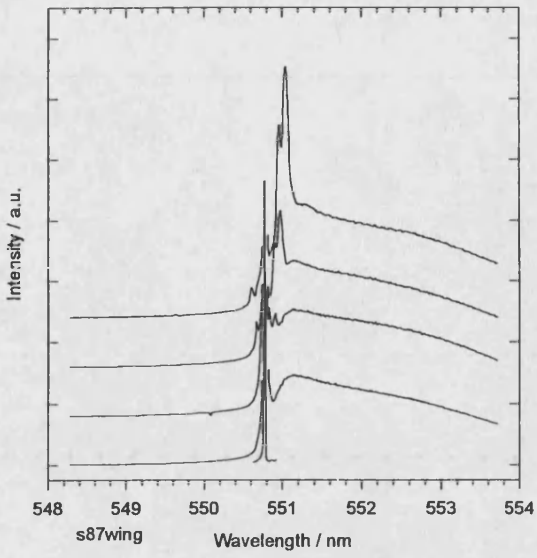

Figure 2.5 Evolution of background and SFRS for increasing magnetic field strength. The spectra are vertically displaced for presentation purposes.

2.6 References

[1] Oxford Instruments Ltd 'Superconducting Magnet Systems' (Company literature, 1988) p10

[2] Instruments S.A. Jobin-Yvon 'S3000 Technical Manual' (Company literature, 1989) p5-1

[3] Instruments S.A. Jobin-Yvon 'CCD Array Detection Systems' (Sales literature,1988) p1

[4] EMI Electronics Ltd 'Photomultiplier Tubes' (Company literature, 1970) p2

[5] RCA Tube Operations 'Photomultipliers' (Sales literature, 1984) p3

[6] S.P.S. Porto, J.A. Giodmain and T.C. Damen, Phys. Rev. 147 (1966) 608

[7] Y. Oka and M. Cardona, Phys. Rev. B **23** (1981) 4129

[8] Catherine Orange, PhD thesis, University of East Anglia, Norwich 1998

[9] Coherent Radiation Laboratories 'Coherent 599 dye laser fact sheet' (Company literature, 1999)

[10] Coherent Radiation Laboratories 'C599 Dye Laser Manual' (Company literature, 1986) p7-5

[11] Spectra-physics 'CW Dye Lasers'(Company literature 1984)

Chapter 3 - Electrons

This chapter is primarily concerned with the determination of the electron gyromagnetic ratio in binary, ternary and quaternary alloys. The aim of the first section is to introduce the features seen in the photoluminescence and spin-flip Raman scattering spectra of ZnSe. The second section is concerned with the compositional dependence of the electron gyromagnetic ratio in the quaternary II-VI alloy ZnMgSSe. The third section extends the discussion to the III-V phosphide based material and establishes the effects that changing the substrate orientation has on the luminescence and SFRS of the ternary alloy GaInP. Finally, in the fourth section, the compositional dependence of the electron gyromagnetic ratio in the quaternary alloy AlGaInP will be presented.

3.1 The excitonic region of ZnSe

This first section seeks to introduce the important PL and SFRS features commonly observed in ZnSe. To achieve this a variety of ZnSe material is examined from several institutions. The section begins with a brief review of PL.

At low temperatures PL is a sensitive probe of low-lying energy levels and used in conjunction with other techniques has provided invaluable quantitative impurity-specific information for basic research and characterisation purposes. In the context of this present work a detailed understanding of the PL is essential, since the highly resonant nature of the SFRS process dictates that the laser energy be near coincident with the excitonic transition under investigation for the SFRS signal to be observed.

The PL process consists of three phases: i) above bandgap excitation leads to exciton formation; ii) rapid energy relaxation of the exciton occurs via phonon-assisted thermalisation; and iii) radiative recombination of the exciton by the emission of a photon. In high purity material at low temperatures recombination occurs at the conduction and valence -band extrema and the energy of the emitted photon is $\hbar\omega = E_0 - E_b$, where E_b is the exciton binding energy. This process is known as free-exciton (FE) luminescence. The presence of impurities may lead to the existence of shallow energy levels within the forbidden gap. In material containing shallow donors and acceptors with concentrations greater than 10^{15} cm^{-3} virtually all of the FE are captured by very efficient neutral donors and acceptors traps, forming neutral bound exciton complexes, respectively denoted D^0X and A^0X (or alternatively I_2 and

I_1). Subsequent recombination from these centres results in the emission of a photon with energy $\hbar\omega = E_0 - E_I - E_b$, where E_I is the donor or acceptor ionisation energy. In compensated material mutual ionisation between donor and acceptor centres can trap optically excited electrons and holes to produce neutral centres, whose captured electron and hole may then radiatively recombine, leaving the ionised centres, such that: $D^0 + A^0 \rightarrow \hbar\omega + D^+ + A^+$. This process is known as donor-acceptor pair (DAP) luminescence. Figure 3.1.1 shows excitonic and DAP luminescence from ZnSe material produced in several institutions, the growth details of which are given in Appendix B.

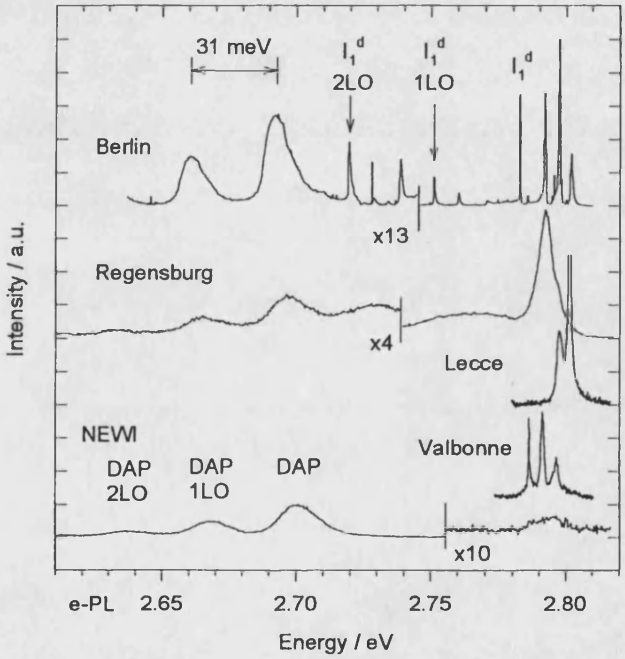

Figure 3.1.1 Low temperature excitonic and DAP luminescence from ZnSe material produced at several institutions using a variety of different growth techniques, see appendix B for sample details. With the exception of the Lecce material all spectra were obtained using above bandgap excitation (~ 2.85 eV).

The peaks at approximately 2.69 eV are assigned to zero phonon DAP recombination[1-4]. The precise position of the DAP peak varies with excitation intensity, doping concentration and dopant species. The recombination energy, $\hbar\omega$, between the donor ground state E_D and the acceptor ground state E_A is given by

$$\hbar\omega = E_g - E_D - E_A + \frac{e^2}{4\pi\varepsilon_0\varepsilon_r R_{DA}} - m\hbar\omega_{LO} \qquad (3.1)$$

Accurate determination of binding energies is difficult using equation (3.1) without knowledge of the fourth, coulomb, term. However, a rough estimate of, for example, the lithium acceptor binding energy may be obtained taking the measured position of

the Berlin DAP^{Li} luminescence (2.6923 eV) together with reasonable values of E_D (26.1 meV) table 3.1, the coulomb term (10-15 meV)[5] and the bandgap, E_0, (2.8218 eV)[6]. A value of 115.5 ± 2.5 meV is obtained using equation (3.1) in fair agreement with the binding energy for Li of 114 meV[6-8]. Similarly, the N binding energy may be estimated from the Regensburg and NEWI samples, giving 111 meV and 108 meV, respectively, see table 3.1.

	FE	Ga	Cl	Al	N	Li	P	I_1^d
$\hbar\omega$ (eV)	2.8023	2.7975	2.7977	2.7977	2.792	2.7921	2.7913	2.7831
E_I (meV)		27.2	26.1	25.6	111-114	114±0.4	80-90	

Table 3.1 transition energy($\hbar\omega$) and ionisation energy(E_I) in strain-free ZnSe[6,8].

On the lower energy side of the zero phonon DAP emission is a series of LO phonon replicas, as described by the fifth term in equation (3.1), separated by the characteristic LO phonon energy of 31 meV for ZnSe at low temperatures[9]. Another phonon replica series belonging to the deep acceptor (I_1^d)[6] is also indicated in figure 3.1.1. However, SFRS is not observed in resonance with the DAP, therefore emphasis will now be placed on the excitonic region, where SFRS signals are observed.

To facilitate the discussion of the PL spectra the excitonic region has been expanded in figure 3.1.2 with the corresponding spin-flip spectra presented alongside in figure 3.1.3. The PL spectra presented in figure 3.1.2 will now be discussed in turn.

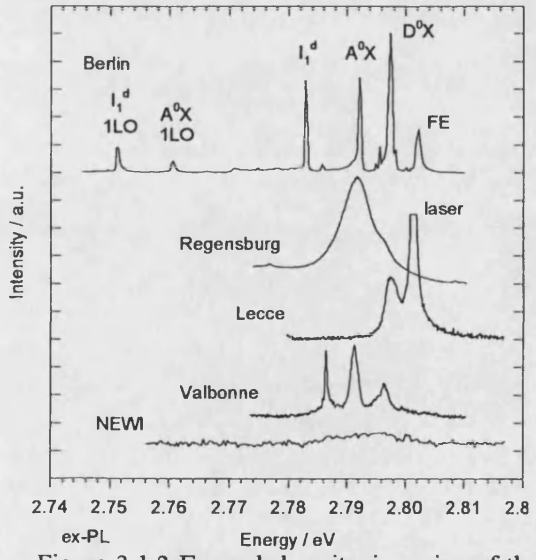

Figure 3.1.2 Expanded excitonic region of the ZnSe material presented in figure 3.1.1

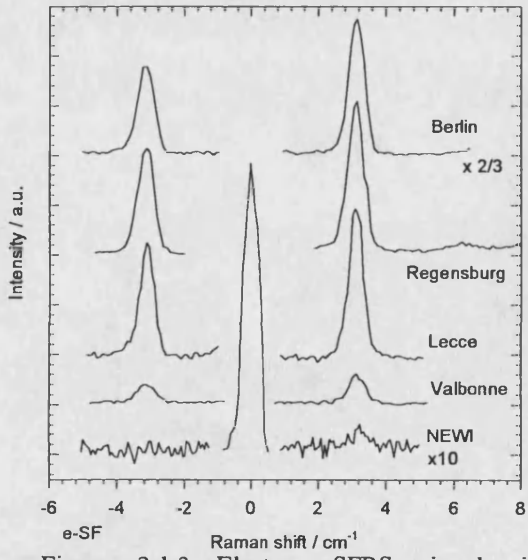

Figure 3.1.3 Electron SFRS signals in resonance with D^0X, corresponding to the PL figure 3.1.2. See section 1.3.2 for a description of spectra.

The uppermost spectrum in figure 3.1.2 shows the excitonic PL from a strain-free bulk ZnSe single crystal. The crystal contains lithium as an unintentional dopant and was grown in Berlin using the Markov vapour phase transport method[10]. The specimen is of very high crystalline quality, as indicated by the extremely narrow excitonic luminescence linewidths (less than 0.8 meV), and therefore provides an excellent example with which to compare other ZnSe material. The most prominent feature in the spectrum, I_1^d at 2.783 eV, has been associated with the presence of Cu[11]; however, more recent studies performed on samples grown under Se-rich conditions indicate that it is related to zinc vacancies V_{Zn}[8,12,13]. No SFRS was detected in resonance with I_1^d and none has been reported in the literature. The excitionic region also shows well-resolved FE, D^0X and A^0X recombination at 2.8022 eV, 2.7975 eV and 2.7923 eV, respectively. These emission energies agree closely with previous work[6,8], enabling Li to be confirmed as the p-type dopant. Of all the samples studied in this investigation, this sample exhibits the strongest SFRS in resonance with the shallow donor, see figure 3.1.3. The A^0X and the hole SFRS associated with it will be discussed fully in the next chapter.

The Regensburg sample was grown by MOVPE and formed part of a trial growth series in which nitrogen doping, using the precursor phenylhydrazine, was investigated. The origin of the broad luminescence lines in this sample is not immediately clear. Based solely on the PL and the sample thickness (0.6 μm) the dominant line at 2.7916 eV might be assigned to A^0X; however, SFRS shows this assignment to be incorrect. In Figure 3.1.4 the integrated intensity of the SFRS signal is shown as a function of excitation energy. Contrary to the selection rules for holes in Voigt geometry the SFRS resonance profile is dominated by the signal at 2.7916 eV, indicating that the signal is not related to A^0X. The gyromagnetic ratio of ~1.12, measured in resonance with the emission lines at 2.7916 eV and 2.7961 eV, is that of the shallow donor in ZnSe[14,15]. This eliminates the possibility that either line originates from the deep donor centre, which has a characteristic g-value of 1.39[16]. Thus, the signals are shallow donor related. However, the separation of the lines, ~4 meV, is too great to be accounted for by various combinations of the principal shallow donor impurities, Al, Cl, Ga, In and F (which differ by less than 1 meV). Therefore, further explanation must be sought.

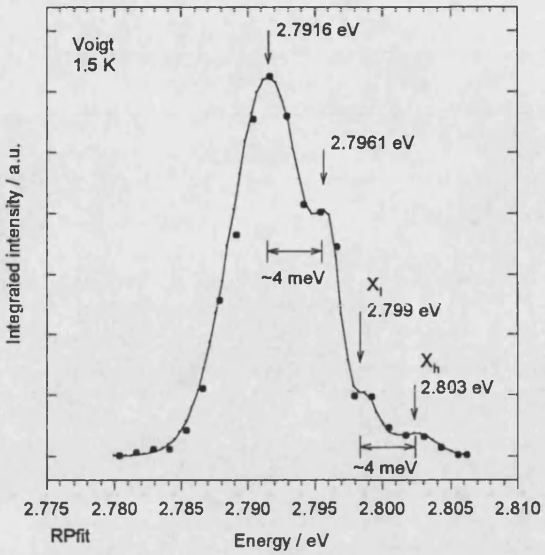

Figure 3.1.4 Variation of the SFRS signal integrated intensity as a function of excitation energy, also known as a resonance profile, obtained from the Regensburg ZnSe material. Each data point has a corresponding g-value of ~1.12, indicating that all features are either FE or D^0X related.

The shallow donor lines in this region have, in the past, been attributed to: i) strain-splitting of the D^0X ground state[17-19], ii) the D^0X ground state together with an excited electronic state[20] and, more recently, iii) N related shallow donor complexes have also been proposed[21,22]. The latter can be rejected immediately since no acceptor PL or SFRS was detected in this sample, indicating a low N content, and as the N shallow donor is thought to be formed as an integral part of the acceptor compensation process[23] it, therefore, seems unlikely that N shallow donor emission would dominate the PL spectrum. The thickness of the sample indicates that the epilayer should experience a small, less than -0.1%, compressive strain[24]. However, the SFRS resonance profile, figure 3.1.4, clearly shows that the FE has split into light-hole, X_l, and heavy-hole, X_h, components and that the epilayer is experiencing a thermally induced tensile strain[24]. The splitting of the FE together with the broadness of the emission bands, caused by inhomogeneous broadening due to a large distribution in the strain states within the layer, indicate that the epilayer has completely relaxed[25] and thus only the thermally induced strain component remains. The partial lifting of the degenerate valance-band states due to biaxial tensile strain, appropriate for the Regensburg specimen, is illustrated in figure 3.1.5 (a full explanation of this process is given in section 1.2.4).

Examination of the resonance profile reveals that the FE and D^0X line have split by similar amounts, approximately 4 meV. This energy is consistent with an +0.2% in-plane tensile strain, usually observed in relatively thick layers greater than 2 μm.

However, even within thin layers the strain may relax by the nucleation of misfit dislocations[26,27], due to incorrect growth conditions. Thus, the broadened linewidths, the splitting of the D^0X and FE lines and their energetic positions can all be accounted for within the framework of strain relaxation, without recourse to arguments involving excited states.

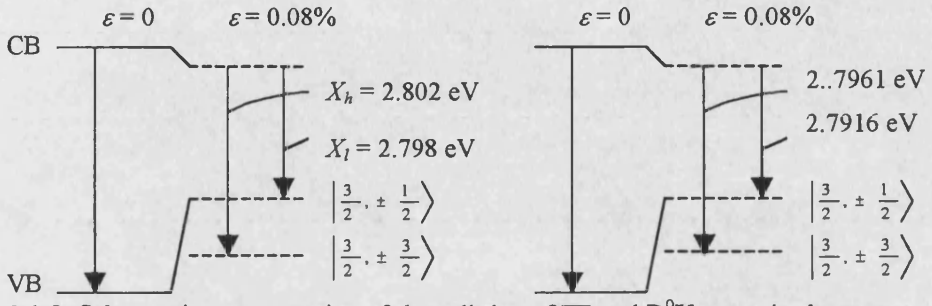

Figure 3.1.5 Schemeatic representation of the splitting of FE and D^0X states in the presence of a tensile biaxial strain for the Regensburg ZnSe epilayer, as discussed 1.2.4.

For the Lecce sample the excitonic and DAP luminescence from this sample were extremely weak and D^0X emission could only be excited by selective excitation, with the laser energy in resonance with excited states of D^0X in the vicinity of the FE, see figure 3.1.2. In spite of this, strong electron SFRS was observed in resonance with D^0X and FE at 2.7968 eV and 2.801 eV, respectively. No hole SFRS was observed in the vicinity of A^0X in Faraday geometry.

The Valbonne sample was grown by MBE and was doped with a pure P-vapour plasma under Se-rich conditions. The narrow line at 2.786 eV corresponds to the 2LO phonon from the laser. The origin of the peak at 2.7913 eV is attributed by the grower[28] to a P-related A^0X. The grower also reports D^0X at 2.797 eV, FE at 2.801 eV[29] and DAP emission at 2.730 eV[28]. The weaker line at 2.7964 eV in the immediate vicinity of D^0X has been a source of controversy in the literature, being attributed to both A^0X^{P30}, due to its LO phonon coupling strength, and D^0X^{Ga}, presumed to originate from Ga in-diffusion from the substrate[31]. The SFRS signal in resonance with this line, figure 3.1.3, identifies it as shallow donor related. The origin of this line will be clarified in section 4.1.

The NEWI sample exhibits a deep red emission, around 2.01 eV, and broad weak excitonic emission, indicating poor crystalline quality. This is confirmed by the X-ray rocking curve data (FWHM 260-350 arc s). SFRS from shallow donors is extremely weak and although the DAP emission suggests the presence of holes in the sample the concentration of shallow acceptors is below the threshold necessary for detection by

SFRS. The evidence is consistent with a stoichiometric deficiency leading to the formation of deep centres.

It is apparent from figure 3.1.3 that despite the change in dopant species, doping concentration and crystal quality that the FWHM of the shallow donor SFRS is not significantly altered. For the samples in this section the SFRS FWHM equaled 0.66 ± 0.07 cm^{-1}. It is also clear from figure 3.1.3 that it is not possible to infer any systematic trend concerning the crystalline quality of the samples from the variation in the intensity of the SFRS signals, due to the highly resonant nature of the SFRS process, other than the fact that very poor quality material exhibits weak SFRS.

Lastly in this section the magnetic field dependence of the shallow donor electron SFRS signal will be examined. It has already been established in section 1.3.2 that the Raman shift of the electron SFRS signal is linearly dependent on the magnetic field strength, in accordance with equation 1.38. Presented in figure 3.1.6 are the Stokes SFRS signals from shallow donors at various magnetic field strengths, with the corresponding integrated intensity and FWHM data from the fitted spectra shown in the main part of figure 3.1.7 and the inset, respectively. It is clear that both the

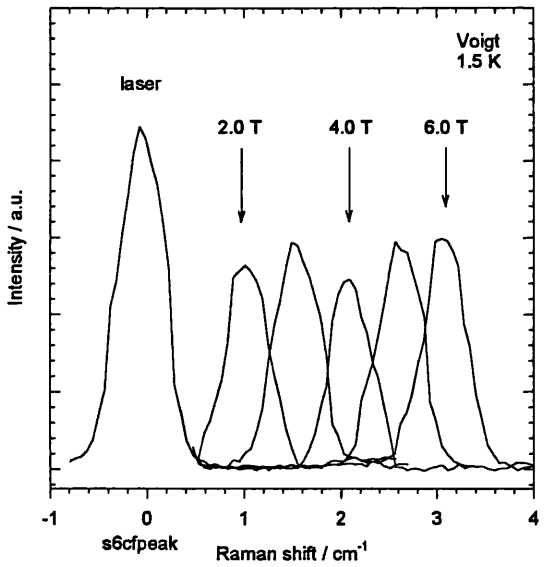

Figure 3.1.6 Stokes electronic SFRS signals in resonance with D^0X in ZnSe for various magnetic field strengths. The left most feature is the laser line.

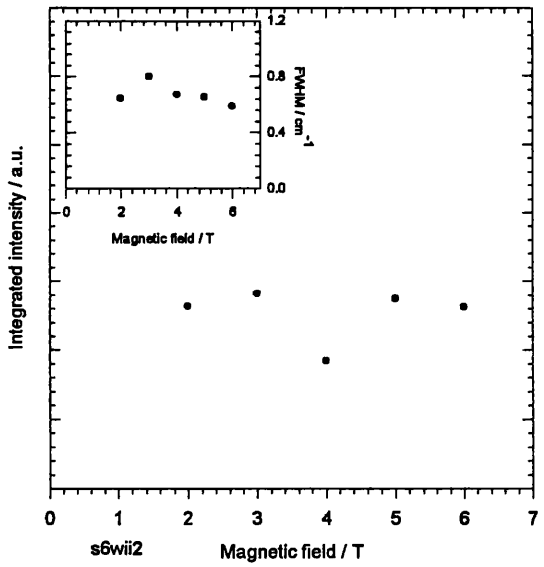

Figure 3.1.7 The integrated intensity and FWHM (inset), for signals presented in figure 3.1.6, as a function of magnetic field strength.

FWHM and the integrated intensity manifest only a weak dependence on the magnetic field strength and that both remain finite when the field is removed. However, caution must be exercised in interpreting the SFRS integrated intensity in binary alloys, since the excitonic transitions are well defined and, therefore, the SFRS signals

will be highly sensitive to the excitation energy. The data presented above was obtained with the intention of providing precise determination of the Raman shift dependence on magnetic field, not the integrated intensity. This point is less crucial for the ternary and quaternary material, examined later, in which the excitonic transition energy is less well defined. The FWHM data is not strongly affected by the precise resonance conditions.

The fundamental PL emission process has been briefly reviewed and the PL features relevant to this work have been introduced. A survey of ZnSe material produced using a variety of growth techniques and a with range of crystal qualities, doping concentrations and dopant species has been conducted using PL and SFRS. Despite variation in the impurity species and crystal quality, electron SFRS was invariably detected and found to have a g-value of 1.12 ± 0.03, which is the value measured for the FE in ZnSe. The ubiquity of the electron SFRS signal in ZnSe is due to its detection in high purity material via free-exciton resonance or from intentional and unintentional shallow donor impurities. The insensitivity of the g-value to the chemical species of shallow donor and the local environment is attributed to the extended nature of the electron wavefunction.

The following key features of the SFRS process have become apparent: i) magnetic field dependent measurements enable the gyromagnetic ratio of centres to be accurately determined; ii) the strong excitation energy dependence enables precise determination of the transition energy of the centre under investigation; and iii) resonant enhancement of the scattering process enables SFRS signals to be observed, even though the PL may be extremely weak. These unique abilities enable SFRS to identify specific types of impurities, ensure that in the presence of additional perturbations, such as strain, spectra are correctly interpreted and augment other spectroscopic techniques.

Finally, examination of the magnetic field dependence of the shallow donor SFRS reveals that the FWHM is independent of the field strength and that the integrated signal intensity is only weakly field dependent. These findings will prove crucial for the interpretation of the less well known ternary and quaternary SFRS examined later. Thus, having established the ability of SFRS in the study of excitonic features in binary ZnSe the method will now be employed to investigate ZnSe-based alloys.

3.2 The dependence of the electron gyromagnetic ratio in ZnMgSSe

The ZnMgSSe system was introduced approximately a decade ago[32]. However, in spite of its technological importance comprehensive studies of its electronic and optical properties over a wide range of compositions have yet to be conducted. For devices in which ZnSe or ZnSSe is used as the cladding layer the lasing wavelength cannot be shorter than in the blue-green spectral region[33], shorter wavelength devices require a wider bandgap material for the cladding layer. The suitability of ZnMgSSe as a cladding layer material for blue and blue-green laser diodes has been demonstrated[34-36], with ZnCdSe, ZnSe or ZnSSe forming the active region. Both n-type and p-type doping has been achieved[37,38]; however, as is the case for ZnSe, p-type doping of the ternary and quaternary alloys has also proven to be problematic. The issues of p-type doping will be discussed further in section 4.4 of the next chapter.

The structural properties of ZnMgSSe have not been extensively examined. There are no reports of long-range order for the ZnMgSSe system, despite the theoretical prediction[39] of large ordering effects in virtually all III-V and II-VI alloys. A weak dependence of the PL emission energy as a function of substrate orientation has been reported for ZnMgSSe[40] and for ZnSSe[41]; data for the latter is displayed alongside GaInP data in figure 3.3.3. Significant amounts of short-range ordering, in the form of MgS and ZnSe clusters, is predicted for technologically important compositions of ZnMgSSe. In epitaxial material clustering is in part driven by bond length considerations, with bond lengths closest to the substrate being energetically favoured, see figure 1.3. Compositional modulation corresponding to regions with different Mg and S concentrations has been observed[42] by transmission electron microscopy (TEM). However, an EXAFS study[43] of MBE grown $Zn_{1-x}Mg_xS_ySe_{1-y}$ (x=0.18, y=0.2) found a random distribution of the chalcogen atoms, implying negligible clustering in ZnMgSSe.

The series of $Zn_{1-x}Mg_xS_ySe_{1-y}$ samples under investigation in this section lie in the composition range $0<x<0.14$ and $0<y<0.27$ and consist of the nominally undoped quaternary barriers of single quantum well (SQW) structures and N-doped ternary and quaternary epilayers. In $Zn_{1-x}Mg_xS_ySe_{1-y}$ epilayers, x is kept well below 0.4 to avoid any phase change in the material into wurtzite or rocksalt structures. The samples were grown by MBE, with one exception which was grown by MOVPE. All material was grown on (100) GaAs substrates. The free hole concentration of the N-doped

samples was determined by electrochemical C-V profiling[44]. The compositions were determined from the relaxed lattice constant and by interpolation from the bandgap energies. The epilayers were sufficiently thick, greater than 1 μm, to assume that the layers were relaxed: X-ray measurements showed that the mismatch was less than 0.1 % and SFRS measurements at 1.5 K, sections 4.4 and 5.1, demonstrate that the strain was indeed negligible. The sample details are given in appendix B.

The dominate feature in the low temperature PL spectra, figure 3.2.1, has been attributed to impurity-bound exciton recombination by analogy with ZnSe and from its temperature dependence[45]. Observation of electron SFRS in resonance with this feature also supports this assignment. The FWHM of the excitonic PL, 12.4 ± 2.67 meV, is significantly broader than the bound excitonic emission from ZnSe, which is typically less than 2 meV for good quality material. The inhomogeneous broadening of the ZnMgSSe has been attributed to the isoelectronic substitution[46] and alloy clustering[47]. Crucially, however, despite the broadening of the PL band, the SFRS

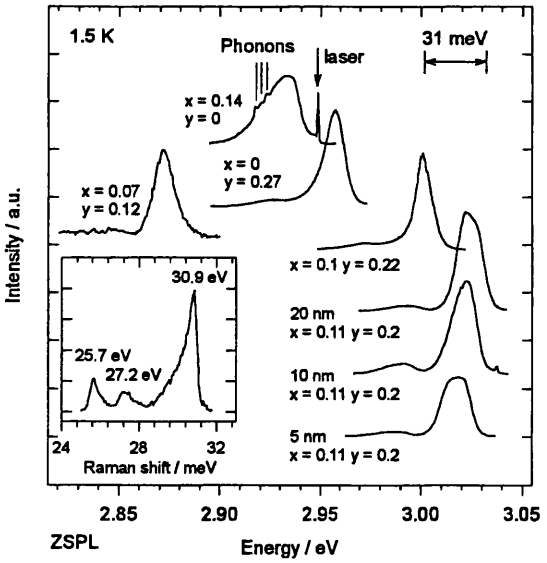

Figure 3.2.1 Low temperature luminescence from ZnMgSSe epitaxial material. The upper four spectra are from nitrogen doped specimens, the lower three spectra are barrier emission from SQW structures. Resonant phonon features in with ZnMgSe excitonic emission band, uppermost spectra. Inset ZnMgSe phonon Raman spectrum.

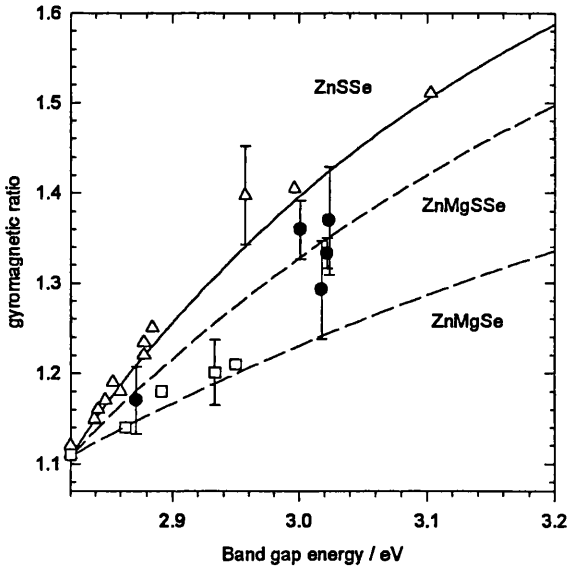

Figure 3.2.2 Dependence of electron gyromagnetic ratio on the bandgap energy for ZnSe-based alloys. Curves show the results of five-band third-order $k \cdot p$ calculations: solid line ZnSSe[52], dashed line ZnMgSe[52] and dotted line ZnMgSSe; with triangles, squares and filled circles indicating respective data sets.

linewidth in ternary and quaternary alloys remains comparable to those in the binary material, see section 4.4 for the SFRS spectra. The DAP emission (not shown), identified by its temperature dependence[48], is also much broader in ZnMgSSe than in ZnSe and is typically situated 100-110 meV below the bound excitonic emission

band. A full discussion of the DAP emission from the N-doped samples is given in reference[44].

The uppermost PL spectrum in figure 3.2.1 shows three distinct phonon features obtained by resonant Raman excitation. In ternary compounds, such as ZnMgSe, the zone centre optical phonons are expected to exhibit "two-mode" behaviour[48]. The inset, figure 3.2.1, shows an in-going resonant phonon Raman spectrum. "ZnSe-like" LO and TO modes are clearly evident at 30.9 meV and 25.7 meV, respectively. However, the peak at 27.2 meV does not correspond to LO or TO GaAs modes and is therefore presumed to be associated with Mg, although a complete study of the composition dependence of zone-centre optical phonons in ZnMgSe has yet to be published in the literature. Nevertheless, the phonon Raman spectrum is completely dominated by the "ZnSe-like" LO phonon mode, as a result the phonon energies are not expected to change significantly with composition[49], for the values of x and y used in this study. The relatively weak feature which appears at ~31 meV to lower energy of the bound exciton is, therefore, tentatively attributed to the phonon replica of the bound exciton.

The direct bandgap as a function of composition has been determined for $Zn_{1-x}Mg_xS_ySe_{1-y}$ at room temperature[50]

$$\begin{aligned} E_g(x,y) = {} & (1-y)\,E_g(ZnSe) + x\,(1-y)\,[E_g(MgSe) - E_g(ZnSe)] \\ & + x\,y\,[E_g(MgS - E_g(ZnS)] + y\,E_g(ZnS) \\ & + A\,x\,(1-x) + B\,y\,(1-y) + C\,x\,y\,(1-x) + D\,x\,y\,(1-y) \end{aligned} \qquad (3.2)$$

where A = -0.53, B = -0.42, C = 0.20 and D = -B are the bowing parameters in eV. The temperature dependence of the bandgap in ZnSSe and ZnMgSSe was found to be identical to that of ZnSe[48]. It is therefore reasonable to adopt the low temperature binary bandgaps, whilst assuming the bowing parameters are constant, in order to estimate the low temperature dependence of the bandgap on composition from the above expression. The bandgaps used were ZnSe = 2.82, ZnS = 3.78, MgSe = 4.05 and MgS = 4.5 eV.

Although the three SQW samples have the same nominal composition, there exists a fair degree of variation in their individual lineshapes and in the energetic positions of their emission bands in the PL. This variation translates into a fairly large variation, ~5 %, in the g-values of the samples; demonstrating both the sensitivity of the SFRS to composition in ZnSe and the inherent difficulty in precisely controlling the growth

process of quaternary alloys. The presence of the SQW is not expected to influence the g-value in the barrier[51].

Figure 3.2.2 shows the dependence of the electron gyromagnetic ratio on bandgap. The fitted curves to the experimental data have been calculated using $\boldsymbol{k}\cdot\boldsymbol{p}$ perturbation theory in conjunction with suitable interpolation schemes. It has been established by successive degrees of approximation[52] that the third-order, five-band $\boldsymbol{k}\cdot\boldsymbol{p}$ perturbation theory gives the most satisfactory approximation to the observed compositional dependence of the gyromagnetic ratio of the electron for ZnSSe and ZnMgSe alloys. Most of the parameters required to implement the third-order approximation for ZnSSe are unknown. Therefore, a linear interpolation between the ZnSe and ZnS end members is used together with the compositional dependence of the bandgap, equation (3.2), for ZnSSe. This procedure gives good agreement over the entire ZnSSe range for the gyromagnetic ratio dependence on bandgap. The inability to grow MgSe in the zincblende structure[53], prohibits the use of the interpolation scheme outlined above for ZnSSe, since very little data exists for MgSe. From equation (3.2) the variation of bandgap ZnMgSe with composition is known, after this the most significant parameter in equation (1.13) is, Δ_0, the spin-orbit splitting. As previously noted, however, the properties of the valence-band are largely determined by the anion and a systematic trend exists for the spin-orbit splitting. For ZnS, ZnSe and ZnTe Δ_0 are 0.10, 0.42 and 0.9 eV, respectively, and for CdS, CdSe and CdTe they are 0.07, 0.43 and 0.81 eV. Therefore, Δ_0 equal to 0.43 eV is inferred for MgSe and the value of E_p of 20 eV is taken, this being typical for zincblende semiconductors[54]. All other values are taken from ZnSe and held constant throughout the interpolation. Though crude, this scheme produces reasonable agreement with experiment.

The proceeding discussion suggests that a suitable interpolation scheme for quaternary data may be obtained by calculating all the parameters according to the S content of the ternary ZnSSe, as above, whilst using the correct value for the quaternary bandgap composition, obtained from equation (3.2). However, unlike the ternaries, there is no unique correspondence between the bandgap and the composition for the quaternary material. For this reason it is difficult to present the quaternary data on the same graph as the ternary material. This problem is overcome by defining the Mg content to be equal to half the S content: this procedure is valid since it ensures that the compositions are correct for ZnSe and technologically

significant barrier compositions. The prediction based on the above interpolation scheme reproduces correctly the observed trend for the quaternary material, though, the agreement with experiment is not as good as in the case of the ternary systems.

The quaternary alloy ZnMgSSe has been investigated using PL, resonant vibrational Raman scattering and SFRS. The dominant spectral feature observed in the PL has been attributed to impurity-bound excitonic recombination. Vibrational mode spectra can yield important microstructural information. Observation of the binary modes indicate that the bond length of the binary end member is retained in the alloy, implying deviation from Vegard's law[55] on a microscopic scale. Examination of resonant phonon Raman spectra indicates that the weaker feature, found to lower energy of the dominant excitonic peak, may be attributed to a phonon replica. The observed excitonic linewidth is much broader than expected from the customary thermal broadening and results from inhomogeneous broadening introduced by the isoelectronic impurities in going from binary to ternary material. The random distribution of atoms on their respective sublattices in the alloy system introduce new physics not found in elemental group IV or binary semiconductors, which strongly influences the optical properties of the semiconductor.

The dependence of the gyromagnetic ratio as a function of bandgap energy has been determined. The third-order five-band $\boldsymbol{k \cdot p}$ theory expression, given in section 1.2.1, was found to give a reasonable description of the observed quaternary alloy dependence, in the composition range crucial for the fabrication of light emitting devices. Many important bandstructure parameters as yet undetermined for this alloy, were estimated for the $\boldsymbol{k \cdot p}$ calculation using simple arguments based on other II-VI materials. Thus, in this section it has been demonstrated that SFRS can be successfully applied to wide-bandgap II-VI alloys. The debate will now be extended to the III-V ternary alloy GaInP.

3.3. The effect of substrate orientation on $Ga_{0.52}In_{0.48}P$

Studies of GaInP[56-59] have indicated that long-range ordering is considerably affected by the orientation of the underlying substrate. In this section the influence of substrate orientation on the PL and SFRS is investigated for GaInP and evidence concerning AlGaInP is briefly examined. The section begins with a discussion of ordering in GaInP.

As discussed in section 1.1.1, GaInP exhibits spontaneous long-range ordering on the cation sublattice. This long-range ordering is most commonly manifested as CuPt-type ordering, in which alternating GaP-InP monolayer form superlattices along two, of the four possible, ⟨111⟩ directions on (001) substrates. The most direct manifestation of CuPt-type ordering is the observation of new superlattice diffraction spots in X-ray spectra[60]. Partially ordered GaInP exhibits a mosaic-like structure, in which ordered and disordered phases coexist. This partially ordered material can be characterized by the order parameter η and the domain size. The order parameter η denotes the fraction of Al or Ga in the alternating ordered planes: $(Ga_{x+\eta/2}In_{1-x-\eta/2}P)/(Ga_{x-\eta/2}In_{1-x+\eta/2}P)$, where $\eta = 1$ indicates perfect order and $\eta = 0$ indicates complete disorder. The domain size indicates the extent of the ordered region, the dimensions of which are defined by antiphase boundaries (APB). An APB is the transitional region, typically a few monolayers wide, in which the sequence of Ga-rich and In-rich ordered planes is reversed. The lateral extent of the domains have been reported to range from several tens of a nanometre[61,62] to the order of a micron[63]. Micro-PL studies[61,64], via the observation of localized excitonic transition, indicate that the potential relief in partially ordered GaInP results in the formation of intrinsic quantum dots. Detection of the localised excitonic signal was correlated with the APB, implying that the APB is responsible for the localisation. The APB have been shown to form disc-like islands in partially ordered material by TEM[64]. A number of distinct effects associated with partial ordering have been observed using a variety of spectroscopic techniques, including PL[65-67], PLE[68] and reflectivity[69], these are: i) the reduction of the bandgap; ii) the splitting of the valence-band; iii) a Stokes shift of the PL relative to the PLE; iv) an intensity dependent PL structure; and v) broadening of the exciton lines. The reduction in bandgap due to ordering has been used extensively in the literature to determine the degree of ordering[70]. However, whilst ordering certainly reduces the bandgap, so does local phase separation (clustering) and tensile strain[39]. A phenomenological explanation of these effects in terms of a distribution of domains with varying degrees of ordering has been proposed[39]. Whilst, the effect of long-range ordering has been explained[71] in terms of zone folding, in which the electronic states at the L point are zone folded to the Γ point, repelling the Γ_6^c states to lower energy. The additional periodicity along the ordering direction also leads to a reduction of the point group symmetry from T_d (zincblende) to C_{3v} (rhombohedral)

and produces a crystal field splitting of the valence-band, reducing the symmetry of the valence-band states from Γ_8 to Γ_4, and $\Gamma_{5,6}$ in the ordered material[68]. Therefore, the total bandgap reduction is a combination of downward repulsion of the conduction-band due to zone folding and upward repulsion of the valence-band due to the crystal field splitting. Bandgap reductions as large as 100 meV have been measured in the most highly ordered material, with the crystal field splitting contributing as much as 30 meV towards this value[72].

The degree of ordering and the domain size of the ordered region in GaInP has been found to be strongly dependent on the growth conditions and surface orientation[39]. The degree of ordering is affected by growth method and the prevailing growth conditions, such as, growth temperature[73], growth rate[74], III/V ratio[75], surface misorientation[56-59] and the presence of dopants during growth (see section 4.5). It has also been shown that spontaneous ordering in GaInP occurs due to surface rather than bulk thermodynamic effects during growth[39]. The use of misorientated substrates in both II-VI and III-V materials has been shown to improve the incorporation of p-type dopants[40,72,76], to reduce the surface defect density[77] and to increase the optical gain of epitaxial structures[78].

Despite the importance of the quaternary alloy AlGaInP to optoelectronic devices, the issue of ordering has not been extensively studied. Although superlattice diffraction spots have been observed in AlGaInP[79], the results of optical investigations are less conclusive than in the case of GaInP[80]. Increasing the Al content is not expected to affect the degree of ordering, because AlP and GaP have similar lattice constants, see figure 1.3. Studies[79] indicate, however, that there is a tendency to order in AlGaInP, though this is less than in AlInP. The latter was found to have a significant degree of ordering even on substrates orientations of 10° off axis; though at 15° all CuPt-type ordering was eliminated throughout the entire composition range[79].

To investigate the effects of substrate orientation a series of latticed matched $Ga_{0.52}In_{0.48}P$ epilayers were grown simultaneously by gas source MBE at Sharp Laboratories of Europe Ltd. This was achieved by quartering a GaAs wafer and polishing each quarter to either 0°, 7°, 10° or 15° towards the (111)B plane. The wafer was then reassembled and placed in the growth chamber for growth to commence, thus ensuring that the growth conditions were identical for each substrate orientation. The phosphide epilayers were typically 2 μm thick and were deposited on a 1 μm

GaAs buffer layer; the growth was terminated by a 100 Å GaAs capping layer. Details of the growth procedure[81] and the determination of the degree of ordering[82] are given elsewhere. SFRS measurements in sections 5.2 demonstrate that the strain in these samples were negligible at 1.5 K.

Figure 3.3.1 shows the low temperature PL using above bandgap excitation. The dominant feature in the PL spectra has been attributed to the recombination of excitons weakly bound at potential fluctuations[83]. The PL lineshapes are near Gaussian in form, possessing only a slight asymmetry. The position of the absorption peak in the PLE[81] is indicated in the figure for each sample by an arrow. The inset

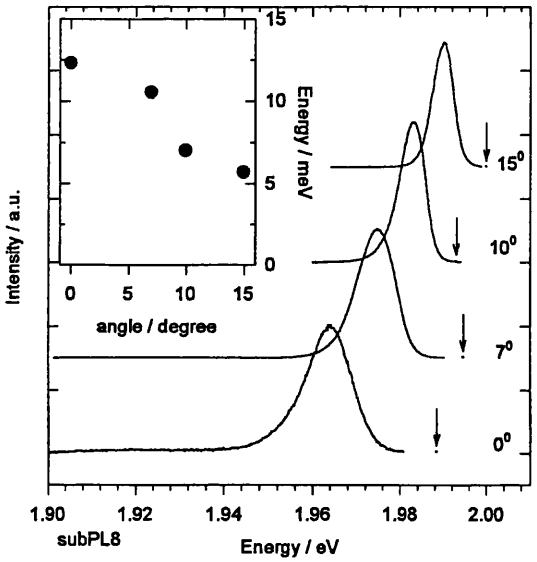

Figure 3.3.1 Near-Gaussian shaped PL from undoped MBE-grown $Ga_{0.52}In_{0.48}P$ on GaAs substrates misoriented by 0°, 7°, 10° and 15° towards (111)B plane, arrows indicate position of absorption peak maximum. Inset shows PL FWHM.

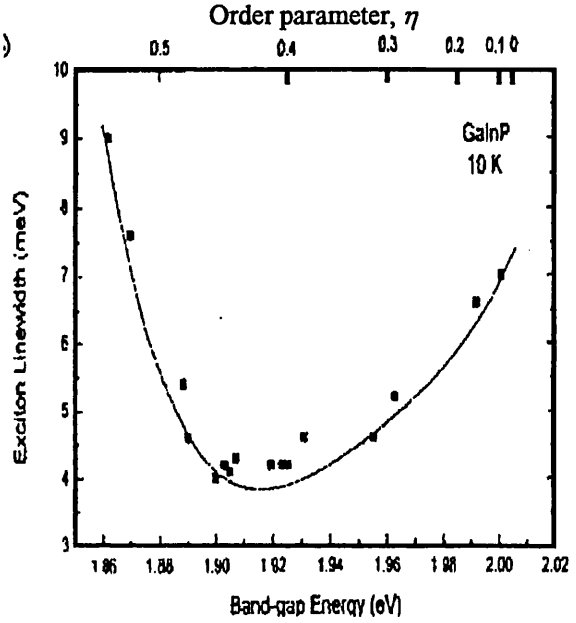

Figure 3.3.2 MOVPE AlGaInP PL linewidth as a function of the bandgap energy or order parameter η. The curve is a guide to the eye. Figure taken from reference [63].

shows the PL FWHM (filled circles) as a function of substrate orientation. It should be noted that precise determination of the absorption peak position from the PLE becomes progressively more difficult as the substrate angle is reduced[39].

Figure 3.3.2, taken from reference [63], shows the GaInP PL linewidth as a function of order parameter, η, and the bandgap energy. The correlation between the order parameter and the bandgap energy has been empirically established[70]. The specimens selected for the study possessed domain sizes of the order of 1 μm, and, therefore, represent material with the largest domain sizes obtainable with current growth techniques[63]. The linewidths thus obtained are believed to be close to the intrinsic

linewidth for the particular value of order parameter. It is clear from figure 3.3.2 that in the range $0<\eta<0.45$ the FWHM decreases with increasing order parameter. This decrease is directly attributed to the reduction in alloy fluctuations due to the spontaneous ordering of the cations[63].

In contrast, for the GaInP material investigated in this work, altering the substrate orientation from 15° (nearly disordered) to 0° (partially ordered) towards the ⟨111⟩ direction produces a significant increase in the FWHM, inset figure 3.3.1. This increase may be attributed to domain size considerations. High substrate angles limit the domain size, strongly suppressing domain formation[84]. However, low substrate angles allow domains with a range of sizes and order parameters to be formed[39]. Thus, in the case of high substrate angle the FWHM is determined by inhomogeneous broadening due to the random alloy fluctuations and, therefore, is close to the theoretical limit for a layer in which the constituents are randomly distributed[85]. Whilst, for low substrate angle inhomogeneous broadening due to variation in the degree of ordering between domains determines the FWHM. Thus, these two inhomogeneous broadening mechanisms account for the observed symmetric PL lineshape.

The PL peak position of the MBE grown specimen on a 15^0 substrate was 1.990 eV, indicating that the sample is nearly completely disordered[70], that is $\eta \sim 0$. The FWHM of this sample was 5.7 meV, which is less than the 6 meV reported for the narrowest FWHM of the nearly disordered MOVPE material[86], obtained under similar experimental conditions. The PL peak position of the MOVPE sample was also 1.990 eV. The PL peak position of the 0^0 oriented specimen indicates that $\eta \sim 0.3$. These results suggest that the MBE grown material is less inclined to order spontaneously than material growth by MOVPE. This is consistent with the published literature[87]. Figure 3.3.3 shows the PL peak position (and, therefore, the degree of ordering) as a function of substrate orientation. Due to the simultaneous growth method used, see growth details above, the systematic change in the PL peak position may be directly attributed to the change in substrate orientation. This observation implies that spontaneous long-range ordering in GaInP occurs as a consequence of surface, rather than bulk thermodynamic, effects during growth[39]. The shift of the excitonic emission towards the red spectral region with increasing order parameter has been firmly established[65-67]. At 15° formation of the Cu-Pt phase is suppressed, so the

unperturbed Γ_6^c form the lowest lying states and the crystal field splitting of the valence-band is zero[72]. Figure 3.3.3 also shows the PL peak position dependence as a function of substrate orientation for ZnSSe remains largely unaffected, suggesting the propensity to order as a function of substrate orientation is much less. The data for ZnSSe is included for comparative proposes.

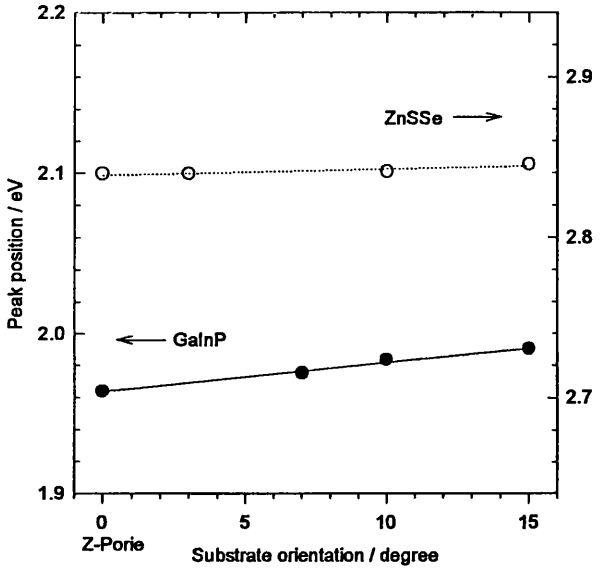

Figure 3.3.3 The dependence of PL peak position on substrate orientation; MBE GaInP and MBE ZnSSe[41] filled and open circles, respectively.

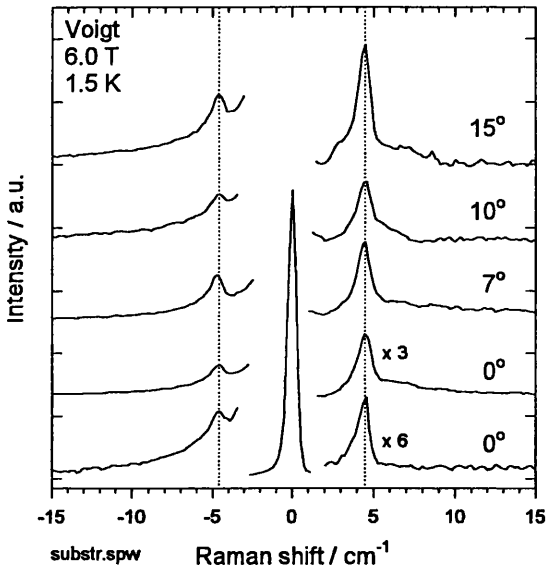

Figure 3.3.4 The upper four spectra show the electron SFRS Stokes and anti-Stokes signals obtained from MBE-grown GaInP epilayers at resonance. The lowest spectrum was obtained off-resonance using 632.8 nm HeNe line.

The most intense SFRS signals were obtained on the high energy side of the excitonic peak. With the exception of the lowest spectrum, figure 3.3.4 shows the resonant electron SFRS spectra obtained for the different substrate orientations. Justification for the assignment of the SFRS signals will be given in the following section. Despite a reduction in bandgap of 26 meV, no discernable change in Raman shift with substrate orientation was detected, indicating that SFRS measurements are completely insensitive to the degree of ordering in the MBE grown $Ga_{0.52}In_{0.48}P$. It is interesting to note that if the prediction of Δ_0 for random (η=0) GaInP and perfectly ordered (η=1) CuPt $GaInP_2$ are correct[71], 0.100 and 0.105 respectively, then a change in the gyromagnetic ratio of a few percent would be expected according to three-band $\boldsymbol{k}\cdot\boldsymbol{p}$ theory. However, the most strongly ordered, 0° substrate, sample was shown above to have an order parameter $\eta \sim 0.3$, therefore no observable change in the gyromagnetic ratio is expected according to the calculation. The electron gyromagnetic ratio for $Ga_{0.52}In_{0.48}P$ determined separately from field dependence measurements was 1.66 ±

0.05[88]. The lowest spectrum in figure 3.3.4 was obtained off resonance by excitation using the 632.8 nm HeNe line. No appreciable narrowing of the SFRS line was observed, despite a reduction in the laser linewidth of ~25 %, suggesting that the linewidth is intrinsic to the SFRS process.

The dependence of excitonic lineshape, linewidth and energetic position was examined as a function of substrate orientation, in epitaxial GaInP grown on GaAs substrates. The PL lineshape was found to be near-Gaussian for all substrate orientations. Comparison with empirically determined data indicated that varying the substrate angle from 15° to 0° produced a corresponding change in the order parameter η from 0 (disordered) to 0.3 (partially ordered), respectively. The FWHM of the disordered MBE material was found to be narrower than that reported for the highest quality MOVPE material, suggesting that the MBE material is of superior quality. In agreement with previous studies a characteristic reduction, attributed to an increase in the ordering of the material, was observed in the energetic position of the excitonic luminescence as the substrate angle was reduced. However, in contrast to previously reported work[63], which found a decrease in the FWHM with the increase in order parameter of the material, the FWHM in the present case is found to increase with increasing order parameter. The observed behaviour is therefore attributed to the dependence of the domain size on substrate orientation, implying, in this instance, that the domain size determines the excitonic linewidth. These findings are in agreement with the phenomenological explanation proposed in reference [39].

The effect that altering the substrate orientation has on the electron gyromagnetic ratio has been examined for the first time. However, the g-value was found to be insensitive to the substrate orientation, despite a 26 meV change in the bandgap energy. Possibly indicating that in this MBE-grown material the domain size is considerably smaller than the excitonic radius. Measurement of the electron gyromagnetic ratio in $Ga_{0.52}In_{0.48}P$ yielded a value of 1.66 ± 0.05. SFRS measurements with the HeNe laser suggest SFRS linewidth obtained is intrinsic to the scattering process.

3.4 The dependence of the electron gyromagnetic ratio in AlGaInP

In this final section the electron gyromagnetic ratio for MBE grown $(Al_xGa_{1-x})_{0.52}In_{0.48}P$ in the composition range $0<x<0.5$ will be determined. The compositional series examined here were grown under the same conditions as those described in the previous section on substrates misoriented by 15° to suppress CuPt-type ordering. There was one exception, however, the x = 0.3 specimen was not from the same growth series as the 15° sample was not available: instead the 10° sample was substituted.

The low temperature PL obtained for the series is presented in figure 3.4.1. As in the previous section for GaInP, the PL is dominated by excitonic emission. The origin of the band at lower energy has been the subject of some controversy, being variously interpreted as defect, impurity and phonon replica related. In appendix C a systematic dependence of the feature on composition is reported, seeming to favour its interpretation as a phonon replica. Since the feature does not exhibit SFRS, it does not form part of the main investigation. It should be noted, however, that the feature

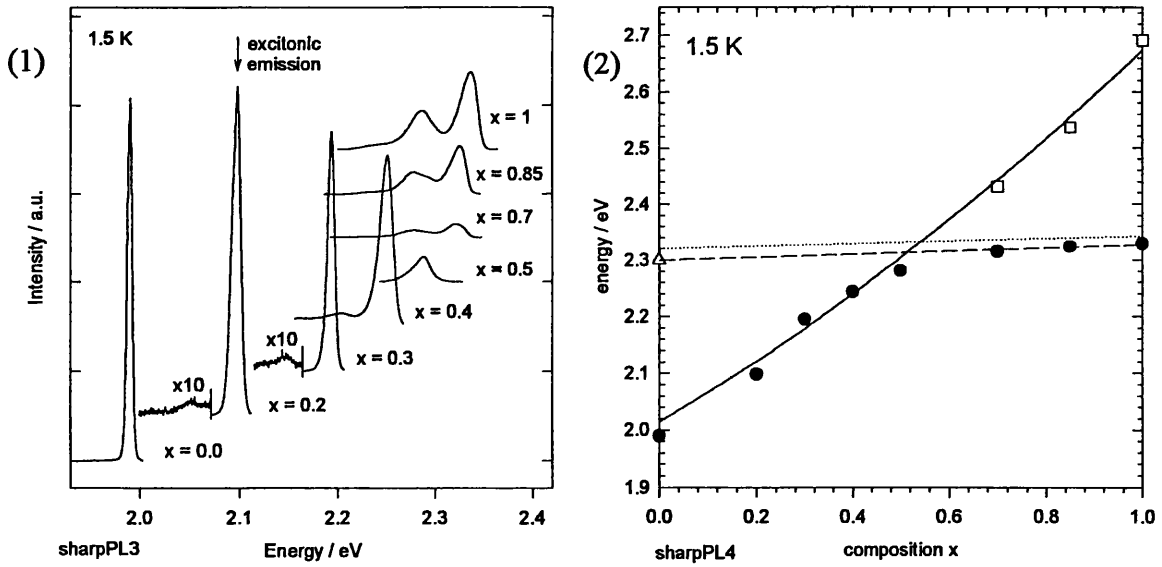

Figures 3.4: (1) Low temperature PL from a series of MBE-grown $(Al_xGa_{1-x})_{0.52}In_{0.48}P$ epilayers, with the composition x indicated in the figure; (2) Compositional variation of the dominant PL peak position. PL (filled circles) and PLE (open squares) data. Solid and dotted lines show the expected direct bandgap[81] and indirect gap variation, respectively. The dotted line indicates the position of the observe luminescence. Triangle indicates position of X-point for GaInP[89].

becomes progressively more pronounced with increasing Al content and the onset of the indirect transition is marked by a strong relative enhancement of the feature.

The direct band-edge variation with composition x, solid line in figure 3.4.2, was determined in earlier work[81], at 5 K, such that:

$$E_0(x) = 2.014 + 0.499x + 0.16x^2 \qquad (3.3)$$

The variation of the indirect gap with composition[90] is indicated by the dotted line, whilst the observed emission is Stokes shifted, dashed line. In $(Al_xGa_{1-x})_{0.52}In_{0.48}P$ the direct-indirect Γ-X band transition occurs at $x_t = 0.50 \pm 0.02$[90,91]. The transition is indicated approximately by the intersection of the dashed and solid lines. For $x > x_t$, the X-band becomes the lowest transition through which excitons may recombine and a distinct 'knee' is formed in the PL emission (filled circles). The direct band-edge is still observed in the PLE[81] (open squares).

The observation of the Stokes and anti-Stokes signals, figure 3.4.3, confirms that the signals are due to SFRS. The SFRS signal strength in Voigt geometry indicates that the origin of the signal is electronic and although electron SFRS is forbidden in Faraday geometry a weakened signal is frequently observed. The partial observation of the electric-dipole selection rules suggests that the assignment made here, and in the previous section, is correct; however, the definitive assignment will be made in the following chapter when the effect of strain on the gyromagnetic ratio is considered. The magnetic field dependence, inset, confirms that the Raman shift behaves according to equation (1.38). In addition to the electron SFRS signals reported in this section further signals were observed for specimens in the range

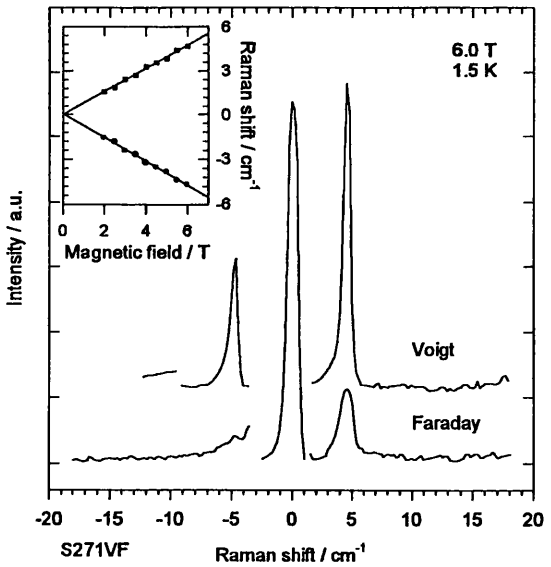

Figure 3.4.3 SFRS spectra from an undoped MBE $(Al_{0.2}Ga_{0.8})_{0.52}In_{0.48}P$ epilayer, in Voigt (upper trace) and Faraday (lower trace) experimental geometries. The inset shows the magnetic field dependence of the SFRS signals.

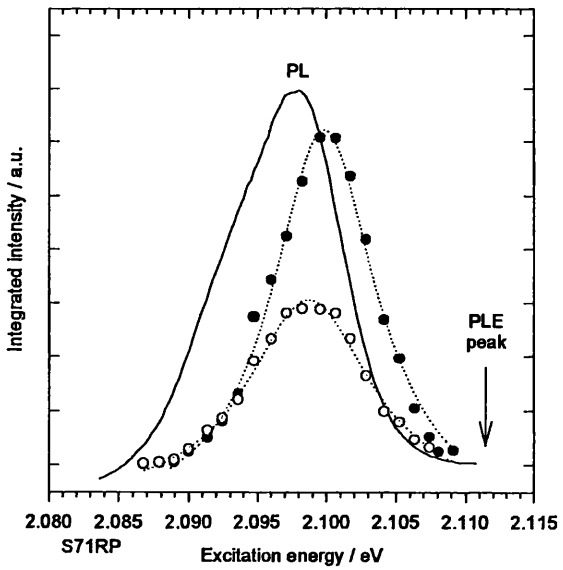

Figure 3.4.4 Stoke (filled circles) and anti-Stokes (open circles) SFRS signal integrated intensity as a function of excitation energy. Solid line is the excitonic PL and dotted lines fitted according to equation (1.39).

$0.3<x<0.5$. These additional signals will be discussed in section 5.2. Excitation of the direct gap by SFRS was also attempted at the points indicated by the PLE data[81] for $x > x_t$, however, no SFRS was observed. Nor was SFRS obtained in resonance with the *X*-band luminescence.

Figure 3.4.4, shows the relationship between the band-edge (arrow)[81], the PL(solid line) and the SFRS resonance profile, for the sample $x = 0.2$. The Stokes and anti-Stokes peaks are indicated by filled and open circles, respectively. The electron SFRS signals show a strong resonant enhancement on the high energy side of the PL peak; similar results were obtained for all the specimens with x equal to 0.5 or less. The linewidth of the SFRS resonance profile and the PL peak are similar, suggesting that they may arise from the same process. Further discussion of this point will be made in section 5.2.

The lower part of figure 3.4.5 shows the electron gyromagnetic ratio dependence on composition determined from the field dependence measurements of the SFRS spectra. The vertical bars indicate the error in the determination of the g-factor. Reflectivity measurements have been used by several groups to determine the spin-orbit splitting $\Delta_0(x)$. However, the consistency between individual data sets is poorer than for the band-edge variation with composition. Using two data sets (*a*)[92] and (*b*)[93] for $\Delta_0(x)$, shown in the upper part of figure 3.4.5, as input for a three-band $\boldsymbol{k \cdot p}$ calcultions, together with equation (3.3) for the bandgap dependence on composition and the following linear interpolation between the binary E_p values[9]:

$$E_p(x) = 21.3 - 2.25x \qquad (3.4)$$

fits to the SFRS experimental data were obtained. Even though the resolution of the SFRS experiment is comparable to the difference between the two data sets, it is clear that data set (*b*)[93] gives the better description of the electron gyromagnetic ratio compositional dependence.

Thus a complete parameter set has been establish that gives good agreement to the experimentally determined electron gyromagnetic ratio for $(Al_xGa_{1-x})_{0.52}In_{0.48}P$. It is interesting to apply this parameter set to estimate the conduction-band effective mass, since the same parameters are required for the $\boldsymbol{k \cdot p}$ calculation. Figure 3.4.6 shows: the solid line obtained using three-band $\boldsymbol{k \cdot p}$ theory in conjunction with the parameter set determined above; the linearly interpolated conduction-band effective masses, InP = 0.077, GaP = 0.15 and AlP = 0.22[94], of the binary materials, dotted line; the

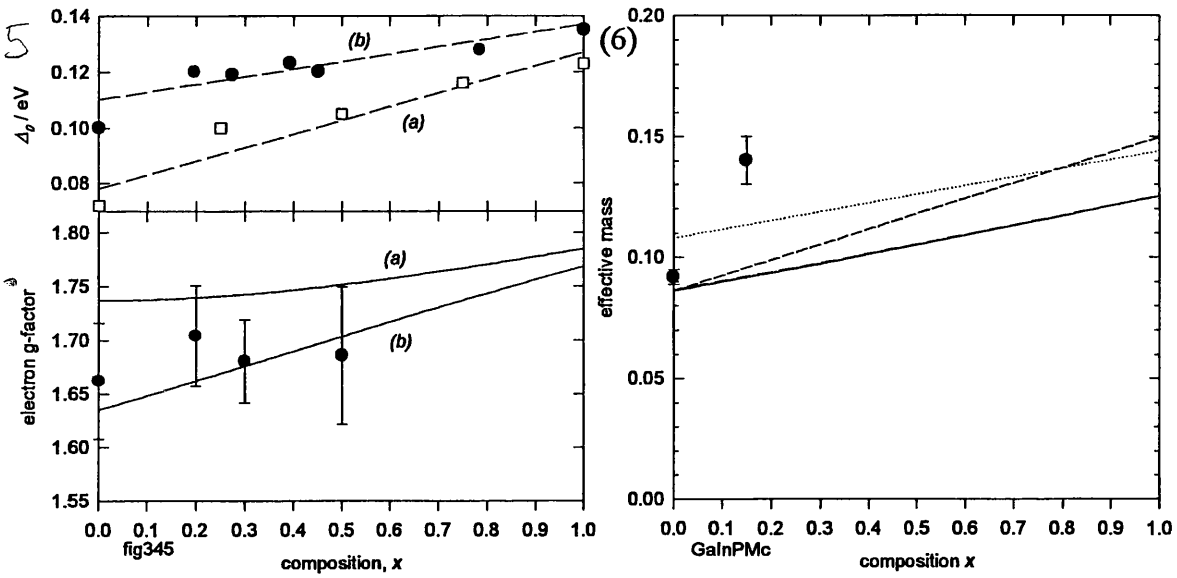

Figure 3.4: (5) The compositional dependence of the spin-orbit splitting Δ_0 (upper portion) and the electron gyromagnetic ratio (lower portion) in undoped MBE-grown $(Al_xGa_{1-x})_{0.52}In_{0.48}P$ epitaxial material. The dashed lines are linear fits to the two data sets (*a*)[92] and (*b*)[93]. The solid line indicates the calculated trend according to three-band ***k·p*** theory; (6) Predictions of the compositional dependence of the conduction-band effective mass for $(Al_xGa_{1-x})_{0.52}In_{0.48}P$ are given: linearly interpolated binary effective masses from end member[9] (dotted line) and ASW bandstructure calculation[95] (dashed line); three-band ***k·p*** theory prediction using the parameter set determined here (solid line); and experimental data (filled circles) obtained by optically detected cyclotron resonance at 6 K[97].

experimental points, filled circles, obtained by optically detected cyclotron resonance at 6 K; the dashed line showing the conduction-band effective mass calculated in reference [95] using a linear interpolation of the effective mass for the binary constituents obtained from *ab initio* augmented spherical wave (ASW) bandstructure method[96]. The present parameter set is in fair agreement with the experimentally determined effective mass for GaInP, though underestimates the predicted trend of the interpolated data sets by approximately 20 %. However, due to the current dearth of experimentally measured effective masses, further analysis is redundant since the data is incapable of finer discrimination.

The first measurements of the electron gyromagnetic ratio in the quaternary alloy system $(Al_xGa_{1-x})_{0.52}In_{0.48}P$ have been reported, in the range $0<x<0.5$. Reasonable agreement was found using the three-band ***k·p*** approximation between the predicted compositional dependence of electron gyromagnetic ratio and the experimentally measured values; justifying this level of approximation. The additional information gained from this investigation of the electron g-factor enabled discrimination between alternative data sets of the spin-orbit splitting parameter. Thus, a complete parameter set was established, allowing the compositional dependence of the effective mass to

be estimated. Fair agreement was found for GaInP with the experimentally determined effective mass, however, the agreement was less good over the rest of the composition range.

Significantly, sharp SFRS spectral features are observed for excitation within the inhomogeneously broadened luminescence, thus demonstrating that SFRS is capable of obtaining a much finer level of information than the inhomogeneous PL linewidth permits in PL experiments.

3.5 Reference

[1] H. Cheng, J. M. DePuydt, J. E. Potts, and T. L. Smith, Appl. Phys. Lett. **52** (1988) 147

[2] H. Cheng, J. M. DePuydt, J. E. Potts, and M. A. Hasse, J. Cryst. Growth **95** (1989) 512

[3] J. E. Potts, H. Cheng, J. M. DePuydt, and M. A. Hasse, J. Cryst. Growth **101** (1990) 425

[4] M. A. Hasse, H. Cheng, J. M. DePuydt, and J. E. Potts, Appl. Phys. Lett. **67** (1990) 448

[5] W. Stutius, J. Cryst. Growth **59**, (1982) 1

[6] P. J. Dean, D. C. Herbert, C. J. Werkhoven, B. J. Fitzpatrick and R. N. Bhargava, Phys. Rev. B **23** (1981) 4888

[7] Y. Zhang, B. J. Skromme and H. Cheng, Phys. Rev. B **47** (1993) 2107

[8] M. Isshiki, T. Kyotani, K. Masumoto, W. Uchida and S. Suto, Phys. Rev. B **36** (1987) 2568

[9] Landolt-Börnstein *'Numerical Data and Functional Relationships in Science and Technology'*, (Springer) 1982

[10] U. W. Pohl, G. H. Kudlek, A. Klimakow and A. Hoffmann, J. Cryst. Growth **138** (1994) 385

[11] C. J. Werkhoven, B. J. Fitzpatrick,S. P. Herko, R. N. Bhargava and P. J. Dean, Appl. Phys. Lett. **38** (1981) 540

[12] T .Taguchi and T. Yao, J. Appl. Phys.**56** (1984) 3002

[13] E. Krause, H. Hartmann, J. Menninger, A. Hoffmann, Ch. Fricke, R. Heitz, B. Lummer, V. Kutzer and I. Broser, J. Cryst. Growth **138** (1994) 75

[14] D. J. Dunstan, J. E. Nicholls, B. C. Cavenett and J. J. Davies, J. Phys. C **13** (1980) 6409

[15] P. A. Fleury and J. F. Scott Phys. Rev. B **3** (1971) 1979

[16] C. M. Townsley, J. J. Davies, D. Wolverson, and P. J. Boyce, G. Horsburgh, T. A. Steele, K. A. Prior, and B. C. Cavenett, Phys. Rev. B **53** (1996) 10983

[17] P. J. Dean, Phys. Status Solidi (a) **81** (1984) 625

[18] K. Shahzad, Phys. Rev. B **38** (1988) 8309

[19] B. J. Skromme, M. C. Tamargo, J. L. de Miguel and R. E. Nahory, Mater. Res. Soc. Symp. Proc. **102** (1988) 577

[20] G. Kudlek, N. Presser, J. Gutowski, S. Durbin, D. Menke, M. Kobayashi and R. L. Gunshor, J. Cryst. Growth **101** (1990) 667

[21] E. Tournie, C. Morhain, G. Neu, J.-P. Faurie, J. Cryst. Growth **184/185** (1998) 520

[22] D. Albert, J. Kraus, S. Einfeldt, J. Nürnberger and D. Hommel, Sol. Stat. Comms. **97** (1996) 909

[23] E. Kurtz, J. Nürnberger, B. Jobst, H. Baumann, M. Kuttler, S. Einfeldt, D. Hommel and G. Landwehr, K. Bethge, and D. Bimberg, J. Cryst. Growth **159** (1996) 289

[24] H. Mayer, U. Rössler, K. Wolf, A. Elstner, H. Stanzl, T. Reisinger and W. Gebhardt Phys. Rev. B **52** (1995) 4956

[25] J. E. Potts, H. Cheng, S. Mohapatra, and T. L. Smith, J. Appl. Phys. **61** (1988) 333

[26] K. Wolf, Ph.D. thesis, Universitat Regensburg, (1994)

[27] K. Wolf, S. Jilka, A. Rosenauer, G. Schutz, H. Stanzl, T. Reisinger, and W. Gebhardt, Appl. Phys. **28** (1995) A120

[28] G. Neu, C. Morhain, E. Tournie, and J.-P. Faurie, Phys. Rev. B **61** (2000) 15789

[29] private communication E. Tournié.

[30] R. N. Bhargava, Bull. Am. Phys. Soc. **32** (1987) 610

[31] T. Yao and Y. Okada, Jpn. J. Appl. Phys. **25** (1986) 821

[32] H. Okuyama, K. Nakano, T. Miyajima, A. Ishibashi and K. Akimoto, Jpn. J. Appl. Phys. **30** (1991) L1620

[33] N. Teraguchi, S. Hirata, H. Mouri, Y. Tomomura, A. Suzuki and H. Takiguchi, J. Cryst. Growth **150** (1995) 803

[34] J. M. Gaines, R. R. Drenten, K. W. Haberern, T. Marshall, P. Mensz and J Petruzzello, Appl. Phys. Lett. **62** (1993) 2462

[35] S. Itoh, N. Nakayama, T. Ohata, M. Ozawa, H. Okuyama, K. Nakano, A. Ishibashi, M. Ikeda and Y. Mori, Jpn. J. Appl. Phys. **32** (1993) L1530

[36] A. Ishibashi and Y. Mori, J. Cryst. Growth **138** (1994) 677

[37] H. Okuyama, Y. Kishita, T. Miyajima, A. Ishibashi and K. Akimoto, Appl. Phys. Lett. (1994) 64904

[38] H. Okuyama, K. Nakano, T. Miyajima, A. Ishibashi and K. Akimoto, J. Cryst. Growth **117** (1992) 139

[39] A. Zunger and S. Mahajan, *'Atomic Ordering and Phase Separation in Epitaxial III-V Alloys in Handbook on Semiconductors'*, Eds. T. Moss and S. Mahajan, vol. 3, ch. 19, (Elsevier Science, Amsterdam, 1994)

[40] Y. Ichimura, K. Kishino, M. Satake, M. Kuramoto and A. Yoshida, J. Cryst. Growth **150** (1995) 812

[41] W.C. Chou, C.S. Yang, A.H.M. Chu, A.J. Yeh, C.S. Ro, W.H. Lan, S.L. Tu, R.C. Tu, S.C. Chou, Y.K. Su and W.Y. Uen, J. Appl. Phys. **84** (1998) 2245

[42] L.H. Kuo, L. Salamanca-Riba, B.J. Wu, J.M. DePuydt, G.M. Haugen, H. Cheng, S. Guha and M.A. Hasse, APL **65** (1994) 1230

[43] T. Maruyama, T. Ogawa, K. Akimoto, Y. Kitajima, S. Itoh and A. Ishibashi, JCG **159** (1996) 41

[44] B. Jobst, S. Strauf, P. Baume, E. Kurtz, H. Schenk, D. Hommel and G. Landwehr, Int. Sym. Blue Laser and light Emitting Diodes, Chiba Univ., Japan, March 5-7, 1996, We-P01

[45] H. J. Chen, D. Y. Lin, Y. S. Huang, R. C. Tu, Y. K. Su and K. K. Tiong, Chinese J. Phys. **36** (1998) 533

[46] S. A. Permogorov and A. Reznitsky, J. Luminescence 52 (1992) 201

[47] H. J. Chen, D. Y. Lin, Y. S. Huang, R. C. Tu, Y. K. Su and K. K. Tiong, Semicond. Sci. Technol. **14** (1999) 85

[48] E. Oh, S. D. Lee, H. D. Jung, M. D. Kim, H. S. Park, B. J. Kim and T. I. Kim, IOP Conference Series **145** (1996) 319

[49] D. J. Olego, K. Shahzad, D. A. Cammack, H. Cornelissen, Phys. Rev. B **38** (1988) 5554

[50] U. Lunz, C. Schumacher, J. Nürnberger, K. Schüll, A. Gerhard, U. Schüssler, B. Jobst, W. Faschinger and G. Landwehr Semicond. Sci. Technol. **12** (1997) 970

[51] J.J. Davies, D. Wolverson, I.J. Griffin, O.Z. Karimov, C. Orange, D. Hommel and M. Behringer, Phys. Rev B **62** (2000) 10329

[52] D. Wolverson, J.J. Davies, C. Orange, K. Ogata, Sz. Fujita, Sg. Fujita, K. Nakano, H. Okuyama, S. Itoh, B. Jobst and D. Hommel, Phys. Rev. B **60** (1999) 13555

[53] B. Vogele, C. Morhain, B. Urbaszek, S. A. Telfer, K. A. Prior, and B. C. Cavenett, J. Cryst. Growth **201/202** (1999) 950

[54] P. Y. Yu and M. Cardona, '*Fundamentals of Semiconductors*' (Springer-Verlag, Berlin, 1996)

[55] L. Vegard, Z. Phys. **5** (1921) 17

[56] P. Bellon, J.P. Chevalier, E. Augarde, J.P. Andre and G.P. Martin, J. Appl. Phys. **66** (1989) 2388

[57] T. Suzuki and A. Gomyo, J. Cryst. Growth 99 (1990) 60

[58] R.P. Schneider, Jr. E.D. Jones, J.A. Lott and R.P. Bryan J. Appl. Phys. **72** (1992) 5397

[59] S.R. Kurtz, J.M. Olson, D.J. Arent, A.E. Kibbler, and K.A. Bertness, Proc of Mat. Res. Soc. Symp., (Mat. Res. Soc., Pittsburgh, 1993, p.83)

[60] A. Gomyo, T. and Suzuki, Phys. Rev. Lett. **60** (1988) 2645

[61] U. Kops, P.G. Blome, M. Wenderoth, R.G. Ulbrich, C. Geng and F. Scholz, Phys. Rev. B **61** (2000) 1992

[62] U. Dörr, H. Kalt, W. Send, D. Gerthsen, D.J. Mobray and C.C. Button, Phys. Rev. Lett. **73** (1998) 1679

[63] Y. Zhang, A. Mascarenhas, S. Smith, J.F. Geisz, J.M. Olson and M. Hanna, Phys. Rev. B **61** (1999) 9910

[64] U. Kops, R.G. Ulbrich, M. Berkard, C. Geng, F. Scholz and M. Schweizer, Phys. Stat. Sol. (a) **164** (1997) 159

[65] T. Kurimoto and N. Hamada, Phys. Rev. B **40** (1989) 3889

[66] T. Kanata, M Nishimoto, H. Nakayama and T. Nishino, Phys. Rev. B **45** (1992) 6637

[67] D.J. Mowbray, R.A. Hogg, M.S. Skolnick, M.C. Delong, S.R. Kurtz and J.M. Olson, Phys. Rev. B **46** (1992) 7232

[68] G.S. Honer, A. Mascarenhas, S. Froyen, R.G. Alonso, K. Bertness and J.M. Olson, Phys. Rev. B **47** (1993) 4001

[69] R.G. Alonso, A. Mascarenhas, S. Froyen, G.S. Honer, K. Bertness and J.M. Olson, Sol Stat. Commun. **85** (1993) 1021

[70] R.L. Forrest, T.D.Golding, S.C. Moss, Y. Zang, J.F. Geisz, J.M. Olson, and A. Mascarenhas, Phys. Rev. B **58** (1998) 15355

[71] S.-H. Wei and A. Zunger, Phys. Rev. B **39** (1988) 3279

[72] K. Sinha, A. Mascarenhas, R.G. Alonso, G.S. Honer, K. Bertness, S.R. Kurtz and J.M. Olson, Sol Stat. Commun. **89** (1994) 843

[73] S.R. Kurtz, J.M. Olson and A.E. Kibbler, Appl. Phys. Lett. **57** (1990) 1922

[74] M. Kondow, H. Kaklbayashi, S. Minagawa, Y. Inoue, T. Nishino and Y. Hamakawa, Appl. Phys. Lett. **53** (1988) 2053

[75] T. Suzuki, A. Gomyo, S. Iijima, K.Kobayashi, S. Kawata, I. Hino and T. Yusa, Jpn. J. Appl. Phys. **27** (1988) 2098

[76] P.J. Parbrook, M.Ishikawa, Y. Nishikawa, S. Saito, M. Onomura and G. Hatakoshi, J. Cryst. Growth **150** (1995) 749

[77] J.S. Kim, S.H. Suh, C.H. Kim and S.J. Chung, J. Appl. Phys. 81 (1997) 6107

[78] J.F. Lin, M.C. Wu M.J. Jou, C.M. Chang and B.J.Lee, J. Electro-chem. Soc **142** (1995) 1293

[79] M.P. Halsall, A.D.F. Dunbar and U. Bangert, J. App. Phys. **85** (1999) 199

[80] O.P. Kowalski, R.M. Wegerer, D.J. Mowbray, M.S. Skolnick, M Hopkinson, C.C. Button, J.S. Roberts, J.P.R. David and, Appl. Phys. Lett. **68** (1996) 3266

[81] S.P. Najda, A.H. Kean, M.D. Dawson and G. Duggan, J. Appl. Phys. 77 (1995) 3412

[82] C. Meenakarn, A.E.Staton-Bevan, M.D. Dawson and G. Duggan, A.H. Kean and S.P. Najda, Inst. Phys. Conf. Ser. No 157 Microsc. Semicond. Mater. Conf, Oxford (1997)

[83] M.D. Dawson and G. Duggan, Phys. Rev. B **47** (1993) 12598

[84] I. Pietzonka, T. Sass, R. Franzheld, G. Wagner and V. Gottschalch, J. Cryst. Growth **195** (1998) 21

[85] E.F. Schubert, E.O. Göbel, Y. Horikoshi, K. Ploog and H.J. Queisser, Phys. Rev. B **30** (1984) 813

[86] E.D. Jones, R.P. Schneider, S.M. Lee and K.K. Bajaj, Phys. Rev. B **46** (1992) 7225

[87] F. Scholz, C. Geng. M. Burkard, H.-P. Gauffel, H. Schweizer, R. Wirth, A. Moritz and A. Hangleteiter, Physica E **2** (1998) 8

[88] I.J. Griffin, D. Wolverson, J.J. Davies, M. Emam-Ismail, J. Heffernan, A.H. Kean, S.W. Bland and G. Duggan, Semicond. Sci. Technol. **15** (2000) to be published

[89] A.R. Goni, K. Syassen, K. Strossner and M. Cardona, Phys. Rev. B **39** (1989) 3178

[90] D.J. Mowbray, O.P. Kowalski, M Hopkinson, M.S. Skolnick and J.P.R. David, Appl. Phys. Lett. **65** (1994) 213

[91] J.S. Nelson, E.D. Jones, S.M. Myers, D.M Follstaedt, H.P. Hjalmarson, J.E. Schirber, R.P. Schneider, J.E. Fouquet, V.M. Robbins and K.W. Carey, Phys. Rev. B 53 **15** (1996) 893

[92] S. Adachi, S. Ozaki M. Sato and K Ohtsuka, Jpn. J. Appl. Phys. 35 537 (1996)

[93] K. Asami, H. Asahi, S.-I. Gonda, Y. Kawamura and H Tanaka, Sol. Stat. Comm. **70** (1989) 35

[94] A.T. Meney, A.D. Prins, A.F. Phillips, J.L. Sly, E.P. O'Reilly, D.J. Dunstan, and A.R. Adams and A. Valster, IEEE J. Quantum Electronics **1** (1995) 1077

[95] M.P.C.M. Krijn, Semicond. Sci. Technol. **6** (1991) 27

[96] A.P. Williams, J. Kubler and C.D. Gelatt, Phys. Rev. B **19** (1979) 6094

[97] P. Emanuelsson, M. Drechsler, D.M. Hofmann and B.K. Meyer, M. Moser and F. Scholz, Appl. Phys. Lett. 64 (1994) 2849

Chapter 4 - Holes

Holes provide a sensitive probe of the local semiconductor environment. In this chapter the behaviour of holes is examined and their unique properties are exploited to gain a deeper insight into the nature of binary, ternary and quaternary alloys.

The first section begins with a brief summary of p-type doping in ZnSe. This is followed by consideration of a possible phosphorus compensation process in ZnSe. In the second section the first report of hole SFRS from lithium acceptors in ZnSe is made. The third section is chiefly concerned with the effects of strain on hole SFRS. The properties of the acceptor valence-band Hamiltonian are established and then applied to a ZnSe epilayer with a small residual strain. In the fourth and fifth sections strain induced anisotropies are used to identify definitively the origins of the SFRS signals in ZnMgSe and GaInP, respectively. Finally, in the sixth section, the compositional dependence of the hole signals in MOVPE-grown AlGaInP material are presented.

4.1 Compensation in ZnSe

Arguably, the technological application of ZnSe has, for the last three decades, been hindered by the difficulty in achieving reliable p-type doping. This section begins with a brief summary of p-type doping issues in ZnSe, with particular attention paid to acceptor compensation. The extensively studied N compensation process will be discussed, then evidence of P compensation will be considered.

The acceptors in ZnSe are formed by group-I and group-V elements. The group-V elements are N[1-5], P[5,6] and As[7,8] substituted on the Se sites, and the group-I, alkali metals, such as Li[9-11] and Na[12] act as substitutional acceptors on Zn sites. The results of p-type doping for epitaxial ZnSe are summarized in table 4.1 below and the ionisation energies for the acceptor discussed are given in table 3.1. Most attempts to dope ZnSe with P and As by conventional methods have resulted in the formation of deep compensating centres, leading to semi-insulating material[13,14]. Li is thought to be amphoteric and is also believed to form compensating interstitial donors[15,16]: this is supported by theoretical calculation[17]. Doping with Na is similar to doping with Li; however, due to its larger covalent radius Na incorporates less well into ZnSe.

The best results in terms of reliability and highest carrier concentration have been obtained by the method of plasma-excited nitrogen doping during MBE growth. However, this is not without difficulty, since the free hole concentration seems to be

limited by a very efficient compensation process[19]. The free hole concentration saturates with increasing N doping at about 1 x 10^{18} cm^{-3}. The N doped material shows strong DAP emission, although donors were not intentionally incorporated and two independent DAP emission processes were observed. These observations led to the proposal of many theoretical models[20-23] involving compensating nitrogen donors, generated by heavy N doping. The existence of a deep compensating donor state was definitively identified using SFRS[24,25]. The results of SFRS investigation support a deep donor model consisting of a N-related complex involving Se vacancies[26-28]. Recently, evidence supporting the existence of a N-related shallow donor compensation has also been reported, which is believed to form even in the initial stages of N incorporation[26,29]. Thus, compensation of nitrogen-doped ZnSe has been extensively studied. However, it is not known if the phenomena is confined solely to N or extends to the alternative p-type dopants. In the following evidence of P compensation is examined.

Group	Element	Dopant	$N_A - N_D$ / cm^{-3}	Growth
I	Li	t-C_4H_9Li	~10^{16}	MOVPE[9]
		Li	~5 x 10^{17}	MBE[10,11]
	Na	C_5H_5Na	-	MOVPE[12]
V	N	NH_3	~10^{14}	MOVPE[1]
		Plasma N_2	~10^{16} – 10^{18}	MBE[2,3]
		t-$C_4H_9NH_2$	~10^{17} – 10^{18}	MOVPE[4]
	P	PH_3	-	MOVPE[5]
		Zn_3P_2	-	MBE[6]
	As	AsH_3	-	MOVPE[7]
		As	-	MBE[8]

Table 4.1 Summary of p-type doping in ZnSe[18]

The samples under investigation in this section were grown by MBE in Bremen using a novel co-doping method[30], via the sublimation of solid source GaP in a decomposition cell. The flux was controlled by the temperature of the decomposition cell, see sample details appendix B. However, despite Ga atoms being the minor flux species the sticking coefficient of atomic Ga to ZnSe is high compared with that of P_2 molecules[30], leading to greater Ga incorporation in the epilayer than P. The doping concentrations presented in appendix B were determined by capacitance-voltage (C-V) profiling[30].

The relative prominence of the FE in the photoluminescence of S116, figure 4.1.1, indicates that the epilayer is of high quality, with a low concentration of impurity

species[31-33]; furthermore, observation of the Y-line[34] at 2.604 eV (not shown) supports this assertion. The Y-line is a defect associated with emission from an exciton bound to a misfit dislocation[35] and is generally only observed in lightly doped material[34]. Given the prevailing dopant species, the dominant peak in the spectrum, at 2.7973 eV, is attributed to the D^0X emission of the Ga shallow donor. No A^0X luminescence or hole SFRS, in the vicinity of A^0X, and only weak DAP emission was observed from this sample, indicating the P is present only in small quantities, or that the P present is not active as a shallow acceptor. Confidence in the assignment of D^0X^{Ga} enables the strain state of the epilayer to be accurately determined. The shift in the energetic position of D^0X^{Ga} luminescence to slightly lower energy indicates a small biaxial tensile strain of less than +0.1 %[36]. This strain is consistent with the layer thickness of 1.7 μm and with the position and linewidth of the FE. The origin of the weak shoulder on the low energy side of D^0X^{Ga} is less clear, however, and has been subject to speculation[37,38]. Selective excitation, see inset figure 4.1.1, has been used to precisely determine the position of this line at 2.7963 eV. The position of the lower energy peak corresponds closely to the shallow donor peak observed in the ZnSe:P Valbonne sample (figure 3.1.2). A high resolution SFRS resonance profile was performed to establish the nature of the centre, see figure 4.1.2. Fitting the data using equation (1.39) reveals two well resolved features in the resonance profile. The Stokes (open circles) and anti-Stokes (filled circles) peaks are offset from one another

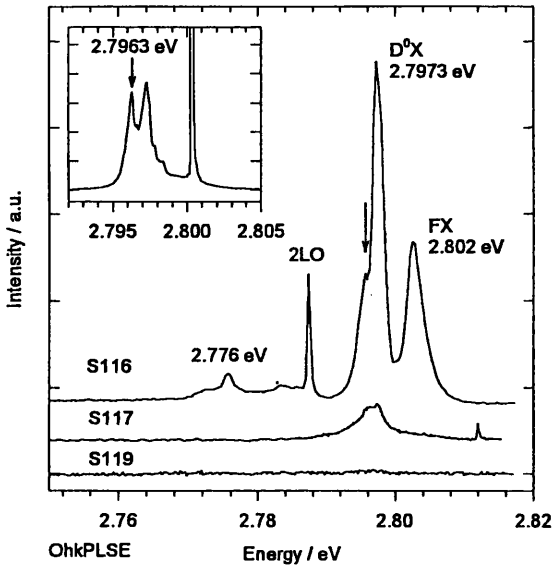

Figure 4.1.1 Low temperature PL from co-doped ZnSe:Ga:P. Inset show the selective excitation of D^0X. The truncated feature at 2.801 eV is the laser line.

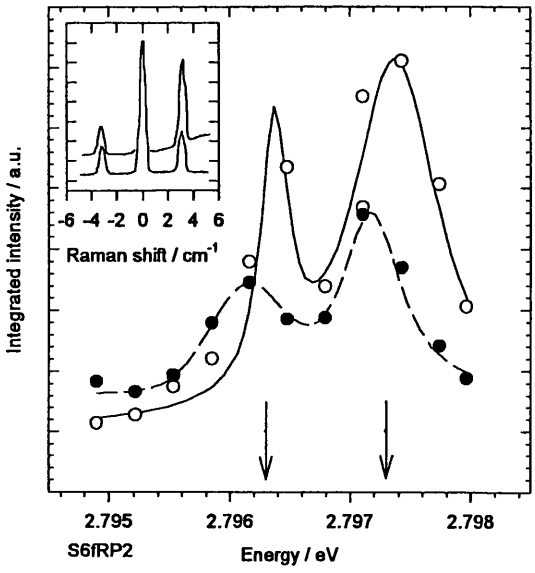

Figure 4.1.2 The SFRS Stokes (open circle) and anti-Stokes (filled circle) resonance profile, fitted using equation (1.39). Inset shows SFRS spectra from each peak in the vicinity of D^0X.

by an energy of ~0.3 meV, with the midpoints corresponding precisely with their peaks in the selective excitation, these positions being indicated by the arrows. The spin-flip Raman spectra, inset figure 4.1.2, show the SFRS signals at resonance for each peak, the upper and lower spectra corresponding to the excitation energies 2.7973 eV and 2.7963 eV, respectively. The gyromagnetic ratio of ~1.12 identifies both peaks in the PL as being shallow donor related.

The ratio of intensities of the lines in the PL does not support either a strain-split or an excited donor state as was put forward in the case of the Regensburg sample, section 3.1, since in the latter case the lower energy line, corresponding to the ground state, would be the most intense on thermal grounds. Similarly, the line cannot be accounted for by the other principal donor impurities, which differ from D^0X^{Ga} by only 0.5 meV at the most. In the present case the separation is 1 meV. Recently, however, shallow compensating donor complexes have been reported in lightly N-doped ZnSe[39,40], with binding energies slightly larger than those of the substitutional shallow donors, but which in other respects behave exactly like effective mass donors. According to Haynes's rule[41] the donor binding energy should be directly proportional to the binding energy of an exciton bound to the neutral donor. For shallow donors in ZnSe the constant of proportionality is 0.19[24], therefore, from the donor depth a binding energy of 30.5 meV is determined, taking into account the residual strain in the epilayer.

Several compensation mechanisms have been proposed which could give rise to shallow N compensation, including N in interstitial configurations[36,37], doubly ionised N atom on a zinc site, N_{Zn}^{2+} and, interestingly, after establishing a link between doping with molecular N_2 and the formation of a shallow donor centre[23], $(N_2)_{Zn}$. The latter candidate may have some validity in the present case of P-doping, since it is diatomic P that arrives at the growth surface during epitaxy and the details of P_2 incorporation have not been established.

A brief summary of doping issues in ZnSe epilayers has been made, with particular emphasis being drawn to the compensation process and evidence for a possible compensation process involving the p-type dopant phosphorus has been considered. The SFRS measurements of the gyromagnetic ratio identify the feature on the low energy side of D^0X^{Ga} as being shallow donor related. The precise determination of the energetic position of the feature by selective excitation and by SFRS resonance profile has enabled the binding energy, which is slightly larger than the principal

substitutional donors, to be estimated. The observation of the feature in the PL of this Ga:P-doped specimen, and the presence of a similar feature in the PL of the Valbonne and other P-doped material[37,38] suggests that P may form a shallow compensating donor and, given the doping concentration of this particular specimen, that the compensation process occurs even at the initial stages of doping[29]. Several possible compensation mechanisms have been proposed, one of which seems particularly relevant since it involves the incorporation of diatomic molecules. Determination of the compensation mechanism is beyond the scope of this work. However, angle resolved SFRS studies and phonon Raman spectroscopy may prove essential in establishing the viability of a diatomic incorporation of P on the grounds of the reduced symmetry of the centre.

4.2 Lithium doped ZnSe

In this section the discussion will be extended to another alternative p-type dopant, lithium. Lithium doped ZnSe has not previously been subject to SFRS investigation and as a consequence important electronic bandstructure parameters have not yet been determined. The salient features in the PL spectra of a high quality series of bulk p-type ZnSe:Li samples will then be discussed, followed by an investigation of the hole SFRS exhibited by these bulk samples.

Figure 4.2.1 shows the low temperature PL from a series of p-type bulk specimens grown by vapour phase transport. The prominence of I_1^d indicates that all of the samples were grown under Se-rich conditions; however, the variation in the intensity of the excitonic features suggests that the doping was not precisely controlled. Observation of the FE suggests that the samples were lightly doped and this is confirmed by comparison with the PL from characterized ZnSe:Li[43], which indicate that the $|N_A - N_D|$ is ~$1x10^{15}$ cm^{-3} or less for the series. The sharpness of the bound exciton lines and their energetic positions[45,46] indicated that the samples are strain-free, and the narrow linewidths together with the absence of red emission indicate that the samples are of high structural quality. At low temperature and in zero magnetic field the A^0X^{Li} emission line shows a threefold fine structure[47] (not resolved in figure 4.2.1) the origin of which has been attributed to the interaction of the bound particles[48-50]. The Zeeman splitting of this fine structure has been subject to detailed investigation for these samples[47]. The two samples, K106 and K5, with fairly prominent A^0X and D^0X lines also exhibit relatively strong DAP emission at ~2.692

eV, as described in chapter 3.1. Sample K52 has the weakest overall emission and certainly the weakest D^0X emission. Sample U17 showed no DAP luminescence.

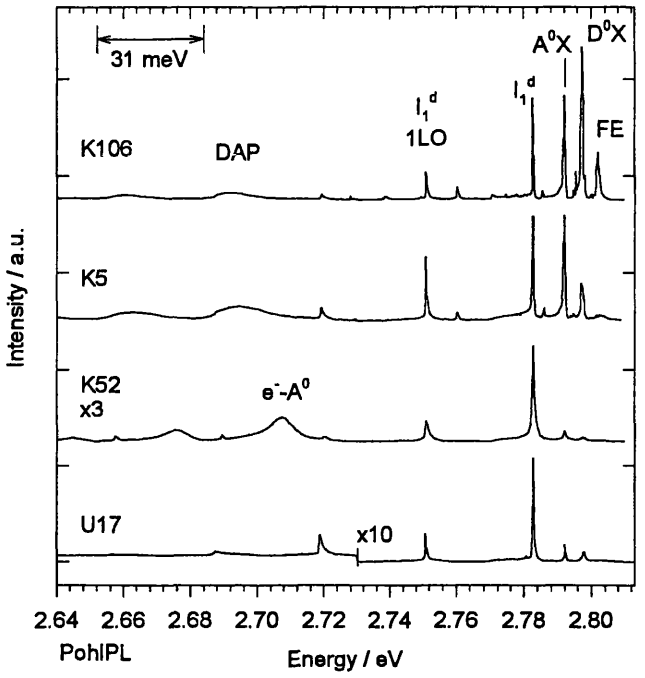

Figure 4.2.1 Low temperature luminescence from bulk ZnSe crystals, grown by vapour phase transport[44]. The 31 meV ZnSe LO phonon energy is indicated in figure.

Instead of the more commonly reported DAP recombination, sample K52 exhibits free-to-bound, conduction-band-to-acceptor (e^--A^0), recombination at ~2.71 eV, figure 4.2.1. Conduction-band-to-acceptor emission is known to occur at low temperatures in ZnTe[51] and is a frequently occurring feature in successfully p-doped ZnSe. In earlier work the peak at ~2.71 eV was believed to derive from recombination between interstitial Li donors and substitutional Li acceptors on Zn sites(Li_i – Li_{Zn}), the so called R-band[52]. However, characterisation by temperature dependent PL and magnetoluminescence have firmly established[43] the e^--A^0 hypothesis. Further, no direct optical evidence was found to support Li donors in MBE-grown ZnSe[43]. According to the model[43], e^--A^0 emission becomes observable at low temperatures whenever the shallow donor concentration is low enough that the DAP recombination pathway is saturated by the filling the donor levels, even at low excitation intensities, so that the additional photoexcited electrons are forced into the conduction-band. This model is consistent with the observed spectra in figure 4.2.1. Observation of the e^--A^0 peak is useful, since it enables the acceptor binding energy to be determined directly. From the position of the e^--A^0 peak at 2.7076 eV, a Li acceptor binding

energy of 114.2 meV is readily determined in close agreement with the theoretical prediction, 110.1 meV[53], and the experimental value, see table 3.1.

All of the bulk samples exhibited shallow donor SFRS in resonance with FE and D^0X, and hole SFRS was also observed from all of the samples. Unexpectedly, two samples, U17 and K5, exhibited additional SFRS signals in resonance with D^0X and FE; these signals, not previously reported in ZnSe, will be discussed in appendix D. The remainder of this section will be solely concerned with hole SFRS.

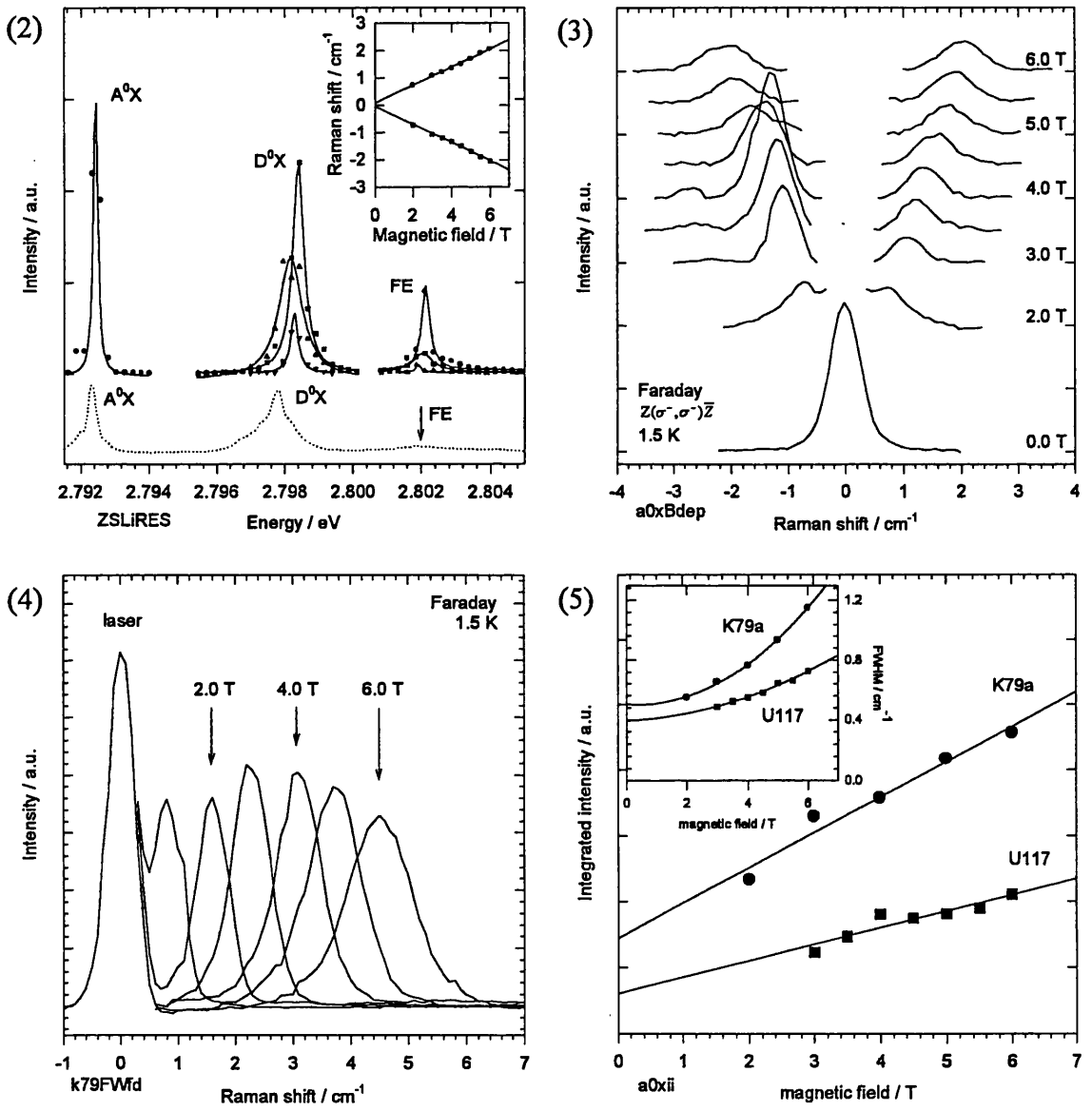

Figure 4.2: (2) SFRS resonance profile of the ZnSe:Li excitonic region. Solid lines are fits to SFRS data, the dotted line indicates the PL. The inset shows the Faraday magnetic field dependence of signal in resonance at A^0X; (3) Hole SFRS spectra from which magnetic field dependence data (inset in adjacent figure) was derived. Magnetic field strength indicated in the figure; (4) Stokes hole SFRS signals in resonance with A^0X in ZnSe for various magnetic field strengths. The left most feature is the laser line; (5) The integrated intensity and FWHM (inset) as a function of magnetic field strength, for the signals presented in figure 4.2.4.

In order to precisely determine the origin of the SFRS signals a resonance profile was performed on sample U17. Figure 4.2.2 shows that resonant SFRS signals were observed for all of the excitonic emission centres; the PL (dotted line) is included in this figure for comparison. SFRS signals with a Raman shift of ~2 cm^{-1} were observed with a pronounced resonant enhancement when the laser energy was coincident with the energy of the acceptor bound exciton transition, indicating that these signals arise from spin-flip of holes at neutral acceptors[49]. The Faraday magnetic field dependence, inset figure 4.2.2, confirms that the signal behaves according to equation (1.38). In figure 4.2.3, the hole SFRS spectra from which the magnetic field dependence was derived are presented. The anti-Stokes signal passes through a distinct resonance.

In contrast to the shallow donor related SFRS, the hole SFRS FWHM and integrated intensity display a distinct and characteristic magnetic field dependence. Figure 4.2.4 shows the SFRS spectra for the nitrogen doped sample K79a at several magnetic field strengths, whilst figure 4.2.5 shows the integrated intensity and FWHM for samples K79a(open circles) and U17(filled circles). For both samples the integrated intensity decreases as the field is reduced, but remains finite at zero magnetic field. However, the caveat concerning the appropriateness of the experimental procedure for determining the integrated intensity expressed in the latter part of section 3.1 is equally valid here. The hole FWHM is composed of the residual SFRS linewidth plus an additional inhomogeneously strain broadened field dependent component. The randomised strain distribution introduces a spread of g-values, which results in a linear broadening of FWHM with increasing magnetic field. At 6 Tesla the FWHM is accounted for by a randomised strain distribution of approximately 80 μeV. Note that, in contrast to the shallow donor SFRS reported in section 3.1, a significant difference in the magnitude of the respective FWHM is exhibited by the two specimens at 6.0 T. This is attributed to the sensitivity of the hole to the local semiconductor environment.

The results of the circular polarization measurements are shown in figure 4.2.6 and are consistent with those for holes[49,54]. The SFRS spectra were excited on the low energy side of the A^0X; thus avoiding deconvolution difficulties associated with the A^0X manifold, as the A^0X PL was not excited. Hence, the anti-Stokes SFRS signal is the dominant line in the SFRS spectra.

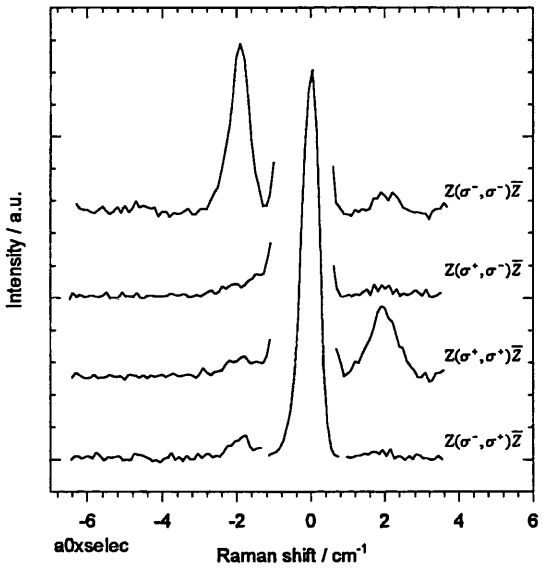

Figure 4.2.6 Circular polarisation measurements of hole SFRS spectra for ZnSe:Li.

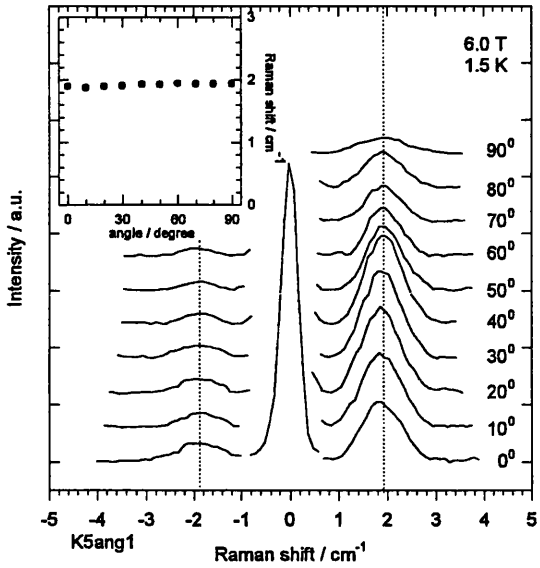

Figure 4.2.7 Bulk ZnSe:Li hole SFRS signal dependence on orientation of the sample with respect to the magnetic field direction.

Figure 4.2.7 shows the angular dependence of the hole SFRS signal and indicates that the sample is indeed strain-free. However, since strain forms the subject of the following section the result will not be discussed further here.

The hole gyromagnetic ratio determined in this investigation was 0.72 ± 0.03. This is in close agreement with the g-value $|g_N| = 0.7 \pm 0.09$ obtained for N acceptor in unstrained ZnSe:N epilayers[55]. This agreement is not coincidental, since both N and Li have similar binding energy depths. The Zeeman spectroscopy conducted on these same samples obtained a lithium acceptor ground state g-value of 0.6[47]. The origin of the disparity is not clear, however, it should be noted that SFRS results, involving only the spin states of the acceptor, are significantly simpler to model than the results of Zeeman spectroscopy studies, which involve the spin states of both the acceptor and the acceptor-bound exciton and therefore require more terms in the spin-Hamiltonian. In previous work[25], an anomalous SFRS signal was detected with a g-value of 0.86 ± 0.07, in Li-doped ZnSe grown by atomic layer epitaxy (ALE). This present work suggests that the signal may be attributed to the spin-flip of a hole.

In summary, the first observation of the lithium acceptor spin-flip signal is reported, with spin Hamiltonian parameters similar to those of nitrogen acceptors. The identification is supported by polarization measurements and a resonant Raman profile of the SFRS signals, which reached a maximum in the vicinity of the acceptor

bound exciton. The results obtained augment those of previous experiments, in which the Zeeman splitting of the excitonic features were studied[47].

The magnetic field dependence of acceptor bound hole SFRS was also investigated. The FWHM and integrated intensity of two specimens were examined and although the magnitudes were found to differ the systematic trends were the same, that is, the FWHM suffered field dependent inhomogeneous broadening, whilst the integrated intensity displayed a quadratic field dependence, but remained finite at zero field. These results reflect the greater sensitivity of the hole to its local environment, produced by the relatively small extent of the hole wavefunction.

4.3 Strain in epitaxial material

Whilst PL is a suitable technique for determining large tensile or compressive strains, it has already been demonstrated in chapter 3 that strain measurements based solely on PL may fail due to the inhomogeneous broadening of free and bound exciton lines in heavily doped material or even the disappearance of those lines in some cases. In the following section the effect of strain on the hole gyromagnetic ratio will be examined. A suitable Hamiltonian describing the effects of strain and spin on the valence-band is discussed. This Hamlitonian is then applied to an epilayer with a small residual strain.

The spin and strain Hamiltonians, presented in chapter 1, may be combined in order to describe the acceptor valence-band states:

$$H_v = H_{spin} + H_{strain} = -2\mu_B[\tilde{\kappa}\,(J_x B_x + J_y B_y + J_z B_z) + \tilde{q}(J_x^3 B_x + J_y^3 B_y + J_z^3 B_z)] + (\Delta/2)(J_z^2 - J[J+1]/3) \qquad (4.1)$$

where μ_B is the Bohr magneton and Δ is the strain induced heavy-hole and light-hole energy splitting in zero magnetic field[56]. The dimensionless isotropic parameters $\tilde{\kappa}$ and $\tilde{q}$ for the acceptor can, in principle, be determined from the SFRS spectra.

The form of H_v implies that if $|\Delta| >> \mu_B \tilde{\kappa} B$ then the strain is dominant and the field induced changes in the light-hole and heavy-hole states are essentially independent of the exact value of strain. Typically, for thick epilayers of ZnSe on GaAs, cooling from the growth temperature to 1.5 K introduces a biaxial tensile strain of about +2 meV[57,58], as a result it is the heavy-hole state, that forms the lowest lying state and will consequently be occupied at low temperatures. For thin layers, compressive strain produced by the difference in lattice constants, of the similar magnitude, but of

opposite sign, inverts the energy levels and it is the light-hole states that become occupied. In contrast, in the case of small strain splitting, Δ becomes comparable to Zeeman splitting $\mu_B \tilde{\kappa} B$, the heavy-hole and light-hole states become mixed and the Raman shift becomes sensitive to the precise value of Δ[59]. Studies on epilayers of intermediate thickness[60,61], and therefore small strains, have shown that Δ, $\tilde{\kappa}$ and $\tilde{q}$ may be more accurately determined than for heavily strained layers.

Analytical solutions[56] to the Zeeman terms are given in table 4.2 for the magnetic field orientated parallel (Faraday) and perpendicular (Voigt) to the growth axis[001]. Intermediate values, including the strain term, were obtained using a suitable matrix diagonalisation routine.

Geometry	light hole states	heavy hole states
Faraday	$\pm \mu_B \mathbf{B} (\tilde{\kappa} + \tilde{q}/4)$	$\pm 3 \mu_B \mathbf{B} (\tilde{\kappa} + 9\tilde{q}/4)$
Voigt	$\pm 2 \mu_B \mathbf{B} (\tilde{\kappa} + 5\tilde{q}/2)$	$\pm 3 \mu_B \mathbf{B} (\tilde{q}/2)$

Table 4.2 Solutions of the Zeeman terms equation 4.1 for the magnetic field orientated parallel (Faraday) and perpendicular (Voigt) to the growth axis[001].

It is plain from the analytical solutions that equation (4.1) predicts anisotropic behaviour for the hole in the presence of a biaxial strain. Furthermore, the light-hole and heavy-hole, due to their different anisotropic dependences on the orientation of the sample to the direction of the magnetic field, can readily be distinguished from one another.

The experimental results obtained for N-doped ZnSe epilayers[62] are summarized in table 4.3. The ranges of epilayer thickness quoted are intended only as a guide, since the actual strain induced, and therefore the observed Raman shift, is critically dependent on the prevailing growth conditions.

Biaxial strain	Thickness (μm)	Faraday	Voigt	Observed behaviour
Compressive(-)	< 0.5	~ 2.4	4.5 - 5	heavy-hole
Tensile(+)	> 0.8	7 - 7.5	0	light-hole
Negligible	0.45 - 0.85	5 - 6	2 - 3	mixed state

Table 4.3 Summary of acceptor Raman shifts for nitrogen-doped ZnSe epilayers[62]. All Raman shifts are expressed in cm^{-1}.

In order to test the validity of equation (4.1) an epilayer of intermediate thickness was investigated. The 0.5 μm thick epilayer was grown by MBE in Bremen on a (001) GaAs substrate, overgrown with a GaAs buffer layer. The grower reported a free hole concentration $|N_A-N_D|$ of ~5 x 10^{17} cm^{-3} from N-doping and a free electron concentration ~5 x 10^{16} cm^{-3} from Cl-doping.

The low temperature luminescence from the co-doped ZnSe:N:Cl sample, figure 4.3.1, is dominated by emission in the vicinity of the A^0X. The expanded excitonic region, inset, shows that this dominant feature is in fact composed of two peaks; the A^0X around 2.792 eV and to lower energy a peak designated C. The origin of the C-line is not clear, however, it has been correlated with N-doping and it has been suggested that the centre may involve nitrogen clusters[63]. The arrow indicates the position at which the SFRS was obtained. No SFRS was observed from the C-line indicating that it cannot be attributed to a deep acceptor centre.

The observation of e^--A^0 at 2.7095 eV is consistent with the doping levels reported by the grower[64] and the absence of D^0X luminescence. The N acceptor binding energy determined from the position of the e^--A^0 is 112.3 meV, which agrees well with other reported values, see table 3.1. The two features on the low energy side of e^--A^0 correspond to the shallow donor and deep donor DAP emission, D^sAP and D^dAP respectively; however, it is difficult to resolve the individual bands in the present case. The broadness of the FE, the difficulty in deconvolving the A^0X peak and the absence of the D^0X line make the precise strain state difficult to determine from the PL. However, the epilayer thickness and the position of the FE suggest that the layer is experiencing a small compressive strain.

In figure 4.3.2, distinct anisotropic behaviour of the hole SFRS is observed on varying the angle between the sample normal and the direction of the applied field in the range from 0^0 to 90^0, that is, from [001] to [110]. The fitted data from the SFRS spectra are presented in figure 4.3.3 and the solid line is the result of calculation using equation (4.1). The acceptor-Hamiltonian valence-band parameters determined from the calculation were $\tilde{\kappa}$ = -0.58, $\tilde{q}$ = -0.01 and Δ = -0.37 meV. The value of $\tilde{\kappa}$ obtained is consistent, though, slightly larger than those previously determined[59-61], whilst Δ is entirely consistent with the sign and magnitude anticipated for this specimen. The Faraday field dependence is shown in figure 4.3.4.

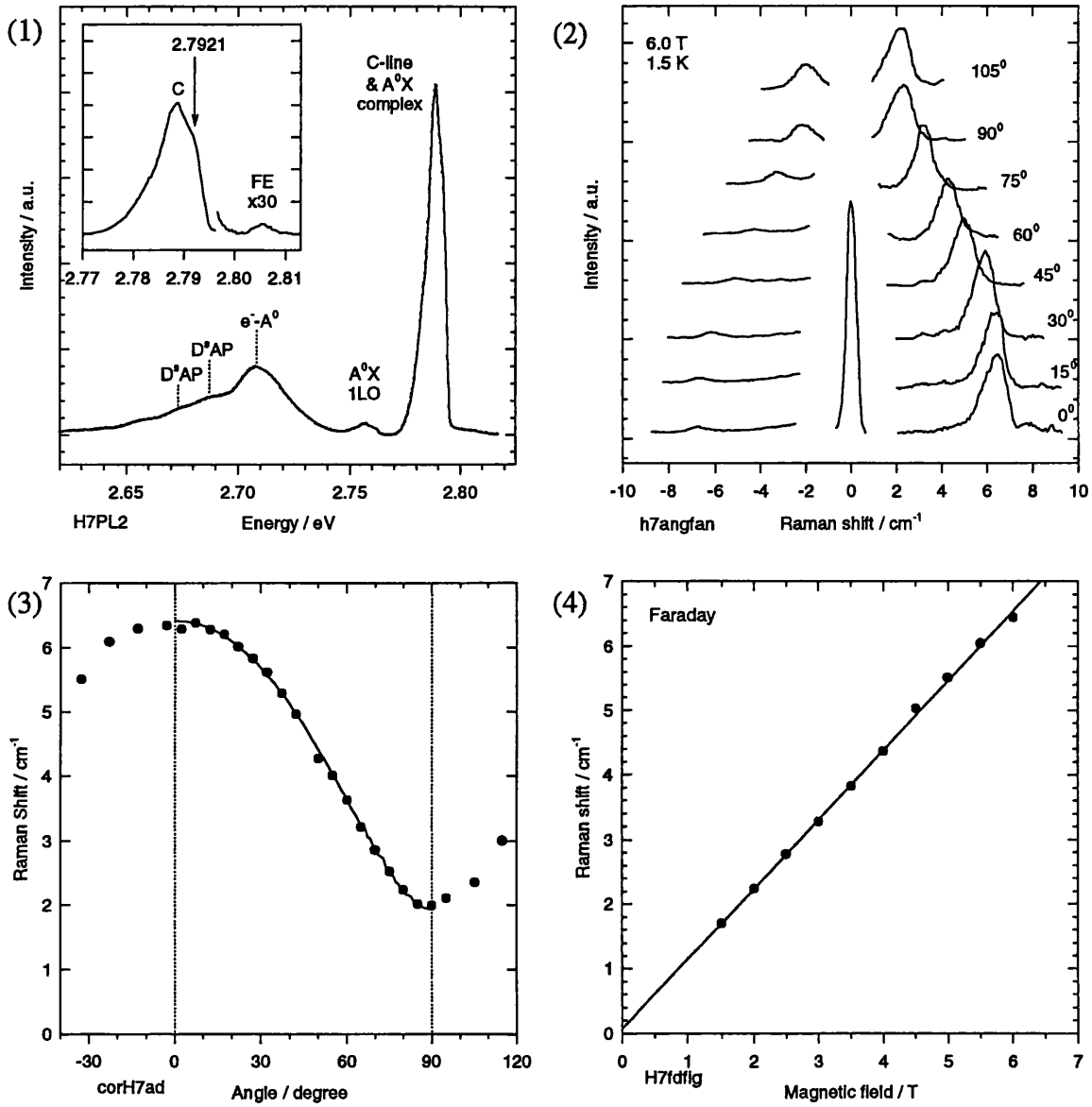

Figure 4.3: (1) Low temperature PL from a co-doped ZnSe:Cl:N epilayer. The inset shows the expanded excitonic region. The arrow indicates the maximum of the hole SFRS signal intensity; (2) SFRS spectra from the acceptor-bound hole as a function of angle between the magnetic field and the growth axis of the sample; (3) Angle dependence of the fitted SFRS data; the solid line was calculated according to equation (4.1); (4) The Faraday magnetic field dependence.

The calculated dependences of the energy levels of the hole states on the rientation of the magnetic field are shown in figure 4.3.5, for the parameters determined above and for a magnetic field of 6.0 Tesla. In figure 4.3.6 the spin-flip Raman shifts corresponding to the energy differences between the valence-band levels are displayed, in the absence of any selection rules. It is clear from figure 4.3.5 that the valence-band states are mixed.

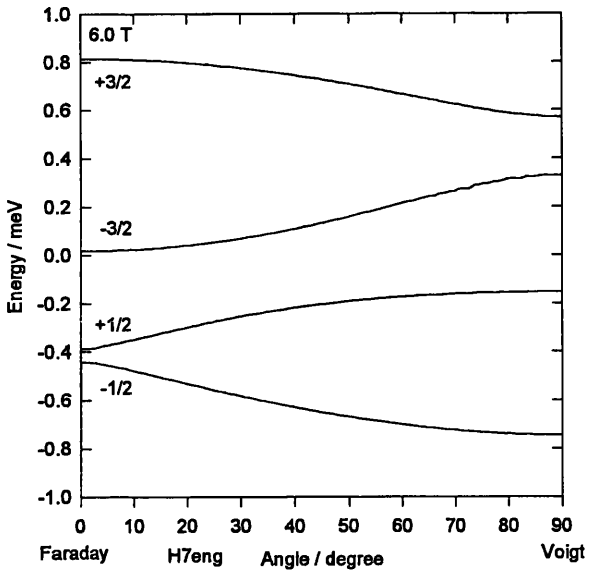

Figure 4.3.5 The calculated dependence of the valence-band energy level states on the angle between the magnetic field and the growth axis, using band parameters determined above.

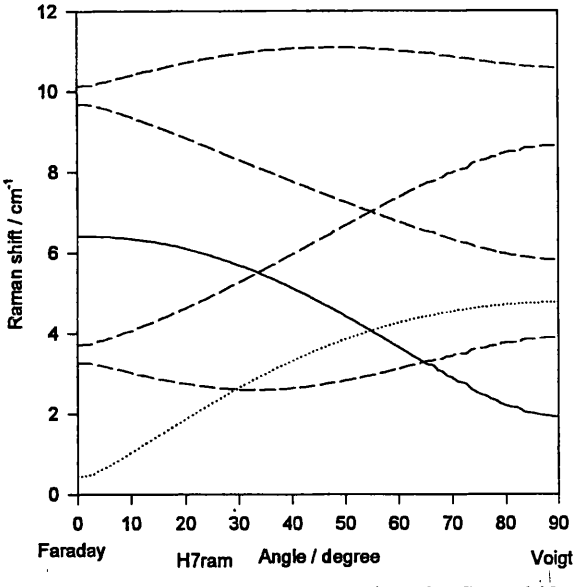

Figure 4.3.6 Lines representing the SFR shifts corresponding to the valence-band energy levels: heavy-hole like (solid), light-hole like (dotted) and mixed states (dashed).

It should be emphasised that the parameters $\tilde{\kappa}$ and $\tilde{q}$ determined here are those of the acceptor-bound hole states. The corresponding valence-band spin-Hamiltonian parameters κ and q can be estimated theoretically in terms of the Luttinger parameters, γ_i, see table 4.4 below. The acceptor-bound valence-band spin-Hamiltonian parameters $\tilde{\kappa}$ and $\tilde{q}$ can in principle be obtained from κ and q[65]. The following relationships enable $\tilde{\kappa}$ to be determined:

$$\tilde{\kappa} = \kappa - d - 13/6\, d(\tau - 1) + 7/6 f \tag{4.2}$$

$$\kappa_L = \gamma_3 - (\gamma_1 - 2\gamma_2 + 2)/3 \tag{4.3}$$

$$d = 0.92\gamma_3^2/\gamma_1, \quad \tau = \gamma_2/\gamma_3, \quad f = 1.5(\varepsilon K)^2 \tag{4.4}$$

where ε is the static dielectric constant and K is the coefficient of the k-linear term in the Hamiltonian. For ZnSe, $K = 2\text{x}10^{-3}$ a.u. has been found by resonant Brillouin scattering[66], implying that f is completely negligible.

Several internally consistent sets of Luttinger parameters have been proposed, that give reliable estimates of the valence-band effective masses, however, they do not yield consistent values of κ and $\tilde{\kappa}$. Using the parameters in table 4.4 and equation (4.2), $\kappa = 0.61 \pm 0.11$ and $\tilde{\kappa} = 0.60 \pm 0.32$ are obtained, where the quoted values represent the average κ and $\tilde{\kappa}$ calculated form the individual parameter sets in table 4.4 and the error quoted is the standard deviation. The magnitude of $\tilde{\kappa}$ calculated here is consistent with the experimentally determined value of $\tilde{\kappa} = -0.58$, however,

the large spread in the theoretical values prohibits further useful comparison. More problematic, however, is that the sign of the measured and predicted κ and $\tilde{\kappa}$ are different. The calculations presented here are most accurate for narrow bandgap materials; it is therefore not expected that a calculation of this type will be appropriate for the valence-band spin-Hamiltonian parameters of ZnSe.

γ_1	γ_2	γ_3	References
4.30	1.14	1.84	[66] [67]
3.21	0.75	2.00	[68]
4.30	1.04	2.00	[69]
3.77	1.24	1.67	[70]

Table 4.4 Luttinger parameters for ZnSe from various sources.

A model has been presented describing the dependence of the valence-band states on the orientation of the magnetic field in the presence of a biaxial strain. The model enables the valence-band spin Hamiltonian parameters, together with the sign and magnitude of the strain to be deduced. The model also predicts manifestly different anisotropic behaviour for the light and heavy hole valence-band states, thus, enabling these states to be distinguished.

The SFRS of acceptor-bound holes in a co-doped ZnSe:N:Cl epilayer with a small indeterminate strain was investigated. The observed anisotropic angular dependence as a function magnetic field direction of the SFRS signals confirmed that the signals obtained were derived from mixed light and heavy hole valence-band states. The epilayer was found to be experiencing a small compressive biaxial strain. The nitrogen-acceptor valence-band spin-Hamiltonian parameters, determined using the model, were found to be consistent with previous measurements. Comparison of the spin-Hamiltonian parameters with theoretical estimates, based on empirically determined Luttinger parameters, were found to be consistent in magnitude, but not in sign.

Hole SFRS has been shown to be an extremely sensitive probe of small strains, not suited to determination by PL. Furthermore, the anisotropic behaviour of holes provides a useful method for distinguishing valence and conduction-band related signals. However, at present it is not possible to relate the acceptor-bound-hole spin Hamiltonian parameters to the valence-band spin Hamiltonian parameters.

4.4 Acceptors in ZnMgSe

In the previous sections the doping issues in ZnSe and the anisotropic behaviour of valence-band related states in the presence of biaxial strain were established; the discussion will now be extended to ZnSe-based alloys. In this section the presence of a small biaxial strain in a nitrogen doped ZnMgSe epilayer will be used to establish the origin of the observed SFRS signals; confirming the assignment for the electron SFRS made in section 3.2 and enabling the strain state of the epilayer to be determined. The section begins with a brief summary of nitrogen doping in ZnSe based alloys.

In ZnMgSSe:N the net active acceptor concentration has been found to monotonically decrease with increasing Mg and S composition[71]. In fact, S and Mg decrease the free hole concentration by as much as a factor of two when added to ZnSe and ZnSSe, respectively[72], see figure 4.4.1. Although the total N concentration increases slightly as S is added to ZnSe, it remains constant with the addition of Mg[73]. This has lead to the suggestion that Mg and S are involved in nitrogen compensation[71,74]. Similar dependences have been reported for N-doping of $Zn_{1-x}Mg_xSe$ (x<0.25)[73] and ZnS_ySe_{1-y} (y<0.3)[75].

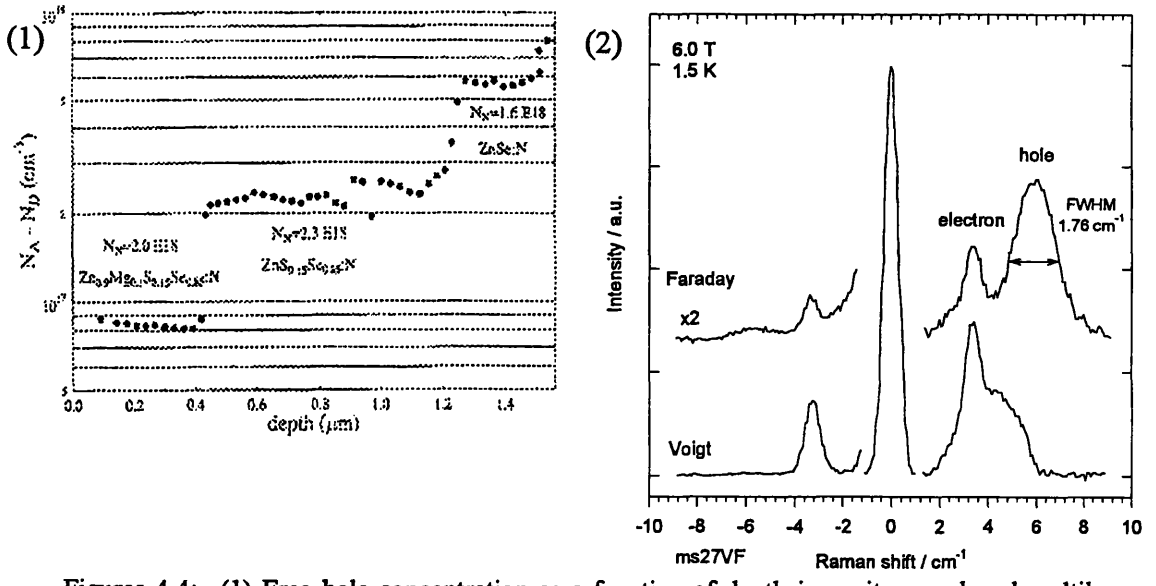

Figures 4.4: (1) Free hole concentration as a function of depth in a nitrogen doped multilayer specimen, determined using electrochemical CV-profiling. Figure taken from reference [72]; (2) SFRS spectra obtained from MBE-grown $Zn_{0.86}Mg_{0.14}Se$ doped with nitrogen. Upper and lower traces show Faraday and Voigt experimental geometries, respectively.

Figure 4.4.2 shows the signals observed in nitrogen doped $Zn_{0.86}Mg_{0.14}Se$ epilayer in two geometries for a magnetic field of 6 Tesla. In each geometry two signals are observed in both the Stokes and anti-Stokes portions of the spectra. The signal with

the higher Raman shift is strongest in Faraday geometry, whilst the signal at lower Raman shift is strongest in Voigt geometry. In Voigt geometry, the selection rules for SFRS imply that electron SFRS should be observed, whereas it is possible to detect hole SFRS in Faraday geometry[54]. Figure 4.4.3 shows that the magnetic field dependence of the signals is linear and converges to the origin in zero field, in accordance with equation (1.38). These observations confirm that the signals arise from SFRS and suggest the identification of the higher and lower Raman shift signals with hole and electron SFRS, respectively.

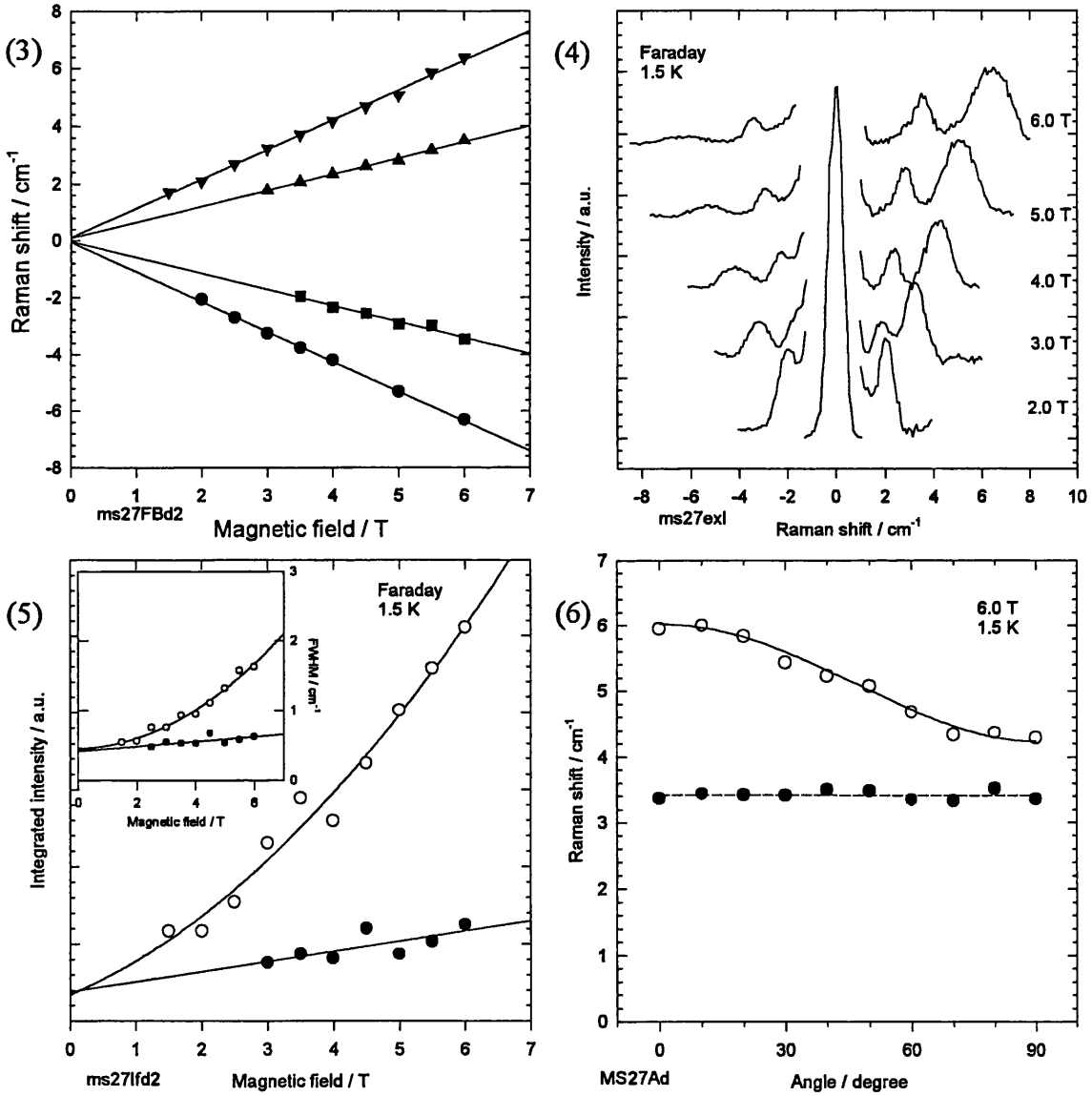

Figures 4.4: (3) The magnetic field dependence data in Faraday geometry; (4) SFRS signals at the magnetic field strengths indicated on the right of the figure; (5) The integrated intensity and FWHM (inset), for signals presented in figure 4.4.4, as a function of magnetic field strength. Electron and hole data represented by filled and open circles, respectively, (6) Dependence of the electron (filled circles) and hole (open circles) spin-flip Raman shift on the angle between the magnetic field and the epilayer growth direction. The solid lines are the result of calculations based on equation (4.1).

Selected spectra from the Faraday field dependence are presented in figure 4.4.4. It is clear from this figure that the linewidth of the signal attributed to the hole decreases as the magnetic field strength is reduced, whilst the intensity remains roughly constant. The magnetic field dependence of the integrated intensities of the signals is shown in figure 4.4.5. The solid lines are quadratic and linear regression fits to the hole and electron data, respectively. The integrated intensity of the electron signal (filled circles) is only weakly dependent on the magnetic field strength, diminishing slightly as the field reduces, but essentially remaining finite even for small fields. This behaviour is consistent with SFRS associated with a carrier bound to a neutral donor, section 3.1. The hole integrated intensity is manifestly field dependent, however, it is important to note that this signal too does not extrapolate to zero integrated intensity at zero field. This behaviour will be reexamined in section 5.1. The observed dependence of the FWHM, inset, is directly analogous to those described in sections 3.1 and 4.2 for donor and acceptor bound electrons and holes.

The spin-flip Raman shift as a function of magnetic field orientation between the growth axis and the layer plane is shown in figure 4.4.6. The solid line in this figure is the result of calculation based on equation (4.1). From the fitting of this line the parameters $\tilde{\kappa} = -0.84$, $\tilde{q} = -0.01$ are determined and a strain splitting of 140 μeV is extracted for the epilayer, thus confirming that the resultant strain in the $Zn_{0.86}Mg_{0.14}Se$ epilayer is indeed small. Similar strains to that determined above were obtained for all the ternary and quaternary ZnSe based material examined in this study.

Nitrogen doping in ZnSe-based alloys has been briefly summarised. The presence of biaxial strain in a nitrogen doped ZnMgSe epilayer has enabled the assignments made previously for electron and hole SFRS signals to be confirmed. The anisotropic behaviour of the signal attributed to the hole identifies it as originating from the valence-band and, therefore, considering the doping and the analogous field dependent behaviour of the FWHM and the integrated intensity to that of the bound states examined previously, it is not unreasonable to conclude that the signal observed in this specimen is derived from the spin-flip of a hole bound to an nitrogen acceptor. It is also clear from figure 4.4.6 that the signal attributed electron in section 3.2 is isotropic, as expected. The measured strain between the epilayer and the GaAs substrate was found to be small.

4.5 Identification of SFRS signals in p-type MOVPE $Ga_{0.52}In_{0.48}P$

The specimen under consideration here forms part of a series of samples grown by MOVPE at Epitaxial Products International Ltd. (EPI) in which the composition was varied according to the formula $(Al_xGa_{1-x})_{0.52}In_{0.48}P$. The growth details and compositional trends within this series will be given in the following section. This section, however, is solely concerned with the identification of the origins of the SFRS signals observed in p-type GaInP.

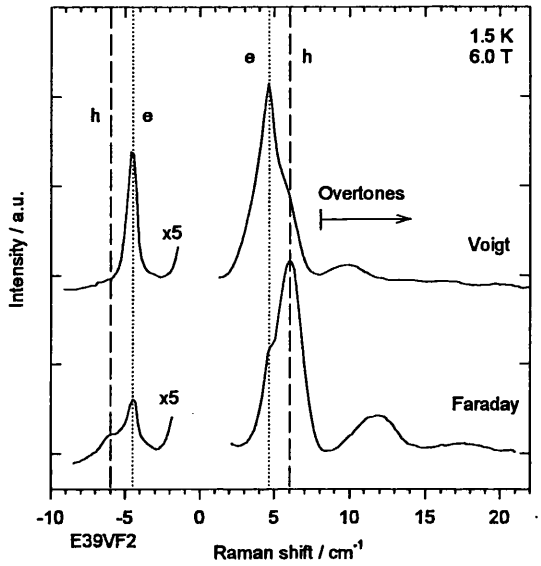

Figure 4.5.1 SFRS spectra from p-type MOVPE-grown $Ga_{0.52}In_{0.48}P$, in Voigt and Faraday geometries. Electron (e) and hole (h) signals are indicated in the figure.

Figure 4.5.1 shows the spectra obtained from the p-type $Ga_{0.52}In_{0.48}P$ MOVPE specimen in Voigt and Faraday geometries at 6.0 T. In total five Stokes signals are observed, although the signals with Raman shifts greater than 7 cm^{-1} are relatively weak. Observation of Stokes and anti-Stokes signals for the two dominant signals, at approximately 4.6 cm^{-1} and 6 cm^{-1}, and the partial adherence of these signals to the electric-dipole selection rules suggest these signals arise from SFRS of electrons and holes, respectively. The signal at ~4.6 cm^{-1} was previously detected in the undoped GaInP material grown by MBE, section 3.3, and was attributed to electron SFRS. The presence of the new signal, at ~6 cm^{-1}, in this deliberately p-doped material gives further indication that the new signal is hole related. However, in contrast to the previous section, there is no apparent shift in the position of the new signal from one field geometry to the other. The figure 4.5.2 shows a series of spectra recorded in Faraday geometry as a function of magnetic field. The magnetic field dependence of the deconvoluted bands is presented in figure 4.5.3. The procedure for deconvolving

the overlapping bands is given in chapter 2. The magnetic field dependence demonstrates that all of the signals behave according to equation (1.38).

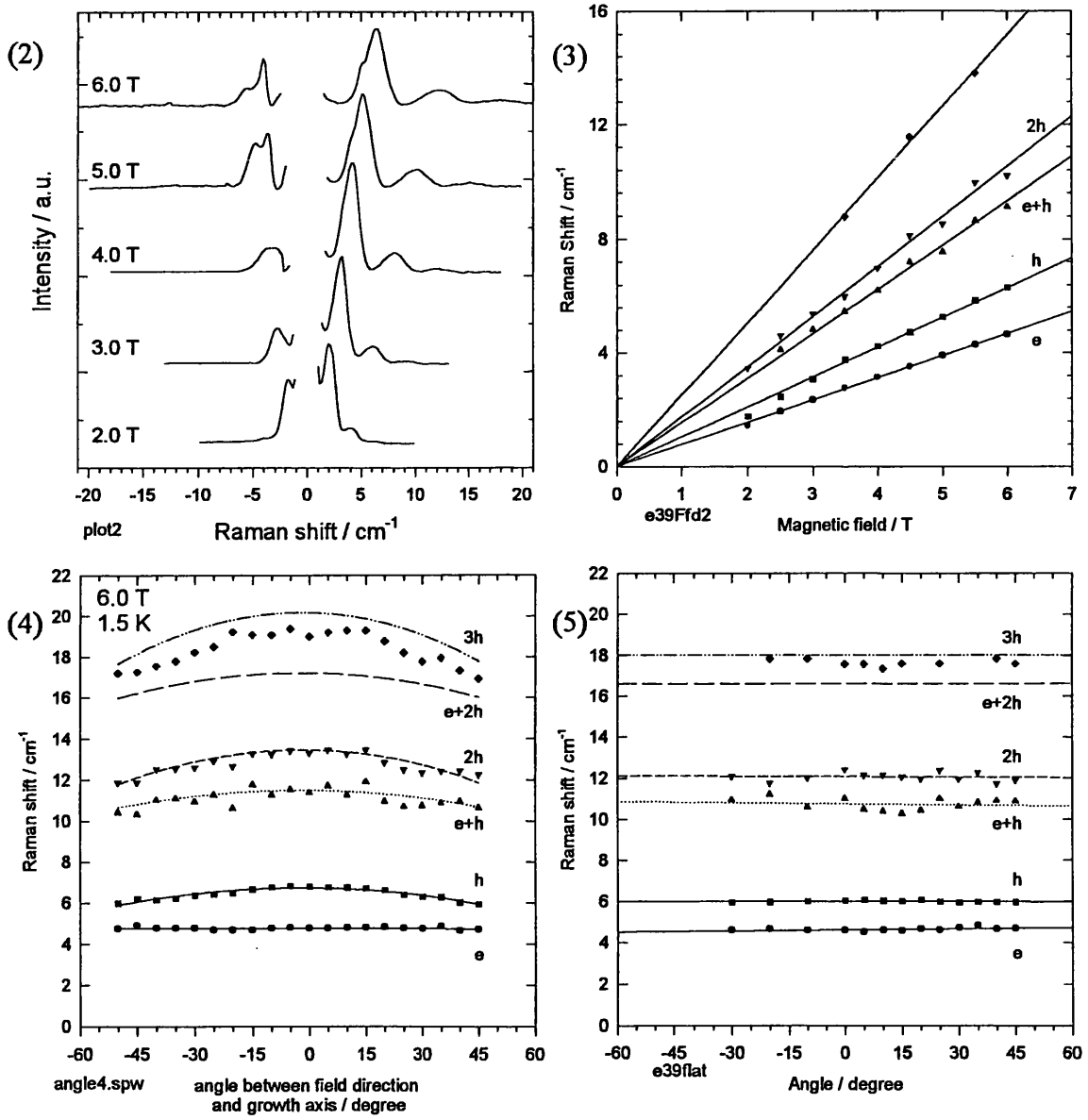

Figures 4.5: (2) SFRS signals at the magnetic field strengths indicated on the left of the figure; (3) The magnetic field dependence data in Faraday geometry; (4) Dependence of SFRS shifts on the angle between the magnetic field and the epilayer growth direction for a epilayer removed from its substrate. Lines are the results of calculation based on equation (4.1), symbols represent electron, hole and combination signals; (5) Dependence of SFRS shifts on the angle between the magnetic field and the epilayer growth direction for an unstrained layer latticed-matched to the substrate.

In order to provide a definitive test of the assignment of the SFRS signals the measurements have been extended to include the variation of strain in the epilayer. The epilayer, nominally latticed-matched to GaAs at the growth temperature, should experience only thermally induced strain produced by the difference in the thermal expansion coefficients between the epilayer and the substrate at low temperatures,

which is expected to be small, certainly less than 1 meV. As demonstrated in previous sections, the SFRS of holes is an extremely sensitive probe of small strains. Therefore, a strain was deliberately introduced into the epilayer by the removal of the substrate, as described in chapter 2. Measurements of the SFRS as a function of the angle between the magnetic field and the normal to the epilayer then reveal a clear anisotropy in the signal ascribed above to hole SFRS. This is shown is figure 4.5.4. The electron signal remains isotropic, as expected, whilst the hole signal is greatest in Faraday geometry and decreases as the magnetic field is rotated towards the layer plane. It is also possible to deconvolve the signals making up the bands at higher Raman shifts, these consist of overtone signals, one with the g-factor $g = g_e+g_h$, one with $g = 2g_h$ and the third signal which appears to be two poorly resolved bands comprised of $3g_h$ and g_e+2g_h. The curved lines in figure 4.5.4 are the results of calculations taking an isotropic electron g-factor and modelling the valence-band splitting in a magnetic field with equation (4.1). The magnitude of the valence-band strain-splitting induced by the substrate removal is found to be 160 μeV. Figure 4.5.5, shows measurements of the Raman shift as a function of angle for the same sample with the epilayer still attached to the substrate. These measurements clearly demonstrate that there is no anisotropy of the hole signal and that, therefore, the strain arising from the differential thermal contraction is indeed negligible in this case.

The deliberate introduction of strain in the epilayer has enabled the unambiguous identification of the electron and hole SFRS signals in p-type GaInP doped with Zn. From magnetic field dependent measurements the following values for the electron and hole gyromagnetic ratios were obtained 1.60 ± 0.05 and 2.05 ± 0.10[76], respectively.

4.6 The dependence of the hole gyromagnetic ratio in AlGaInP

It was confirmed in the previous section that the p-doped material exhibits both electron and hole SFRS. In this last section evidence pertinent to the origin of the SFRS signals will be examined and the compositional dependence of the hole gyromagnetic ratio will be determined for a series of p-type $(Al_xGa_{1-x})_{0.52}In_{0.48}P$ epilayers in the direct gap composition range $0<x<0.46$. The section begins with a brief summary of p-type doping in AlGaInP.

The electrical characteristics of the p-AlGaInP layer as a cladding layer has a direct bearing on the laser performance characteristics, such as the threshold current or maximum operating temperature[77]. For p-type cladding layers a hole concentration of about $1x10^{18}$ cm^{-3} is desired to avoid leakage of the carriers from the active layer towards the cladding layer. This has been achieved using either Zn or Mg as p-type dopants, with Zn being the most widely used dopant because of its excellent controllability and reproducibility. However, in AlGaInP the fraction of Zn that is electrically active decreases with increasing Al content[78]. The maximum obtainable hole concentration for MOVPE grown AlInP doped with Zn is only $2x10^{17}$ cm^{-3}[79]. In devices this results in a high laser threshold current and a pronounced temperature dependence[80]. Using the alternative p-type dopant Mg improved active doping of AlInP has been achieved[81]; however, the current Mg precursors have proved problematic for growers. Studies on MOVPE Zn-doping of AlGaInP using off-axis substrates have shown that substrate misorientation improves the Zn electrical activity and enhances the Zn incorporation efficiency[82]. Oxygen contamination has been identified as the main cause of Zn acceptor compensation[82], since oxygen in the layers can act as a deep donor, thereby reducing the Zn electrical activity. In addition the introduction of p-type dopants influences the surface morphology of GaInP[83]. This can destabilize thermodynamically the surface reconstruction[84]. It has been found that the presence of Mg and Zn atoms above a critical concentration ($\sim10^{18}$ cm^{-3})[85-89] has the effect of 'poisoning' the CuPt-type order. Recent studies involving the n-type dopant Te have shown that CuPt-type ordering is eliminated for Te concentrations greater than $6x10^{17}$ cm^{-3}[90]. The MOVPE growth process is believed to increase the propensity of AlGaInP to order[91].

The material under investigation was grown by MOVPE and a free hole concentration of 1-2 x 10^{17} cm^{-3} was achieved using Zn as a p-type dopant, suggesting possible

oxygen compensation. The epilayers were 0.5 μm thick and lattice matched to GaAs substrates; a GaAs buffer layer and capping layer were also included.

Figure 4.6.1 shows the low temperature PL from the p-type GaInP sample grown by MOVPE. An order parameter of $\eta = 0.25$ is indicated by the energetic position of the PL band, at 1.973 eV. The FWHM of 9.7 meV is significantly broader than that reported for the nearly disordered GaInP MBE specimen in section 3.3; alloy fluctuations, domain size variation and the presence of Zn acceptor impurities may all contribute to the broadening; however, it is not clear which mechanism is most significant. The increased prominence of the lower energy feature is consistent with the stronger LO phonon coupling strength associated with an acceptor bound recombination[92]. Figure 4.6.2 shows that the variation of the integrated intensity and FWHM with magnetic field for the electron (filled circle) and hole (open circle) SFRS is analogous to the those described in sections 3.1 and 4.2 for donor and acceptor bound electrons and holes in the ZnSe-based alloys.

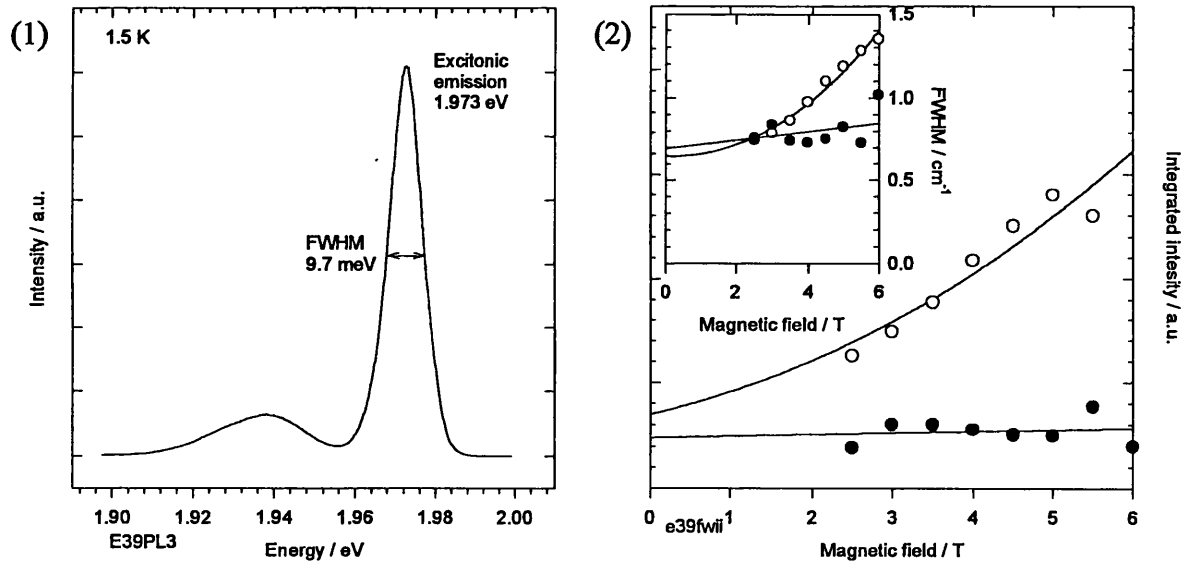

Figures 4.6: (1) Low temperature photoluminescence spectrum from a p-type $Ga_{0.52}In_{0.48}P$ layer grown by MOVPE; (2) The integrated intensity and FWHM (inset) as a function of magnetic field strength for the p-type MOVPE grown $Ga_{0.52}In_{0.48}P$ epilayer. The electrons and holes are represented by filled and open symbols, respectively.

To investigate further the origin of the SFRS signals the intensity of the signals as a function of excitation energy was examined. It is clear in figure 4.6.3 that both SFRS signals exhibit a strong resonant enhancement at approximately the same energy (to within 0.8 meV) which falls on the high energy side of the dominant PL peak, at 2.103 eV. The width of the resonance profile of the SFRS signals is significantly less than that of the PL peak, suggesting that the latter does not arise from a single

process. The origin of the excitonic emission, its broadening mechanism and the origin of the SFRS will be re-examined in section 5.2.

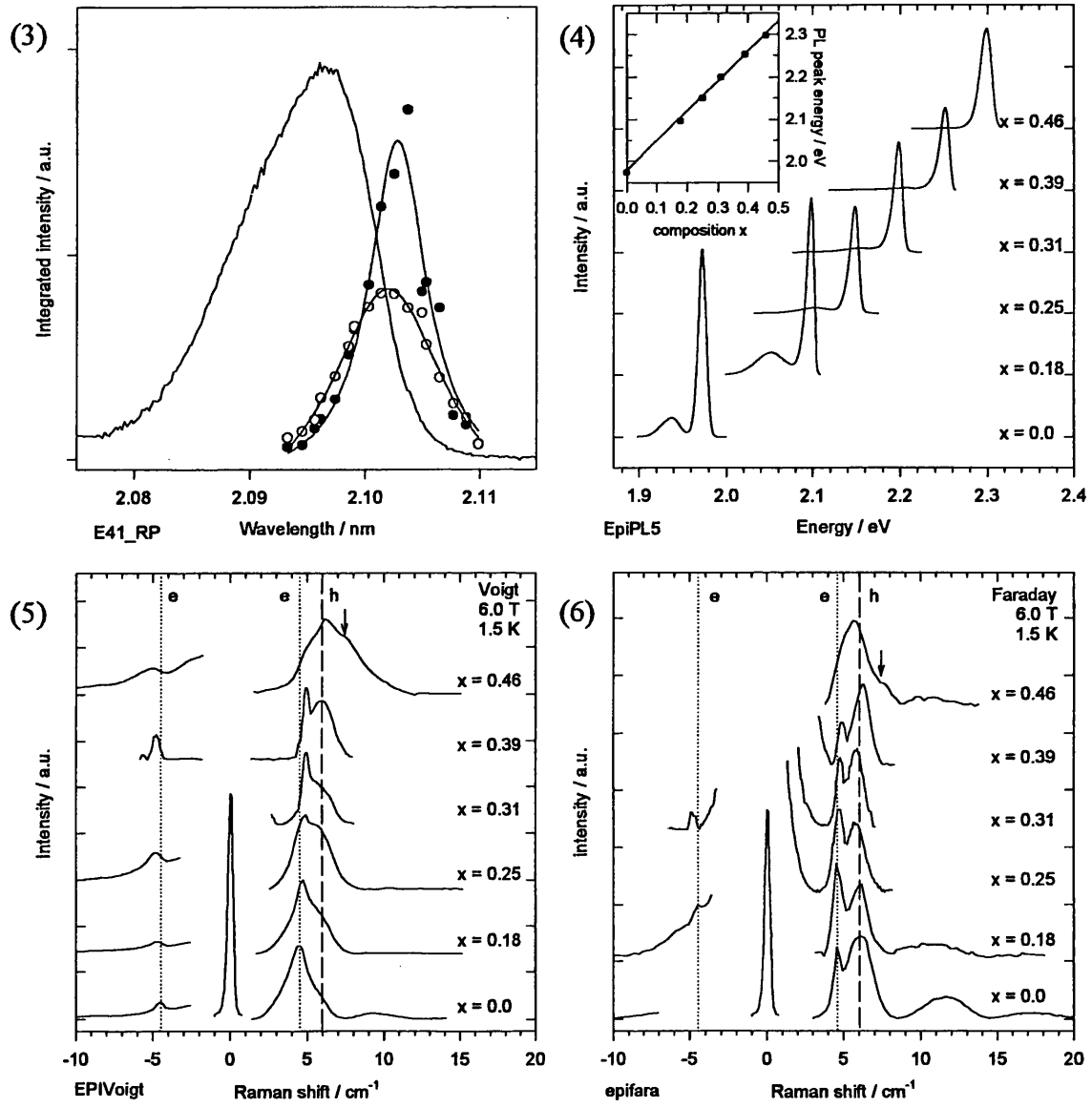

Figures 4.6: (3) Electron (filled circles) and hole (open circles) SRFS resonance profile data superimposed on the PL spectrum from a p-doped MOVPE-grown $(Al_{0.18}Ga_{0.82})_{0.52}In_{0.48}P$ epilayer. SFRS data fitted according to equation (1.39); (4) PL spectra from p-type MOVPE-grown $(Al_xGa_{1-x})_{0.52}In_{0.48}P$ epitaxial material. The inset shows the compositional dependence of the dominant PL peak position, with the expected variation (solid line) according to reference [93]; (5) Voigt SFRS spectra for the compositions indicated on the right of the figure; (6) Faraday SFRS spectra for the compositions indicated on the right of the figure.

Figure 4.6.4 shows the low temperature PL for the series of samples described in section 4.5. As previously mentioned, the dominant band in the PL of this p-doped material corresponds to bound exciton emission; this point will be justified in chapter 5. The relative intensity of the feature on the low energy side of the main peak was found to diminish with increasing Al content. The inset of figure 4.6.4 shows the comparison between the expected variation of the excitonic bandgap at low

temperatures and the energy of the dominant band observed in the PL. The variation of the excitonic bandgap, E_0, was determined in a previous investigation[93], at 4.2 K, to be:

$$E_0(x) = 1.9790 + 0.704x \tag{4.5}$$

The dependence of the PL and PLE spectra on composition[93] showed a small Stokes shift of the dominant PL band, which increased as the Al content increased, but was always less than 10 meV for the direct gap compositions studied here.

Figures 4.6.5 and 4.6.6 show the SFRS spectra obtained for the composition range examined, in Voigt and Faraday geometries respectively. Despite the electron SFRS signal being dominant in Voigt geometry and the hole SFRS signal being dominant in Faraday geometry, precise deconvolution of the two signals was problematic. It is also clear from the two figures that the variation in g-value with composition is small for both electron and hole signals. It is interesting to note the emergence of a third signal, indicated by an arrow, at higher Raman shift than the hole for the sample with the highest Al content, x=0.46. This third signal forms a weak shoulder in Faraday geometry and is more prominent in Voigt geometry, but is not evident in the spectra of samples with lower Al content. The significance of this signal will be discussed in chapter 5.

Figure 4.6.7 shows a composite diagram with electron g-values determined using the magnetic field dependence of the SFRS signals in Voigt geometry and hole g-values determined using Faraday geometry data. The electron data was fitted in precisely the same manner as the undoped MBE material, section 3.4, using equation (4.5) for the compositional dependence of the bandgap. The dependence of the electron gyromagnetic ratio (dashed line) is reproduced well for the p-doped MOVPE material; in fact there is negligible difference between the results for the doped and undoped material.

The information available to calculate the compositional dependence of the hole gyromagnetic ratio for ternary and quaternary phosphide-based material is extremely limited. To implement the approach based on the Luttinger parameters adopted in section 4.3 for the phosphides requires the following linear interpolations of the binary Luttinger parameters[94]:

$$\gamma_1 = 5.24 - 0.365x, \quad \gamma_2 = 1.53 - 0.46x, \quad \gamma_3 = 2.21 - 0.255x \tag{4.6}$$

The result of the above calculation, illustrated in figure 4.6.7 by the dotted line, underestimates the experimental data g-values. However, an alternative three-band model expression for κ exists[95]:

$$\kappa = \frac{1}{3}\left(1 - \frac{E_p}{2E_0}\right) \tag{4.7}$$

dependent on, in this case, the interpolated binary energy momentum matrix element E_p, equation (3.3), and the variation of the excitonic bandgap, E_0, equation (4.5). The gyromagnetic ratios determined using equation (4.7) are also shown in figure 4.6.7 by the solid line.

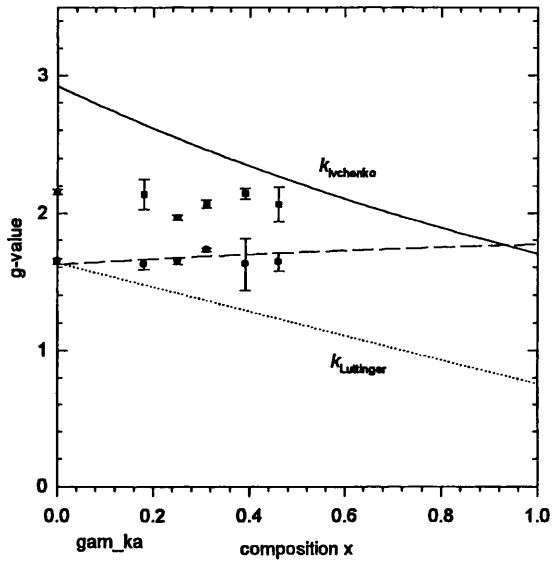

Figure 4.6.7 The compositional dependence of the electron (circles) and hole (squares) g-factor in p-type MOVPE-grown $(Al_xGa_{1-x})_{0.52}In_{0.48}P$ epitaxial material. Vertical bars indicate the uncertainty in measurement. The dashed line indicates the three-band $k \cdot p$ theory calculation for the electron g-value. The solid and dotted lines are calculations for the hole g-factors based on references [95] and [65], respectively.

The average value of g_h obtained from the experimental data is 2.05 ± 0.1[76] and this is related to the bandstructure parameter κ via $g_h = 2\kappa$. No determination of this parameter exists for the alloy and its interpretation is rather difficult since the hole observed is bound to the Zn acceptor, rather than free, so g_h need not be equal to the value appropriate to the valence-band[38]. It is interesting to note that a value of $g_h = 1.81$ is obtained by linear interpolation of the values κ reported for InP and GaP[94]. However, linear interpolation does not correctly predict the hole g-factor when x is greater than zero for the present series of samples, since a strong dependence on composition would be expected, whereas it is found experimentally that g_h does not vary significantly with composition.

Experimental results have been presented for the compositional dependence of the electron and hole SFRS signals in MOVPE-grown AlGaInP alloy. The electron g-value is found to have the same compositional dependence as that reported earlier in section 3.4 for MBE grown material. The compositional dependence of the hole g-value is reported for the first time and is found to exhibit only a small variation over the composition range examined. However, the overall fit obtained, using appropriate three-band $\boldsymbol{k \cdot p}$ theory, to the hole SFRS data is less satisfactory than that achieved for the electron SFRS data. The observed magnetic field dependence of these signals in conjunction with information provided by the grower concerning the doping levels of the epilayers indicate that the results are consistent with the signals originating from bound exciton complexes.

4.7 References

[1] A. Ohki, N. Shibata, K. Ando and A. Katsui, J. Cryst. Growth **93** (1988) 93

[2] R. M. Park, M. B. Troffer, C. M. Rouleau, J. M. DePuydt and M. A. Hasse, Appl. Phys. Lett. **57** (1990) 2127

[3] K. Ohkawa, K. Karasawa and T. Mitsuyu, Jpn. J. Appl. Phys. **330** (1991) L152

[4] Sz. Fujita, T. Ansano, K. Maehara and Sg. Fujita, 35th Electronic Materials Conf. Santa Barbara, USA, June 1993

[5] W. Stutius, J. Cryst. Growth **59** (1982) 1

[6] T. Yao and Y. Okada, Jpn. J. Appl. Phys. **25** (1986) 821

[7] M. Okajima, M. Kawachi, T. Sato, K. Hirahara and T. Beppu, Extended Abstracts 18th Conf. on Solid State Devices and Materials, Tokyo, 647 (1986)

[8] S. M. Shibi, M. C. Tamargo, B. J. Skromme, S. A. Schwartz, R. E. Nahory and R. J. Martin, J. Vac. Sci. Technol B **8** (1990) 187

[9] H. Mitsuhasi, A. Yahata, T. Uemoto, A. Kamata, M. Okajima, K. Hirahara and T. Beppu, J. Cryst. Growth **101** (1990) 818

[10] H. Cheng, J. M. DePuydt, J. E. Potts, and T. L. Smith, Appl. Phys. Lett. **52** (1988) 147

[11] J. Ren, K. A. Bowers, A. Sneed, D. L. Dreifus, Jr. J. W. Cook, J. F. Schentzina, R. M. Kolbas, Appl. Phys. Lett. **57** (1990) 1901

[12] H. Kukimoto, J. Cryst. Growth **101** (1990) 953

[13] B. J. Skromme Annu. Rev. Mater. Sci. **25** (1995) 601

[14] K. Nakano, P. J. Boyce, J. J. Davies and D. Wolverson, J. Cryst. Growth **117** (1992) 331

[15] J.H.Harding, J.Phys.C**14** (1981) 5049

[16] J. Lilja, M. Toivonen, P. Wyosocki and M. Pessa, Vacuum **40** (1990) 491

[17] D. B. Laks, C. C. G. Van de Walle, G. F. Neumark and S. T. Pantellides, Proc. 20th Int. on Physics of Semiconductors 1991

[18] H. Kukimoto, Mat. Sci. Forum **143** (1994) 385

[19] J. Qiu, J.M. DePuydt, H. Cheng and M.A. Hasse, Appl. Phys. Lett. 59 (1991) 2992

[20] K. W. Kwak, R. D. King-Smith and D. Vanderbilt, Phys. Rev. B **48** (1993) 17827

[21] A. Garcia and J. E. Northrup, Phys. Rev. B **74** (1994) 1131

[22] B. H. Cheong, C. H. Park and K. J. Chang, Phys. Rev. B **51** (1995) 10610

[23] C. H. Park and D. J. Chadi, Phys. Rev. Lett.**75** (1995) 1134

[24] C. M. Townsley, J. J. Davies, D. Wolverson, and P. J. Boyce, G. Horsburgh, T. A. Steele, K. A. Prior, and B. C. Cavenett, Phys. Rev. B **53** (1996) 10983

[25] D. Wolverson, P. J. Boyce, C. M. Townsley, B. Schlichtherle and J. J. Davies, J. Cryst. Growth **159** (1995) 229

[26] I. S. Hauksson, J. Simpson, S. Y. Wang, K. A. Prior and B. C. Cavenett, Appl. Phys. Lett. **61** (1992) 2208

[27] I. S. Hauksson, S. Y. Wang, J. Simpson, K. A. Prior, B. C. Cavenett, W. Liu and B. J. Skromme, Phys. Rev. B **52** (1995) 17184

[28] T. Yao, Z. Zhu, Y. H. Wu, C. D. Song, F. Nishiyama, K. Kimura, H. Kajiyama, S. Miwa and T. Yasuda, J. Cryst. Growth **159** (1996) 214

[29] E. Tournie, C. Morhain, G. Neu, J.-P. Faurie, Phys. Rev. B **56** (1997) R1657

[30] private communication K. Ohkawa

[31] G. Kudlek, N. Presser, J. Gutowski, S. Durbin, D. Menke, M. Kobayashi and R. L. Gunshor, J. Cryst. Growth **101** (1990) 667

[32] K. Ohkawa, T. Mitsuyu and O. Yamazaki, Phys. Rev. B **38** (1988) 12465

[33] J. Gutowski, N. Presser and G. Kudlek, Phys. Stat. Sol. (a) **120** (1990) 11

[34] K. Shahzad, J. Petruzzello, D.J. Olego, D.A Cammack and J.M. Gaines, Appl. Phys. Lett. 57 (1990) 2452

[35] L. Worschech, W. Ossau, C. Fischer, H. Schafer and G. Landwehr, Mat. Sci. Eng. **B43** (1997) 29

[36] K. Shahzad, Phys. Rev. B **38** (1988) 8309

[37] R. N. Bhargava, Bull. Am. Phys. Soc. **32** (1987) 610

[38] T. Yao and Y. Okada, Jpn. J. Appl. Phys. **25** (1986) 821

[39] E. Tournie, C. Morhain, G. Neu, J.-P. Faurie, J. Cryst. Growth **184/185** (1998) 520

[40] D. Albert, J. Kraus, S. Einfeldt, J. Nürnberger and D. Hommel, Sol. Stat. Comms.**97** (1996) 909

[41] J.R. Haynes, Phys. Rev. Lett. **4** (1960) 361

[42] E. Kurtz, J. Nürnberger, B. Jobst, H. Baumann, M. Kuttler, S. Einfeldt, D. Hommel and G. Landwehr, K. Bethge, and D. Bimberg, J. Cryst. Growth **159** (1996) 289

[43] Y. Zhang, B. J. Skromme and H. Cheng, Phys. Rev. B **47** (1993) 2107

[44] E.V. Markov and A.A. Davydov, Neorg. Mater. 11 (1975) 1755

[45] P. J. Dean, D. C. Herbert, C. J. Werkhoven, B. J. Fitzpatrick and R. N. Bhargava, Phys. Rev. B **23** (1981) 4888

[46] M. Isshiki, T. Kyotani, K. Masumoto, W. Uchida and S. Suto, Phys. Rev. B **36** (1987) 2568

[47] U. W. Pohl, D. Wiesmann, G. H. Kudlek, B. Litzenburger and A. Hoffmann, J. Cryst. Growth **159** (1996) 414

[48] H. Mathieu, J. Camassel and F. Ben Chenkroun, Phys. Rev. B **29** (1984) 3438

[49] Y. Oka and M. Cardona, Phys. Rev. B **23** (1981) 4129

[50] R. N. Bhargava, J. Cryst. Growth **59** (1982)15

[51] P. J. Dean, H. Venghaus and P. E. Simmonds, Phys. Rev. B **18** (1978) 6813

[52] P. J. Dean and J. L. Merz, Phys. Rev. **178** (1969) 1310

[53] A. Baldereschi and N.O. Lipari, Phys. Rev. B **8** (1973) 2697

[54] Y. Yafet, Phys. Rev. **152** (1966) 858

[55] A. Hoffmann, D. Wiesmann, I. Loa, R. Heitz, W. W. Pohl, I. Broser, L. Worschech, E. Kurtz, D. Hommel, G. Landwehr and B. K. Meyer, J. Cryst. Growth **159** (1996) 302

[56] G. L. Bir and G. E. Pikus, '*Symmetry and Strain Induced Effects in Semiconductors*' (J. Wiley and Sons, New York, 1974)

[57] K. Ohkawa, T. Mitsuyu and O. Yamazaki, Phys. Rev. B **38** (1988) 12465

[58] J. Gutowski, N. Presser and G. Kudlek , Phys. Stat. Sol. (a) **120** (1990) 11

[59] W. Heimbrodt, C. L. Orange, D. Wolverson, J. J. Davies, K. Kimura and T. Yao, Phys. Rev. B **56** (1997) 6889

[60] C. Orange, B. Schlichtherle, D. Wolverson, J. J. Davies, T. Ruf, K. Ogata and Sg. Fujita, Phys. Rev. B **55** (1997) 1607

[61] C. L. Orange, W. Heimbrodt, D. Wolverson and J. J. Davies, J. Cryst. Growth **184/185** (1998) 510

[62] Catherine Orange, PhD thesis, University of East Anglia, Norwich 1998

[63] E. Kurtz, J. Nürnberger, B. Jobst, H. Baumann, M. Kuttler, S. Einfeldt, D. Hommel and G. Landwehr, K. Bethge, and D. Bimberg, J. Cryst. Growth **159** (1996) 289

[64] Private communication D. Hommel

[65] K. Cho, S. Suga, W. Dreybrodt and F. Willmann, Phys. Rev. B **11** (1975) 1512

[66] B. Sermage and G. Fishman, Phys. Rev. B **23** (1981) 5107

[67] H. Mayer and U. Rössler, Sol. Stat. Comms. **87** (1993) 81

[68] M. Willatzen, M. Cardona and N. E. Christensen, Phys. Rev. B **51** (1995) 17992

[69] H. Mayer, U. Rössler, K. Wolf, A. Elstner, H. Stanzl, T. Reisinger and W. Gebhardt, Phys. Rev. B **52** (1995) 4956

[70] P.Y. Yu and M. Cardona, '*Fundamentals of Semiconductors*' (Springer-Verlag, Berlin, 1996)

[71] H. Okuyama, Y. Kishita, T. Miyajima, A. Ishibashi and K. Akimoto, Appl. Phys. Lett. **64** (1994) 904

[72] B. Jobst, S. Strauf, P. Baume, E. Kurtz, H. Schenk, D. Hommel and G. Landwehr, Int. Sym. Blue Laser and light Emitting Diodes, Chiba Univ., Japan, March 5-7, 1996 We-P01

[73] B. Vogele, C. Morhain, B. Urbaszek, S. A. Telfer, K. A. Prior, and B. C. Cavenett, J. Cryst. Growth **201/202** (1999) 950

[74] J. Han, M. D. Ringle, Y. Fan, R. L. Gunshor, A. V. Nurmikko, Appl. Phys. Lett. **65** (1994) 3230

[75] N. Teraguchi, S. Hirata, H. Mouri, Y. Tomomura, A. Suzuki and H. Takiguchi, J. Cryst. Growth **150** (1995) 803

[76] I.J. Griffin, D. Wolverson, J.J. Davies, M. Emam-Ismail, J. Heffernan, A.H. Kean S.W. Bland and G. Duggan, Semicond. Sci. Technol. **15** (2000) to be published

[77] G. Hatakoshi, K. Itaya, M. Okajima and Y. Uematsu, IEEE J. Quantum Electron.QE-**27** (1991) 1476

[78] Y. Nishikawa, M. Suzuki, M . Ishikawa, Y. Kokubun and G. Hatakoshi, J. Cryst. Growth **123** (1992) 181

[79] M. Suzuki, K. Itaya and M. Okajima, Jpn. J. Appl. Phys. **33** (1994) 749

[80] S.H. Hagen, A. Valster, M.J.B. Boermans and J. van der Heyden, Appl. Phys. Lett. **57** (1990) 2291

[81] Y. Nishikawa, H. Sugarawa and Y. Kokubun, J. Cryst. Growth **119** (1992) 292

[82] G.J. Bauhuis, P.R. Hageman and P.K. Larsen, J. Cryst. Growth **191** (1998) 313

[83] I. Pietzonka, T. Sass, R. Franzheld, G. Wagner and V. Gottschalch, J. Cryst. Growth **195** (1998) 21

[84] A. Zunger and S. Mahajan, *'Atomic Ordering and Phase Separation in Epitaxial III-V Alloys in Handbook on Semiconductors'*, Eds. T. Moss and S. Mahajan, vol. 3, ch. 19, (Elsevier Science, Amsterdam, 1994)

[85] A. Gomyo, T. Suzuki and S. Iijima, Phys. Rev. Lett. **60** (1988) 2645

[86] A. Gomyo, S. Kawata, T. Suzuki, S. Iijima and I. Hino, Jpn. J. Appl. Phys. **28** (1989) L1728

[87] T. Suzuki, A. Gomyo and S. Iijima, J. Cryst. Growth **93** (1988) 396

[88] T. Suzuki, A. Gomyo, S. Iijima, K.Kobayashi, S. Kawata, I. Hino and T. Yusa, Jpn. J. Appl. Phys. **27** (1988) 2098

[89] T. Suzuki, A. Gomyo, I. Hino, K.Kobayashi, S. Kawata and S. Iijima, Jpn. J. Appl. Phys. **27** (1988) L1549

[90] S.H. Lee, C.Y. Fetzer, G.B. Stringfellow, D.H. Lee and T.Y. Seong, J. Appl. Phys. **85** (1999) 3590

[91] F. Scholz, C. Geng. M. Burkard, H.-P. Gauffel, H. Schweizer, R. Wirth, A. Moritz and A. Hangleteiter, Physica E **2** (1998) 8

[92] K.J. Nash and M.S. Skolnick, Phys. Rev. B **39** (1989) 5558

[93] D.J. Mowbray, O.P. Kowalski, M Hopkinson, M.S. Skolnick and J.P.R. David, Appl. Phys. Lett. **65** (1994) 213

[94] Landolt-Börnstein *'Numerical Data and Functional Relationships in Science and Technology'*, (Springer) 1982

[95] E.L. Ivchenko and G.E. Pikus, *'Superlattices and Other Heterostructures'*, (Springer-Verlag New York) 1994

Chapter 5 - Excitons

The exciton is of central importance in our understanding of semiconductors. In the following chapter the behaviour of weakly localised excitons will be investigated, thereby accounting for the additional signals reported in chapters 3 and 4. The chapter is divided into two sections. The first section establishes the existence of localised excitons in the quaternary alloy ZnMgSSe, whilst in the second section analogous results are reported for the AlGaInP quaternary material system. Thus, weak exciton localisation is establish as a general phenomena of quaternary alloys, independent of the particular material system.

Section 5.1 Exciton localisation in ZnMgSSe

The quaternary alloy ZnMgSSe is a promising material in which to study the effects of alloy disorder, since composition variations on both anion and cation sublattices are likely to induce strong potential fluctuations. In this section a preparatory investigation of the magnetic field dependent signals observed in ZnMgSSe quaternary alloy is undertaken. Two types of sample are examined, a nitrogen doped epilayer specimen and the undoped quaternary barriers of a SQW sample.

The magnetic field dependent signals obtained from the nitrogen doped $Zn_{0.9}Mg_{0.1}S_{0.22}Se_{0.78}$ quaternary alloy are presented in figure 5.1.1, in Voigt and Faraday geometries at 6 Tesla. Superficially, these spectra resemble those presented for the nitrogen doped ZnMgSe ternary alloy in section 4.4, however, it will be shown that important differences occur in the magnetic field dependence of the broader signal.

Consider first the signal at lower Raman shift. This signal adheres to the selection rules for electron SFRS, as described in section 4.4. The Raman shift, at 3.75 cm^{-1} at 6 Tesla, is consistent with the five-band third-order $\boldsymbol{k \cdot p}$ prediction for the electron SFRS, section 3.2, for the above composition. The linewidth is narrow, comparable to those previously reported for electron SFRS in section 3.1, and exhibits only a weak dependence on the magnetic field, inset figure 5.1.2 (filled circles). The magnetic field dependent behaviour of the integrated intensity (filled circles), figure 5.1.2, is in accordance with that reported in sections 3.1 and 4.2. The field dependence of the Raman shift, figure 5.1.3, is linear and converges to the origin at zero field, in accordance with equation (1.38). Finally, from figure 5.1.3 it can be deduced that the signal is isotropic in the presence of biaxial strain (open symbols:

Voigt geometry and filled circles: Faraday geometry). Therefore, the signal can be attributed to SFRS of an electron bound to a neutral donor. The data for figures 5.1.2 and 5.1.3 were obtained from the spectra presented in figure 5.1.4.

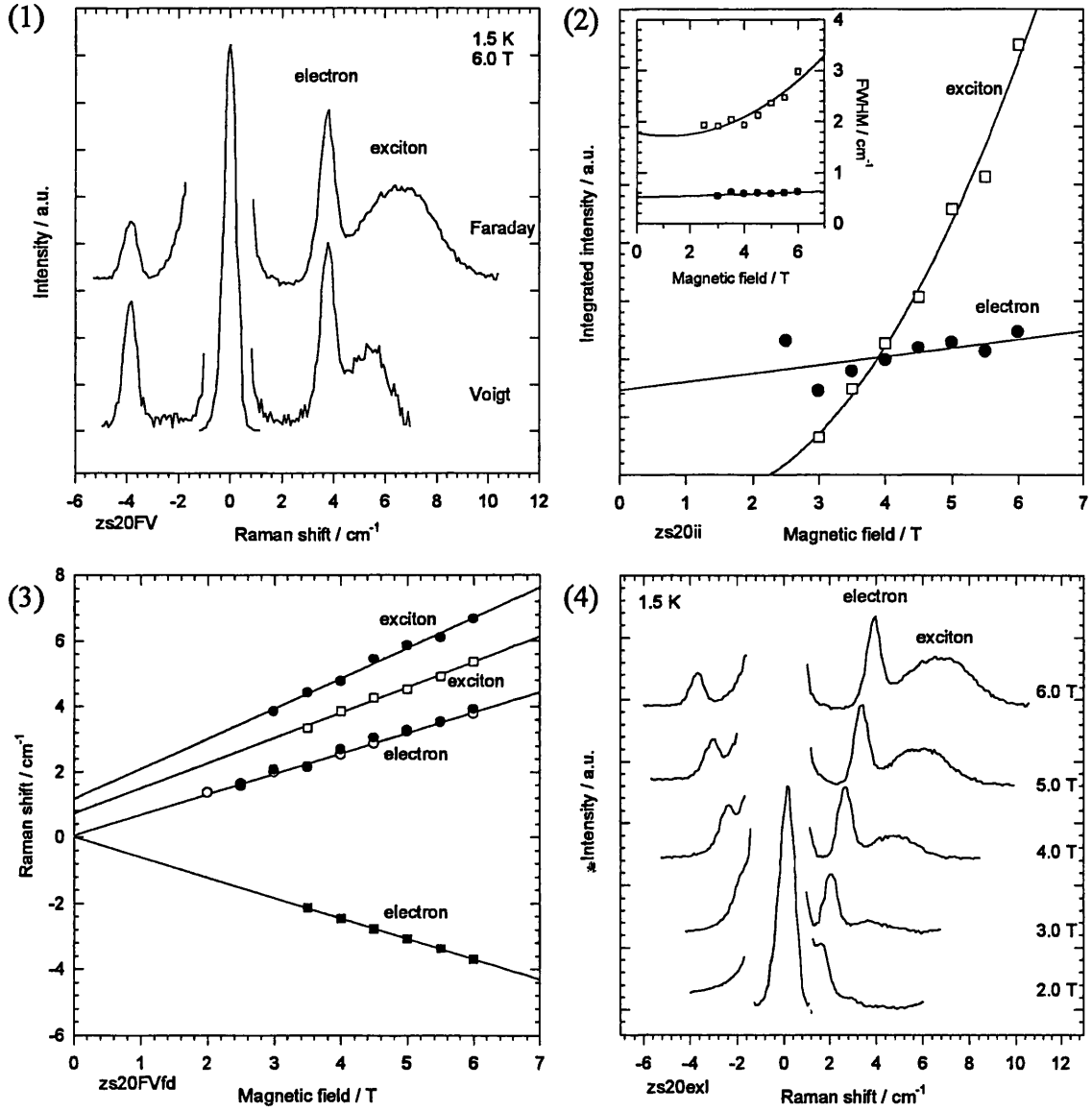

Figures 5.1: (1) Voigt and Faraday SFRS spectra from a nitrogen-doped $Zn_{0.9}Mg_{0.1}S_{0.22}Se_{0.78}$ quaternary epilayer; (2) Faraday magnetic field dependence of integrated intensity and FWHM (inset) for N-doped epilayer. Filled and open symbols corresponding to electron and exciton, respectively; (3) Voigt (open) and Faraday (filled) magnetic field dependence of electron (circle) and exciton (square) SFRS Raman shift for N-doped epilayer; (4) Faraday SFRS spectra from a N-doped epilayer for the range of magnetic field strengths indicated on the right side of the diagram.

The signal at higher Raman shift shares several similarities with the hole SFRS. It partially adheres to the selection rules appropriate for hole SFRS. Anisotropic behaviour can be inferred from figure 5.1.3. The FWHM exhibits a similar magnetic field dependence to those reported for holes in sections 4.2 and 4.4, although the new signal is significantly broader. However, a distinct departure from the previous

behaviour reported for holes is observed in the magnetic field dependence, in which important differences occur in the integrated intensity and the Raman shift. The integrated intensity exhibits a pronounced quadratic dependence on magnetic field, extrapolating to zero between 1 and 2 Tesla. This requirement of a minimum threshold field suggests a 'switching on' of the transition. This is clearly seen in figure 5.1.2. The Raman shift of the signal as a function of magnetic field, though linear, does not extrapolate to the origin for zero magnetic field. This finite value implies a zero field splitting of a few tenths of an meV. No signal reported previously in this work exhibits this range of field dependent behaviour.

Analogous behaviour of the linewidth, integrated intensity and nonzero Raman shift at zero field was also exhibited by the undoped quaternary barriers of the SQW samples. Results for sample S84 are shown in figure 5.1.5 and 5.1.6. The Voigt and Faraday magnetic field dependences and the angular variation are shown in figure 5.1.7.

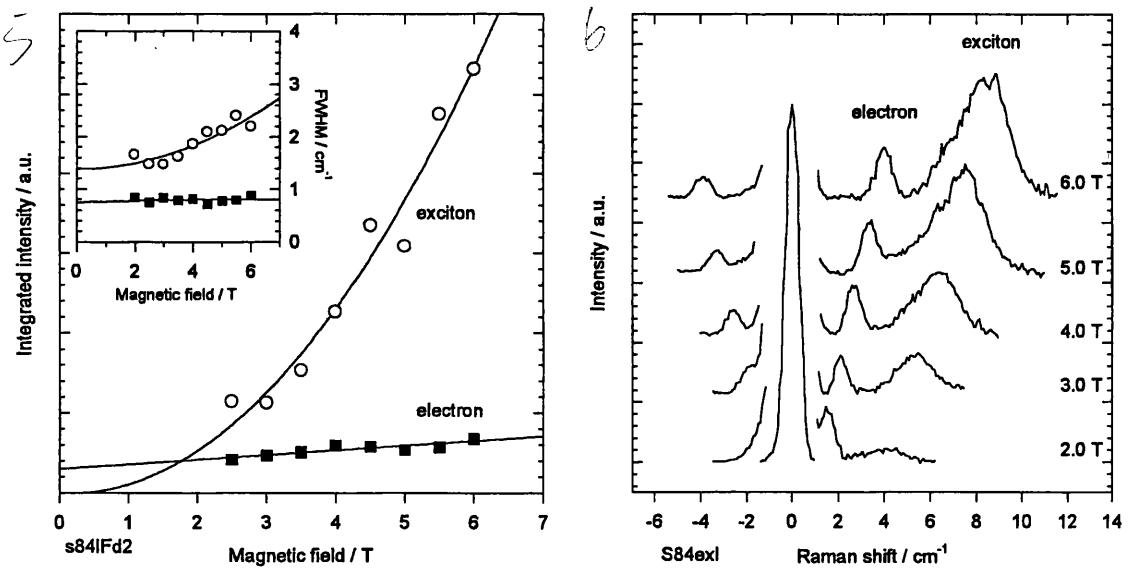

Figures 5.1: (5) Faraday magnetic field dependence of integrated intensity and FWHM (inset) from an undoped $Zn_{0.89}Mg_{0.11}S_{0.2}Se_{0.80}$ quaternary barriers of a 5 nm SQW sample. Electrons and excitons are represented by filled and open symbols, respectively; (6) Faraday SFRS spectra from an undoped ZnMgSSe quaternary SQW barrier for range of magnetic field strengths indicated on right side of the diagram.

The electron signal was detected in all of the ZnSe based material, however, only the quaternary $Zn_{1-x}Mg_xS_ySe_{1-y}$ material examined with compositions $x > 0.1$ and $y > 0.2$ exhibited the new signal. Neither the MOVPE-grown epilayer, with composition $x = 0.07$ and $y = 0.12$, nor the ternary material examined exhibited the new signal.

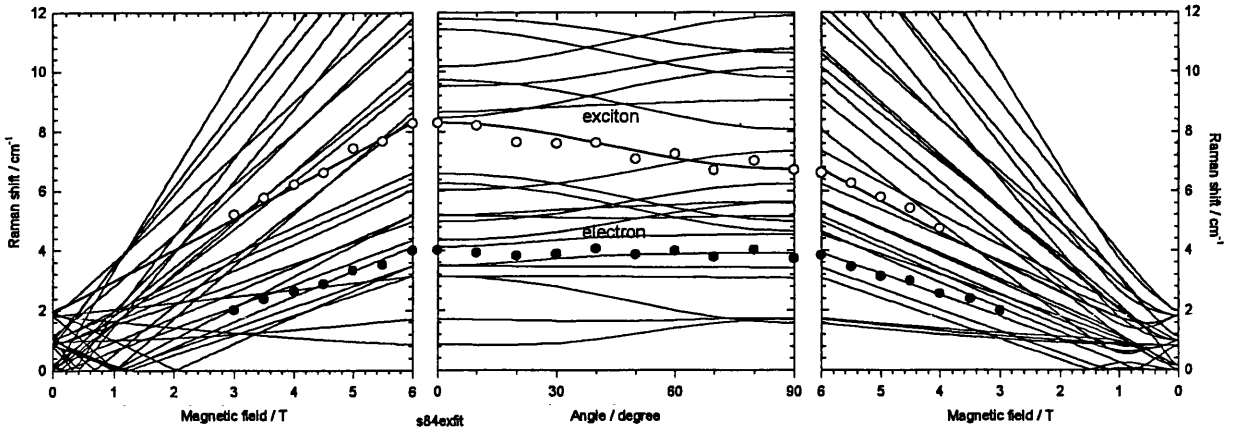

Figure 5.1.7 The field dependent Raman shifts for an undoped ZnMgSSe quaternary SQW barrier, sample S84. Voigt and Faraday electron (filled) and exciton (open) SFRS Raman shift magnetic field dependence, diagrams on left and right sides. Central diagram SFRS Raman shift as a function of magnetic field direction. Lines are results of calculation based on equation (5.1).

Having identified the presence of a new signal it is of interest now to determine its dependence on excitation energy. Figure 5.1.8 shows the raw spectra. In conjunction with the reduction in laser intensity due to the crossed polarization employed in Voigt

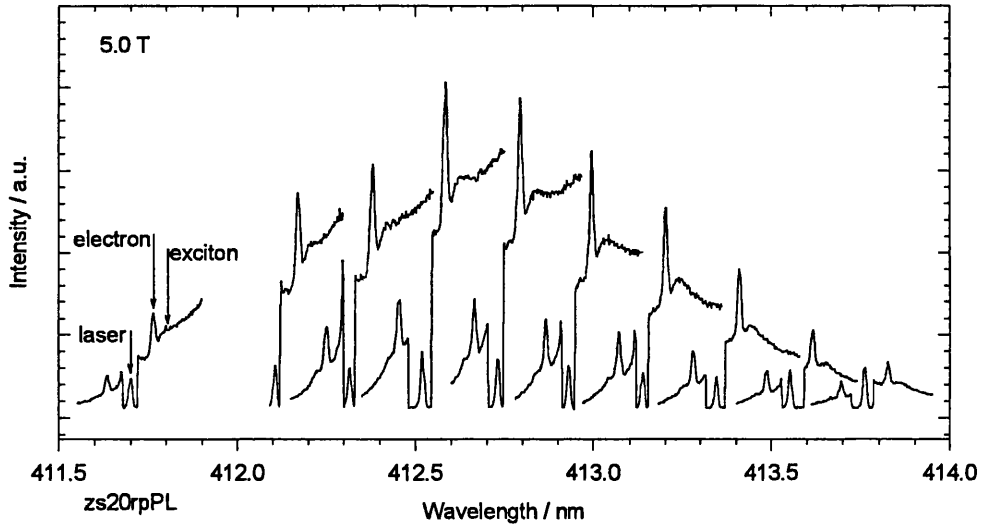

Figure 5.1.8 The dependence of electron and exciton related SFRS signals on excitation wavelength for N-doped epilayer in Voigt geomentry. The raw spectra show electron and exciton related Stoke and anti-Stokes SFRS signals. The central feature in each spectra is the strongly attenuated laser signal.

geometry $z(\pi,\sigma)\bar{z}$, additional attenuation of the laser was provided by a neutral density filter. On the low energy side of the laser line the stronger Stokes signals are clearly observed, together with the PL background which follows the luminescence profile. On the high energy side the anti-Stokes signals of the electron and new signal are also observed. Analysis of these spectra enables the Raman shift dependence on excitation energy and resonance profile to be constructed, figures 5.1.9 and 5.1.10, respectively. It is clear from figure 5.1.9 that the Raman shift of neither signal is

dependent on excitation energy. The resonance profile data indicates that the most intense signals occur on the high energy side of the PL band. Fitting of the data, according to equation (1.39), reveals that the two intensity profiles are coincident, within the limit of the experimental resolution. The linewidths of the PL and resonance profiles were comparable and their separation was ~3 meV.

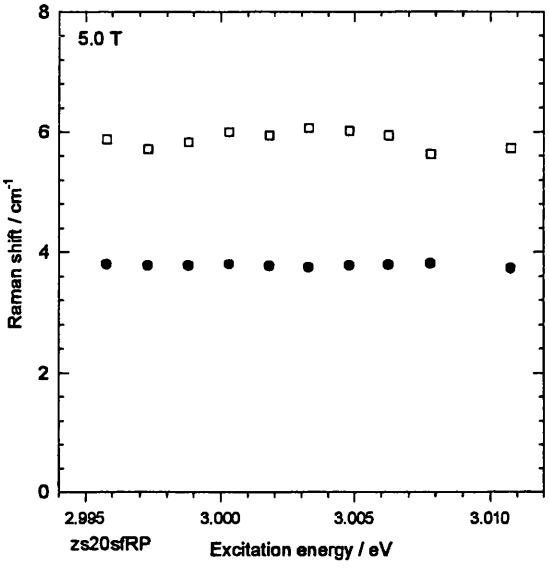

Figure 5.1.9 Raman shift of electron (filled) and exciton (open) fitted SFRS signals, shown in figure 5.1.8, as a function of excitation energy for N-doped epilayer.

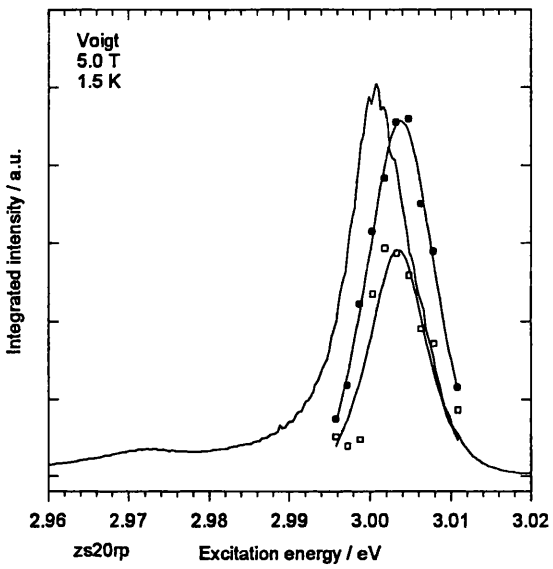

Figure 5.1.10 The integrated intensity of the SFRS signals as a function of excitation energy for N-doped epilayer. PL solid line, electron and exciton related signals filled and open symbols, respectively.

A model is required to account for the observed linearity of the field dependence of the Raman shift, the finite extrapolation at zero field and the 'switching on' of the transition as the magnetic field is increased. In addition, the existence of a small biaxial strain has already been established in these specimens and must also be included in the model. A suitable Hamiltonian to describe these observations is that of an exchange-coupled electron-hole pair with an isotropic exchange interaction in the presence of a biaxial strain. This is given by the following Hamiltonian:

$$H = g_e \mu_B s \cdot B + g_h \mu_B J \cdot B + \delta_1 J \cdot s + \frac{\Delta}{2}\left(J_z^2 - \frac{J[J+1]}{3} \right) \qquad (5.1)$$

where the terms and parameters are as previously defined in sections 1.2.5, 1.2.6 and 4.3. The Zeeman terms describe the magnetic field splitting of the conduction and valence -band spin states. The band-edge states are further split by the exchange constant δ_1, which accounts for the non-zero extrapolation of the Raman shift at zero field. The exchange interaction also introduces mixing between the electron and hole spin states and is therefore responsible for the quadratic magnetic field dependence of

the integrated intensity. The last term describes the biaxial strain. Terms involving the exchange interaction δ_2 and the hole Zeeman parameter q, refer to sections 1.2.6 and 1.2.4 respectively, have been neglected and therefore anisotropic behaviour is introduced solely by the strain term. Justification for this will be given in section 5.2.

The faint lines in figure 5.1.7 depict all 28 possible Stokes SFRS transitions between the eightfold excitonic spin states[1]. The best description of the experimental data is obtained is when $g_e = 1.37$, $g_h = 2.2$, $\delta_1 = 0.10$ meV and $\Delta = 0.11$ meV and is shown by the bold line. The value of g_e is entirely consistent with the measured g-value (above) and with that predicted by the five-band third-order $\boldsymbol{k \cdot p}$ model. No such measurement exist for the hole g-factor for ZnSe-based quaternary alloys and comparison with $\tilde{\kappa}$ determined in sections 4.2-4 for ZnSe:Li, ZnSe:N and ZnMgSe:N are not meaningful, since these values are for holes bound to neutral acceptors and are therefore not directly comparable. An estimate based on the interpolation procedure adopted in section 3.2 for the quaternary alloys, in conjunction with equation (4.7) and the relation $g_h \sim 2\kappa$, yields $g_h = 1.81$. However, it has already been shown that estimates based on the three-band model for II-VI materials are not accurate[2,3], so this apparent agreement may be fortuitous. The exchange parameter is comparable with those determined in other II-VI bulk materials, see discussion below. The strain is consistent with the other alloy specimens examined in this thesis and is therefore considered reasonable. Thus, the experimental observations are adequately described using an excitonic model. It is interesting to note that the signal attributed to an electron bound to a neutral donor, above, could not be fitted simultaneously with the new signal in a satisfactory manner using the excitonic model, indicating that the two signals may indeed derived from different processes.

It is tempting to speculate as to the origin of the signals. The signal at approximately 3.75 cm^{-1} (at 6 Tesla) is entirely consistent with that of electron SFRS in resonance with a shallow donor, as detected in almost all ZnSe-based material. The origin of the new signal is not immediately apparent. The presence of the single quantum well suggests exciton localisation due to interface roughness between the barrier and the well[4,5]. However, the doped epilayer sample also exhibited the new signal without the presence of a quantum well. Therefore, exciton localisation due to interface roughness cannot be invoked to explain the results from both types of sample. Conversely, the barriers in the SQW samples were not intentionally doped, and since

it becomes progressively more difficult to dope binary, ternary and quaternary ZnSe-base material p-type[6], see section 4.4, it therefore seems unlikely that sufficient unintentional p-type impurities exist within the quaternary barriers to meet the SFRS detection threshold and thereby enable hole spin-flip to be detected. Thus, the signal cannot be attributed to acceptor bound SFRS. In fact the signal detected in the doped epilayer is considerably weaker than those detected in the undoped barriers, suggesting perhaps that the presence of the nitrogen impurities may actually inhibit the formation of excitons or offer an alternative recombination route preventing localisation and subsequent detection via this pathway. However, the compositions of both types of sample were similar (Mg content ~ 0.1 and S~0.2), suggesting, finally, the possibility of exciton localisation at potential fluctuations caused by alloy disorder.

It is possible to obtain strong SFRS when the laser is in resonance with the transition energies of exciton localised at quantum wells or potential fluctuations[7-10]. In such cases, the spin-flip occurs in the optically excited, excitonic, state. The incoming photon creates the exciton, which undergoes a change in angular momentum through the intervention of an acoustic phonon, followed by the emission of a photon of lower energy in the Stokes process. The localised character of the excitonic wavefunction leads to the relaxation of $\boldsymbol{k}$-vector conservation in the Raman process. As a consequence, acoustic phonons throughout the entire Brillouin zone can contribute to the scattering process, since the phonon continuum can always provide phonons to fit the Zeeman splitting in this doubly resonant process[11]. The new signal may therefore be attributed to a doubly resonant acoustic-phonon mediated spin-flip process. The interest in such processes stems from the fact that the exchange interaction between the electron and hole can therefore be measured.

Recently, measurement of the exchange interaction has been the subject of intense investigation, particularly in structured materials, where the exchange interaction is enhanced and therefore more easily measured. Reports of exchange constants in bulk material systems range from 0.1 meV[12] to 0.4 meV[13] for ZnSe and from 0.02 meV[14] to 0.37 meV[15] in GaAs. Enhancement of the exchange interaction is anticipated in quantum well(QW) structures[16,17], because the two-dimensional confinement increases the spatial overlap between the electron and hole wavefunctions. In II-VI and III-V based materials exchange interactions from 0.5 to 6 meV have been reported in GaAs/AlGaAs[16,18,19] and (Zn,Cd)Se/ZnSe[20] QW structures, depending on

material and well width. Similar exchange splittings have been reported for CdS/ZnS quantum discs a few monolayers thick[21] and fractional monolayer insertions of CdSe in ZnSe matrix[22,23]. Substantial enhancements are expected in quantum dot (QD) systems, as a result of the three-dimensional confinement[24]. In CdSe QD[21,25] and CdS QD embedded in glass[26] exchange splittings of 12 to 15 meV have been reported.

A preparatory investigation has been conducted on the II-VI quaternary alloy ZnMgSSe. A new signal is observed in juxtaposition with the ubiquitous electron SFRS found in almost all ZnSe based material. The new signal exhibits a distinct magnetic field dependent behaviour different from that previously reported in chapters 3 and 4. The linewidth of the new signal was broader than previously observed SFRS signals, the Raman shift remained finite when extrapolated to zero field and the integrated intensity displayed a quadratic field dependence, such that, the new signal could not be observed below 2 Tesla. Significantly, the signals were observed in two types of sample, a nitrogen-doped epilayer specimen and the undoped barriers of a SQW sample. Observation of the new signal in both types of sample was crucial, since it implied that the new signal was neither doping nor interface related.

An excitonic model accounting for the field dependent behaviour of the new signal was developed and the origins of the signal have been discussed in terms of exciton localisation by alloy fluctuations. The effective Hamiltonian to describe the observed behaviour is that of an isotropic exchange-coupled electron-hole pair in the presence of a biaxial strain. Four parameters were required to fit the field dependent data, the electron and hole g-factors, the bulk exchange splitting and the strain splitting. All of the parameters determined using the excitonic model were found to be reasonable and consistent with those previously reported. The selection rules governing transitions within the localised exciton accounted for the observed field dependence of the integrated intensity of the signal. In zero magnetic field the pure $F = 2$ state is forbidden and therefore completely absent from the optical spectra, with increased magnetic field the transition gains in oscillator strength because of magnetically-induced mixing of the $F = 1$ and 2 states, allowing the transitions to be observed.

The spectra are therefore interpreted as the superposition of two signals originating from two distinct processes. The signal at lower Raman shift arises from the spin-flip of an electron bound to a neutral donor, whilst the slightly broader signal to higher Raman shift is derived from an acoustic-phonon mediated spin-flip transition within a localised exciton. The slightly increased linewidth may be an inherent feature of the

of the phonon assisted process or may indicate that the resonant excitation probes localised states possessing a range of exchange splittings.

The composition range examined in this preparatory study was far from exhaustive and a systematic composition series should be investigated. It has been argued that exciton localisation by potential fluctuations is responsible for the observed field dependent spectra and that therefore the results are a manifestation of the physics of alloying. The crucial test of this assertion is therefore to find supporting evidence in another material system and this follows in the next section.

5.2 The localising potential in AlGaInP

In the previous section magnetic field dependent measurements suggested the existence of excitons localised by potential fluctuations. Potential fluctuations are a general feature of alloy systems and, therefore, these same effects, if correctly interpreted, should be observable in other alloy systems. To test this assertion evidence of exciton localisation will be sought in the AlGaInP alloy system. In this last section the undoped MBE-grown AlGaInP material, initially discussed in terms of the electron gyromagnetic ratio in section 3.4, is reexamined. The section begins with a detailed examination of the compositional dependence of the PL linewidth and lineshape, the composition dependence of the magnetic field dependent signals is then discussed, followed by the magnetic field dependent investigation of the signals and, finally, results from the excitation dependence study are presented.

Presented in figure 5.2.1 is the variation of the PL FWHM with composition for the nominally undoped MBE (open circles) epilayers and, for comparative purposes, data from the p-type MOVPE (filled circles) AlGaInP epilayer specimens is also presented (the dotted lines are a guide to the eye). The two types of sample clearly exhibit different types of behaviour. Qualitatively, the dependence of the nominally undoped MBE material is of the form proposed for exciton localisation[27,28], whilst the dependence of the p-type MOVPE material is consistent with that of bound excitons[29]. However, in both cases quantitative estimates predict narrower linewidths than those obtained experimentally. As discussed in section 3.3, several mechanisms contribute to the inhomogeneous broadening of the excitonic PL linewidth in alloys[30], these include: i) microscopic statistical fluctuations in the composition x and the ordering

parameter η; ii) spatial variation of x and η on the macroscopic scale and iii) excitonic scattering due to defects, such as domain boundaries. However, insufficient knowledge of the microstructure of these specimens prohibits further quantitative analysis.

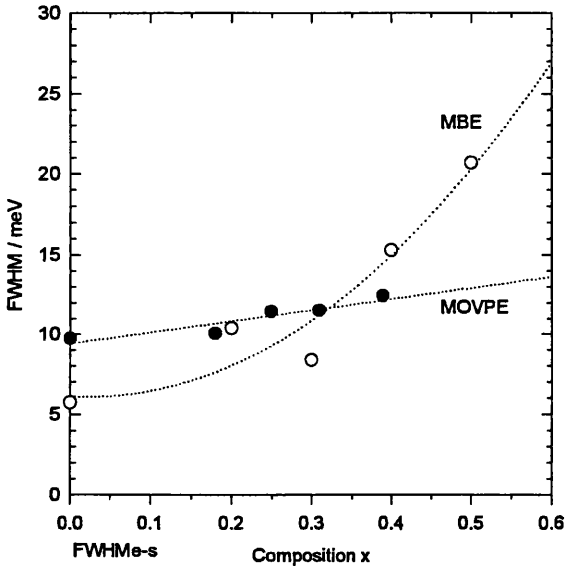

Figure 5.2.1 The compositional dependence of the PL FWHM from $(Al_xGa_{1-x})_{0.52}In_{0.48}P$ epilayers, undoped MBE material (open circles) and p-type MOVPE material (filled circles).

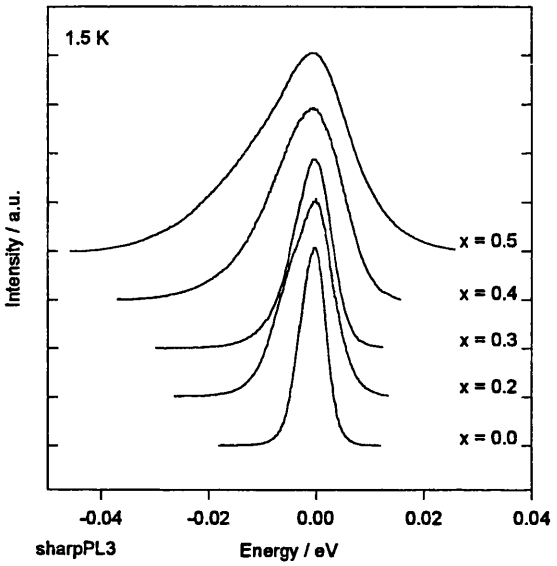

Figure 5.2.2 The compositional dependence of the PL lineshape from undoped $(Al_xGa_{1-x})_{0.52}In_{0.48}P$ epilayers grown by MBE. Note sample with x=0.3 is not from the same growth series as the other material.

The PL lineshapes of the undoped MBE material are shown in figure 5.2.2, offset in energy to facilitate comparison. The lineshape broadens systematically with increasing aluminium content and becomes progressively more asymmetric. The specimen with composition x = 0.3 deviates from this trend; however, as previously noted in section 3.4, this specimen was obtained from a separate growth series to the other samples. The complex PL lineshape has been interpreted[31,32] in terms of exciton localisation due to the effects of disorder on the excitonic states of solid solutions. The possibility of exciton localisation in potential wells produced by large scale fluctuations of composition was first put forward in reference [27]. Of crucial importance is the transitional energy that separates localised excitonic states from delocalised states. In the Mott-Anderson model[33] this transition energy is called the mobility edge, and is well-defined. However, this idealised model neglects the influence of the finite exciton lifetime and the effect of long-range composition fluctuations, which both contribute to a smearing of the sharp threshold of the

interband density of states (DOS), resulting in the formation of localised tail states in the forbidden gap. The expected dependence of the DOS in the tail is given by[27]

$$g(E) \propto exp[-(\varepsilon/\varepsilon_0)^{1/2}] \quad (5.2)$$

where the energy ε is measured downward from the excitonic band-edge and ε_0 is a characteristic energy, depending both on material parameters and the composition of the alloy[27]. The processes leading to the formation of the luminescence band are shown schematically in figure 5.2.3. The right hand portion of the figure shows the energy dependence of the DOS. The PL lineshape does not directly represent the DOS of the exciton band. Instead, the PL lineshape results from the competition between the energy relaxation time of excitons down the disordered exciton energy band and the recombination time. It should be noted that the position of the effective mobility edge does not correspond to any singular point in DOS and must be empirically determined.

Excitons are created in the region of high DOS and possess kinetic energy that exceeds the amplitude of the potential fluctuations. Relaxation via rapid thermalisation reduces the excitons' energy, bringing them into the region of potential relief. In this region spatial migration is possible only through the tunnelling into adjacent localized states. Further energy relaxation results in the complete localisation of the exciton. The relaxation rate for such a process strongly depends on the number of available final states with lower energy and decreases rapidly with the decrease of energy within the tail due to exhaustion of final states. Typically, the radiative recombination time of the excitons is of the order of 10^{-9} s, whereas characteristic times for phonon-assisted energy relaxation for free particles is of the order 10^{-12} s or less[31,32]. As a result the emission intensity for the region of fast relaxation will be small. However, a substantial increase of the emission intensity can be expected for the spectral region corresponding to the free-to-tunnelling transition. In this region the high energy border of the emission band should be situated. The decay of the emission band intensity to lower energies will be given by the decrease of the DOS in the tail, equation (5.2). Thus, without recourse to arguments involving long-range ordering, this qualitative model accounts for two important features of the luminescence: i) the broadening of the optical transitions with alloying due to the formation of a band tail in the vicinity of the band-edge; and ii) the Stokes shift

between the absorption and PL due to the exciton relaxation and recombination dynamics.

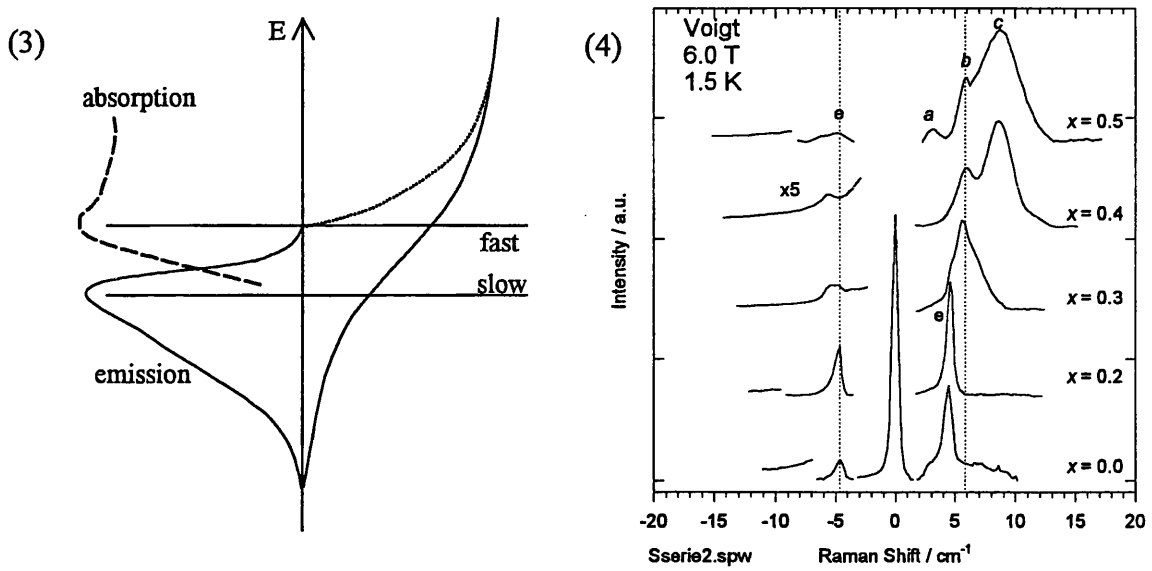

Figures 5.2: (3) A achematic representation of band-edge excitonic process. Right part of the figure shows the energy dependence of the DOS, with the dotted and solid lines corresponding to the bulk three-dimensional DOS and the exponential decay of localised states. The left part shows expected positions of the absorption (dashed line) and PL (solid line); (4) The compositional dependence of the SFRS spectra from undoped $(Al_xGa_{1-x})_{0.52}In_{0.48}P$ epilayers grown by MBE. The composition x is indicated on the right side of the figure. The excitonic signals are labelled *a* to *d* and the electron signal is labelled *e*.

Parallel to the pronounced dependence of the PL lineshape on composition are changes in the observed magnetic field dependent signals. Figure 5.2.4 shows the magnetic field dependent signals obtained from the samples at the excitation energy of strongest resonant enhancement in Voigt geometry at 6 Tesla. The series of spectra show the progressive evolution of four distinct new signals with respect to increasing aluminium content. In the range $0.0<x<0.2$ only the signal attributed to donor bound electron SFRS in section 3.4 is evident in both the Stokes and anti-Stokes portions of the spectra. At $x = 0.3$, three Stokes signals are observed; the electron and two new signals designated *b* and *c*. The Raman shift of the dominant signal *b* corresponds closely to that of the hole (~6 cm^{-1}) observed in the doped material, see section 4.5. The electron signal and the third signal *c* form two weaker shoulders at lower and higher Raman shift with respect to signal *b*. The anti-Stokes portion of the $x = 0.3$ spectra shows the electron SFRS and signal *b*. In the samples with $x = 0.4$ and 0.5 an additional new signal, *a*, is observed close to the laser line. Signal *c* now dominates the Stokes spectra and is observed at higher Raman shift than in the previous specimen. The signal is significantly broader than signal *b*, its FWHM being comparable to the excitonic signal observed in the previous section. Signal *b* is still

apparent in both samples. However, the electron signal cannot be resolved on the Stokes side, but appears in the anti-Stokes portion of the $x = 0.5$ spectrum. In Faraday geometry, see figure 5.2.9 below, one further new signal *d* is observed. No SFRS signals were observed in the next sample in the series, $x = 0.7$, or for those remaining samples with higher aluminium content, as the indirect *X*-band becomes the lowest transition for recombination.

The emergence of these new signals is intimately linked to the increase in the aluminium content and the broadening of the excitonic luminescence. Thus, there is a marked transition, around $x = 0.3$, at which the signal attributed to bound exciton electron SFRS diminishes and the new signals, *a* to *d*, become dominant. Significantly, no such transition was observed in the composition dependence of the doped AlGaInP samples, section 4.6, although a similar trend was exhibited by the ZnMgSSe alloys, in section 5.2.

The integrated intensity as a function of magnetic field is shown for the electron signal in the $x = 0.2$ sample (open circles) and for signals *b* and *c* (filled symbols) from the $x = 0.4$, in the composite figure 5.2.5, the inset shows the FWHM dependence. The electron behaves in accordance with the donor bound SFRS reported in section 3.1, whilst signals *b* and *c* exhibit analogous behaviour to the excitonic signal reported in the previous section for ZnMgSSe. Signal *d* (not shown) exhibited a similar quadratic field dependence in Faraday geometry. Selected spectra are presented in figure 5.2.6.

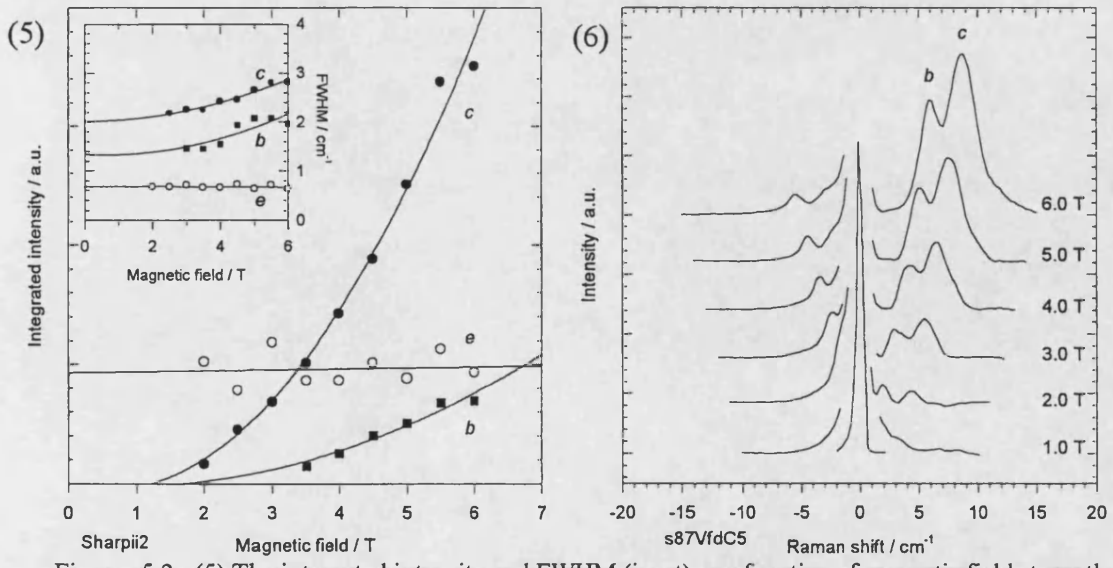

Figures 5.2: (5) The integrated intensity and FWHM (inset) as a function of magnetic field strength for two samples with compositions x=0.2 and x=0.4, open and filled circles respectively; (6) Selected SFRS spectra at the magnetic field strengths indicated on the right of the figure.

In order to clarify the origin of the observed signals, *a* to *d*, a sample with negligible strain was examined. Figure 5.2.7 shows the transitions (solid lines) predicted using the excitonic model, equation 5.1, with the strain term equal to zero and with the g-values $g_e = 1.6$[34,35] and $g_h = 2.1$[35], determined previously for this composition, and an exchange splitting $\delta_1 = 0.16$ meV. With this reasonable parameter set all of the observed Raman shifts are accounted for in both Voigt and Faraday field geometries and in the angular field dependence. The strain-free sample provides an important test of the assumptions made for the excitonic model, equation 5.1. There is no significant anisotropy in the Raman shift of the signals with respect to the orientation of the sample in the magnetic field, indicating that δ_2 and q are indeed small. Thus, the neglection of these terms in the excitonic model is vindicated. Furthermore, the observed isotropic dependence enables the possibility of a crystal field splitting, central to order induced effects, to be eliminated for which a pronounced anisotropic behaviour is predicted, see appendix D.

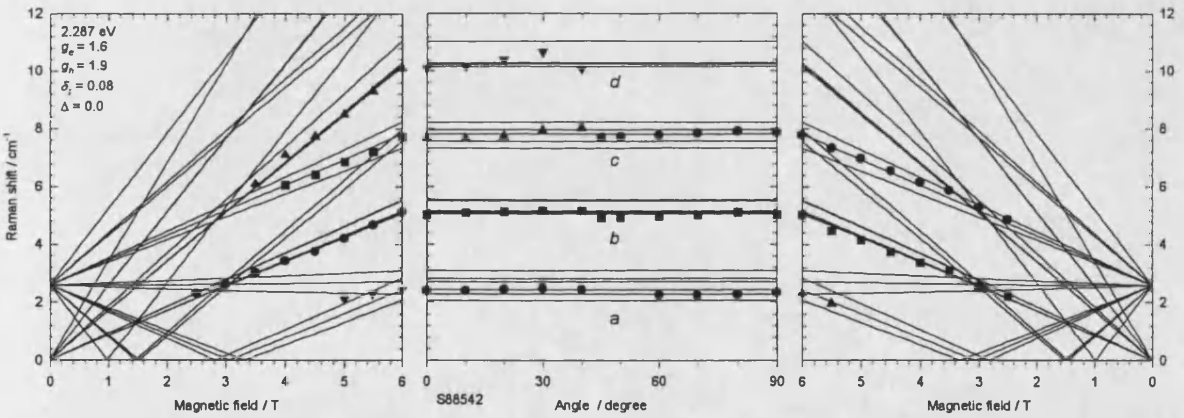

Figure 5.2.7 Magnetic field dependent Raman shifts for the undoped MBE-grown $(Al_{0.5}Ga_{0.5})_{0.52}In_{0.48}P$ epilayer. Outer figures show the Faraday (left) and Voigt (right) magnetic field dependences. The central figure shows the angular dependent variation of the SFRS signals as a function of magnetic field orientation between the growth axis and the direction of the magnetic field. The solid lines are the transitions predicted by the excitonic model, equation (5.1).

It is not possible to identify precisely which transitions give rise to the observed signals. However, the change in total spin projection of the exciton state, Δm_F, for each group of transitions can be determined, see figure 5.2.8. The observed signals may then be attributed to the following subset of transitions: Δm_{Fb} and $\Delta m_{Fc} = 1$, $\Delta m_{Fd} = 2$. Due to the close proximity of signal *a* to the laser line it was not possible to distinguish between $\Delta m_{Fa} = 0$ or 1. Figure 5.2.9 shows the observed spectra for various polarisation orientations. In agreement with the selection rules predicted

using the excitonic model for the observed transitions: Voigt geometry is dominated by signals *b* and *c*, whilst signal *d* dominates Faraday geometry. Signal *a* appears relatively strongly in $z(\pi,\sigma)\bar{z}$, but is not apparent in any of the Faraday polarisations, suggesting that $\Delta m_{Fa} = 1$ is the appropriate selection rule for this transition. The anti-Stokes of signal *c* is observed in $z(\pi,\sigma)\bar{z}$ polarisation. Thus, the observed signals, *a* to *d*, can be attributed to transitions within localised excitons.

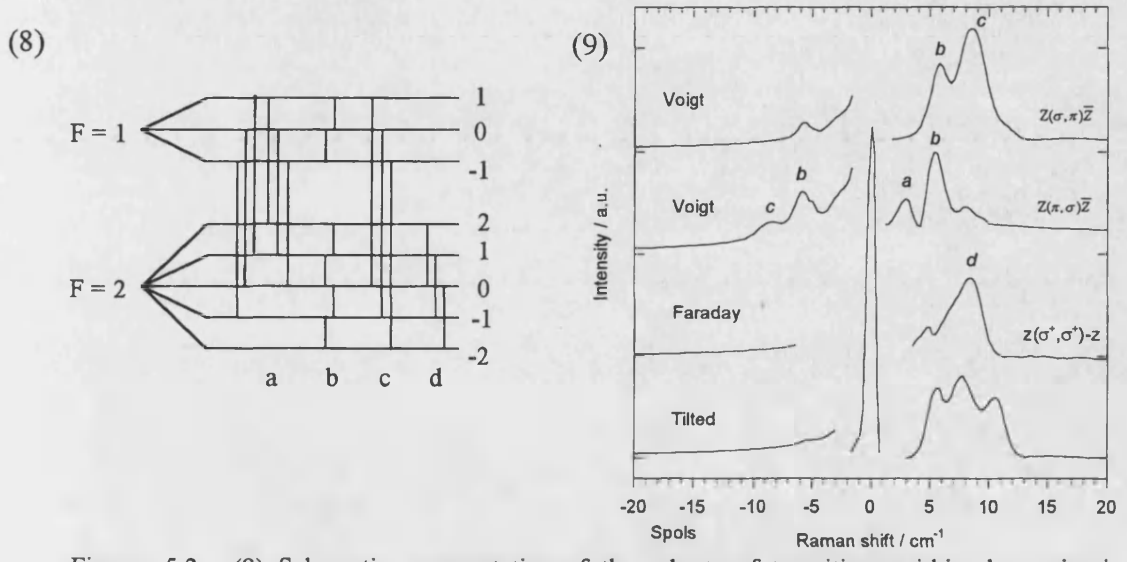

Figures 5.2: (8) Schematic representation of the subsets of transitions within the excitonic manifold; (9) SFRS spectra for different polarisation in various magnetic field geometries.

Figure 5.2.10 below shows the magnetic field dependence and angular dependence for the sample with aluminium content $x = 0.4$. To describe completely this sample it was necessary to include a residual strain $\Delta = 0.14$ meV, otherwise the parameters were similar to those stated above for the strain-free sample.

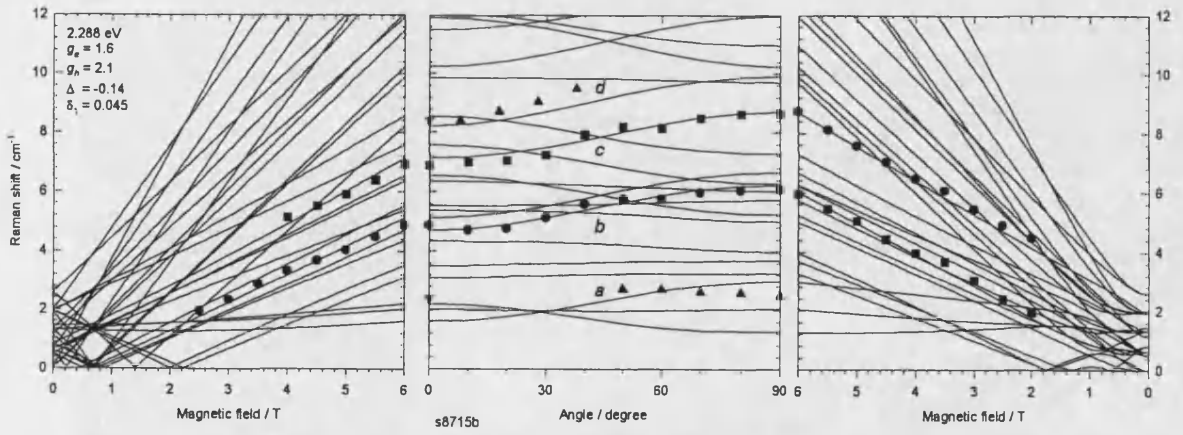

Figure 5.2.10 Magnetic field dependent Raman shifts for the undoped MBE grown $(Al_{0.4}Ga_{0.6})_{0.52}In_{0.48}P$ epilayer. See figure 5.2.7 for other details.

Figure 5.2.11 shows the SFRS intensity variation of signal *b* and *c* as a function of excitation energy for two samples with different degrees of ordering, but with the same composition, $x = 0.4$. Once again the strongest resonance is obtained on the high energy side of the normalised PL peak. However, the separation between the peak of the SFRS intensity profile and the PL peak is noticeably greater in the case of

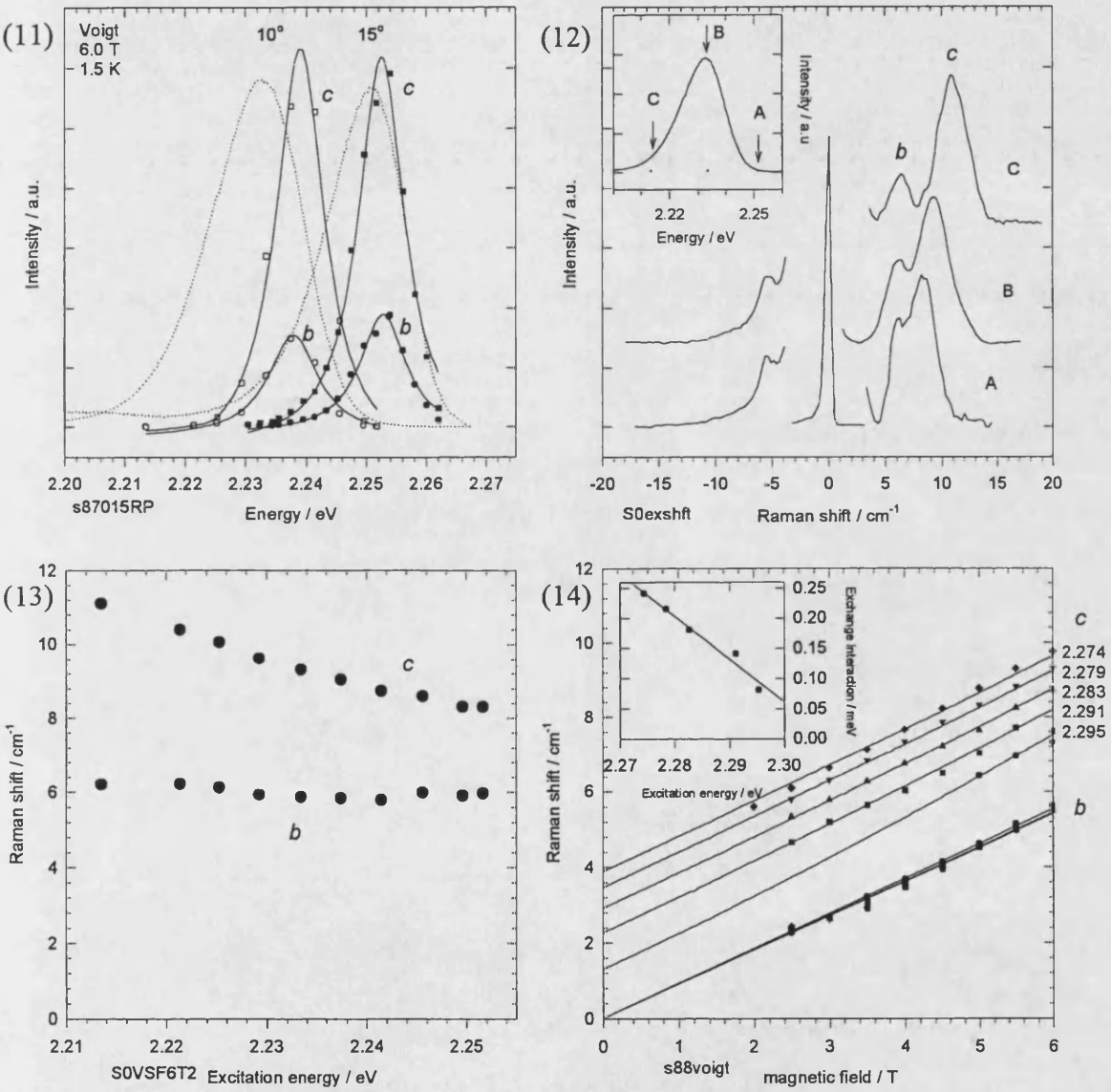

Figures 5.2: (11) SFRS resonance profile data superimposed on the PL spectra $(Al_{0.4}Ga_{0.6})_{0.52}In_{0.48}P$. The SFRS data was fitted using equation (1.39). signals *b* and *c* corresponding to circles and squares, substrate orientations 15° (nearly disordered) and 0° (partially ordered) towards the (111)B direction; (12) The SFRS spectra in $(Al_{0.4}Ga_{0.6})_{0.52}In_{0.48}P$ epilayer for three excitation energies: A = 2.252, B = 2.233, C = 2.214 meV are shown. Spectra normalised to peak *b*. Inset shows the position of excitation in relation to PL; (13) Spin-flip Raman shift as a function of excitation energy for $(Al_{0.4}Ga_{0.6})_{0.52}In_{0.48}P$ epilayer S87(0°); (14) Magnetic field dependences in Voigt geometry as a function of excitation energy for $(Al_{0.5}Ga_{0.5})_{0.52}In_{0.48}P$. The SFRS data was fitted using excitonic model equation (5.1), see text for details. Inset shows dependence of the exchange energy, determined using excitonic model, on excitation energy.

the more ordered specimen. In both cases the FWHM of the SFRS profile is narrower than the corresponding PL FWHM, suggesting that the latter does not arise from a single process.

Spectra in resonance with the PL band at different excitation energies are shown in figure 5.2.12. The spectra were normalised to the integrated intensity of peak *b*. It is evident from this figure that the Raman shift of signal *b* is independent of excitation energy, whilst the Raman shift of signal *c* reduces as the excitation energy is increased. These findings are entirely consistent with the model, see figure 5.2.8, provided the observed splitting between the $F = 1$ and $F = 2$ excitonic states is permitted to be a function of the excitation energy. The systematic trend is shown clearly by the fitted data in figure 5.2.13.

To investigate this behaviour further a series of magnetic field dependence measurements were performed as a function of excitation energy. Figure 5.2.14 shows the Voigt geometry data obtained from the strain-free specimen with $x = 0.5$. The data were fitted using the excitonic model, equation (5.1). It is important to note that all the fitted curves were obtain by adjusting one parameter only, the exchange splitting δ_1. The inset, figure 5.2.14, shows the exchange energy E_{ex}, determined using the excitonic model, as a function of excitation energy. It is clear, from the inset, that the exchange constant is linearly dependent on excitation energy. The constant of proportionality for the specimen was 0.0074. Experiments conducted on specimens with different composition and degrees of ordering produced the same result, that is, the exchange energy is a linear function of energy. Figure 5.2.15 shows the normalised PL spectra from two samples with the same composition $x = 0.4$, but different degrees of ordering, the PLE[36] from the disordered sample is also shown, together with the exchange energy data, determined using the excitonic model, as a function of excitation energy from the two specimens. Extrapolation of the data indicates that both sets of data converge to the same point, which corresponds closely with the peak in the absorption. This convergence suggests the existence of an effective excitonic mobility edge, below which transitions within localised excitons become observable through acoustic-phonon assisted SFRS. The excitation energy may then be interpreted as a localisation energy E_{loc}, corresponding to band tail potential fluctuations of different depths. The excitonic wavefunction experiences

stronger confinement as the well depth increases, producing a commensurate change in the exchange interaction, thus accounting for the observed excitation dependence.

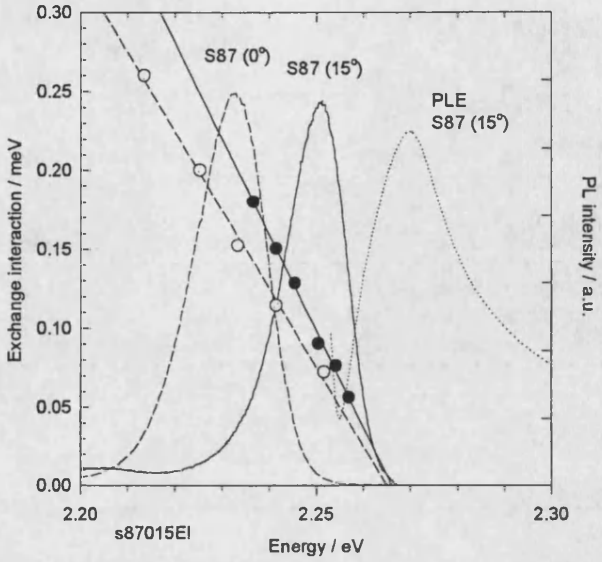

Figure 5.2.15 Excitation energy dependence of exchange energy, determined using the excitonic model, for $(Al_{0.4}Ga_{0.6})_{0.52}In_{0.48}P$ epilayers with partially ordered (open circles) and nearly disordered (filled circles) material. Nearly disordered PL and PLE solid and dotted lines. Partially ordered PL dashed line.

The existence of an effective mobility edge in a disordered system has never been satisfactorily established experimentally[37], since it is not manifest in optical spectra. Previous attempts to determine its position have relied on empirical definitions, such as, the portion of the spectrum where the radiation intensity was reduced to $\sim 10^{-2}$ of the value of the emission band maximum[38]. However, the convergence of the excitation dependence of the exchange energy to the same point may indicate the existence of an effective mobility edge.

The relation between the exchange splitting E_{ex} and localisation energy E_{loc} may be understood more fully by consideration of the confining potential. Considering the effect of localisation on the exciton wavefunction by a one-dimensional potential well of depth V_0 and with a width which is small compared with the exciton radius. The square of the amplitude of the exciton wavefunction $\psi(0)$ becomes enhanced by a factor:

$$\alpha = \left(\frac{2mE_{loc}}{\hbar^2} \right)^{1/2} \pi^{1/3} a_0 \qquad (5.3)$$

If the exciton is localised by a two-dimensional potential, the increase in $\psi(0)^2$ will be given by α^2, assuming that there is no change in the wavefunction in the direction normal to the plane of the well. Similarly, if the localisation is caused by a three

dimensional fluctuation, $\psi(0)^2$ will be enhanced by α^3. Thus, in accordance with the simple model, a linear dependence is provided by a weak two-dimensional confining potential with the gradient given by

$$\frac{E_{ex}}{E_{loc}} = \frac{2m_0\pi^{2/3}a_0^2E_{ex}^{3D}}{\hbar^2}\frac{m^*}{m_0} \qquad (5.4)$$

A linear relationship was recently reported[22,23] for fractional monolayer insertions of CdSe in ZnSe. The CdSe is believed to form two-dimensional disc-like structures, the lateral extent of which in the layer plane is much smaller than the exciton radius. Using appropriate excitonic values of the bulk exchange splitting E_{ex}^{3D} = 0.13 meV[25], the Bohr radius a_0 = 50 Å and the reduced mass m^* = 0.13 the gradient predicted using the above expression is 0.026, this compares favourably with the experimentally determined gradient of 0.022. In the present case, the bulk excitonic exchange splitting is not known for AlGaInP. However, using the gradient 0.0074 determined from figure 5.2.14, together with reasonable estimates of the excitonic Bohr radius and the reduced effective mass, 64 Å and 0.096 respectively, the following prediction of the bulk exchange splitting for AlGaInP was obtained, E_{ex}^{3D} = 0.03 meV; which, though small, is consistent with values reported for other III-V semiconductors.

The compositional dependence of the alloy AlGaInP has been investigated using PL and SFRS in the range $0<x<0.5$. A qualitative explanation of the Stokes shift between the PL and absorption maxima and the gradual broadening of the PL linewidth, with increasing Al content, in terms of exciton localisation at alloy fluctuations has been given. A remarkable evolution of the magnetic field dependent signals with composition was observed in parallel to the compositional dependence of the PL: this was also explained in terms of exciton localisation at alloy fluctuations. In the range $0<x<0.2$ only bound exciton electron SFRS was observed; however, in specimens with higher Al content, $0.3<x<0.5$, the Stokes signal was either absent or unresolvable and only weakly present in the anti-Stokes portion of the spectra. Instead, four new signals were observed, that displayed analogous magnetic field dependent behaviour to the signal attributed to the localised exciton reported in the previous section for quaternary ZnSe-based alloys. The observed transition from the bound exciton regime to that of excitons localised by potential fluctuations may possibly be attributed to quenching of the bound exciton states by the fast exciton localisation at alloy fluctuations. The excitonic model proposed in section 5.1 was found to be equally successful in describing the phosphide-based material results. Reasonable

parameters were determined using the excitonic model for material with different composition, strain state and states of ordering. The signals were all attributed to subsets of the excitonic manifold. These assignments were supported by polarization measurements. Furthermore, the opportunity to investigate a strain-free specimen provided an important test of the assumptions made in developing the excitonic model in section 5.1. The signals were found to be isotropic with respect to the orientation of the magnetic field in the absence of strain, justifying the neglection of anisotropic valence-band spin-Hamiltonian q and exchange interaction δ_2 parameters. In addition it demonstrated that order induced effects were not significant.

In contrast to the reported findings in the previous section, the excitation dependence of the exchange splitting δ_1 was found to depend linearly on the localisation depth. A simple model put forward accounting for this linear dependence implied that the excitons were localised by a weak two-dimensional confining potential. The model was found to predict correctly the order of magnitude of the proportionality constant for CdSe/ZnSe system, reported elsewhere, and to provide a reasonable estimate of the three-dimensional exchange constant in AlGaInP, given the experimentally obtained constant of proportionality. In the CdSe/ZnSe system the fractional monolayers are known to form two-dimensional islands. The detailed microstructure of the AlGaInP material examined here was unknown; however, considering the tendency of AlGaInP to manifest spontaneous long-range CuPt-type ordering, the formation of two-dimensional islands in the MBE-grown material is not implausible[39-41]. Further work is required to establish the correlation between the microstructure and the observed linear dependence.

Examination of two specimens with the same composition $x = 0.4$, but different degrees of ordering, yielded a further intriguing result. The extrapolation of the exchange parameter as a function of excitation energy for both sets of data converged to the same point, which corresponded closely to the peak in the absorption. This convergence may indicate the existence of an excitonic mobility edge.

All of the observations obtained in this section have been explained qualitatively in terms of exciton localisation. Additionally, the excitonic model and the model of exciton localisation have provided quantitative results that compare favourably with the experimental findings. Thus, compelling evidence has been established indicating that the III-V quaternary alloy AlGaInP exhibits effects of weak excitonic localisation

at potential fluctuations. Furthermore, through the distinct magnetic field dependence observed using SFRS, it is clear that these results are directly analogous to those observed in the II-VI quaternary alloy ZnMgSSe, indicating that exciton localisation in disordered alloys is indeed a general phenomena.

5.3 References

[1] K. Cho, S. Suga, W. Dreybrodt and F. Willmann, Phys. Rev. B **11** 1512 (1975

[2] M. Cardona, J. Phys. Chem. Solids **24** 1543 (1963)

[3] M. Willatzen, M. Cardona and N. E. Christensen, Phys. Rev. B **51** (1995) 17992

[4] Z. Zhu, H. Yoshihara, K. Takebayashi and T. Yao, Appl. Phys. Lett. **63** (1993) 1678

[5] M. Ramsteiner, R. Hey, R. Klann, U. Jahn, I Gorbunova and K.H. Ploog, Phys. Rev. B **55** (1997) 5239

[6] B. Jobst, S. Strauf, P. Baume, E. Kurtz, H. Schenk, D. Hommel and G. Landwehr, Int. Sym. Blue Laser and light Emitting Diodes, Chiba Univ., Japan, March 5-7, 1996, We-P01

[7] V.F. Sapega, M. Cardona, K. Ploog, E.L. Ivchenko and D.N. Mirlin, Phys. Rev. B **45** (1992) 4320

[8] V.F. Sapega, V.I. Belitsky, T. Ruf, H.D. Fuchs, M. Cardona and K. Ploog, Phys. Rev. B **46** (1992) 16005

[9] V.F. Sapega, T. Ruf, M. Cardona K. Ploog, E.L. Ivchenko and D.N. Mirlin, Phys. Rev. B **50** (1994) 2510

[10] A.A. Sirenko, T. Ruf, N.N. Ledentsov, A.Y. Egorov, P.S. Kop'ev, V.M. Ustinov and A.E. Zhukov, Sol. Stat. Comms.**97** (1996) 169

[11] A.A. Sirenko, V.I. Belitsky, T. Ruf, M. Cardona, A.I. Ekimov, C. Trallero-Giner, Phys. Rev. B **58** (1998) 2077

[12] F. Kubacki, J. Gutowski, P. Ruppert, D. Hommel and G. Landwehr, Mater. Sci. Forum **182/184** (1995) 223

[13] H. Mayer, U. Rossler, S. Permogorov, H. Stolz, H. Vogelsang and W. von der Osten, J. Cryst. Growth **138** (1994) 195

[14] W. Ekardt, K.Losch, and D. Bimburg, Phys. Rev. B **20** (1979) 3303

[15] M.A. Gilleo, P.T. Bailey and D.E. Hill, Phys. Rev. **174** (1968) 898

[16] Y. Chen, B. Gil, P. Lefebvre and H. Mathieu, Phys. Rev. B **37** (1988) 6429

[17] Al.L. Efros, M. Rosen, M. Kuno, M. Nirmal, D.J. Norris and M. Bawendi, Phys. Rev. B **54** (1996) 4843

[18] R. Bauer, D. Bimberg, J. Christen, D. Oertel, D. Mars, J.N. Miller T. Fukunaga and H. Nakashima, Proc.18th Int. Conf. Phys. Semicond., Stockholm 1986, Ed. O. Engstrom,(World Sci. Pub. Co., Singapore1987)

[19] M. Potemski, J.C. Maan, A. Fasolino, K. Ploog and G. Weimann, Surf. Sci. **229** (1990) 151

[20] J. Puls and F. Henneberger, Phys. Stat. Sol.(a) 164 499 (1997)

[21] U. Woggon, F. Grindele, W. Langbein and M. Hetterich, Phys. Stat. Sol.(a) **164** (1997) 505

[22] O.Z. Karimov, D. Wolverson, J. J. Davies, T. Ruf and L.N. Tenishev, Phys. Stat. Sol.(a) **215** (1999) 373

[23] T. Ruf, O.Z. Karimov, D. Wolverson, J. J. Davies, A.N. Reznitsky, A.A. Klochikhin, S.Yu. Verbin, L.N. Tenishev, S.A. Permogorov and S.V. Ivanov, Physica B **273-274** (1999) 911

[24] T. Takagahara, Phys. Rev. B 47 (1993) 4569

[25] M. Nirmal, D.J. Norris, M. Kuno, M. Bawendi, Al.L. Efros and M. Rosen, Phys. Rev. Lett. **75** (1995) 3728

[26] U. Woggon, F. Grindele, O. Wind and C.Klingshirn, Phys. Rev. B **54** (1996) 1506

[27] S.D. Baranovskii and A.L. Efros, Sov. Phys. Semicond. **12** (1978) 1328

[28] A. Lusson, R. Legros, Y. Marfaing and H. Mariette, Sol. Stat. Comms.**67** (1988) 851

[29] E.F. Schubert, E.O. Göbel, Y. Horikoshi, K. Ploog and H.J. Queisser, Phys. Rev. B **30** (1984) 813

[30] Y.Zhang, A. Mascarenhas, S. Smith, J.F. Geisz, J.M. Olson and M. Hanna, Phys. Rev. B **61** (1999) 9910

[31] S. Permogorov and A. Reznitsky, J. Lumin. **52** (1992) 201

[32] U. Dörr, H. Kalt, D.J. Mowbray and C.C. Button, Appl. Phys. Lett. **72** (1998) 821

[33] N.F. Mott and E.A. Davis, '*Electronic Processes in Non-Crystalline Materials*', 2nd ed. (Oxford Uni. Press 1979)

[34] A.A. Sirenko, T. Ruf, A. Kurtenbach and K. Eberl, in Physics of Semiconductors, Wurzburg 1996, Ed. M. Scheffler and R. Zimmermann, (World Scientific, Singapore 1996) p. 1385

[35] I.J. Griffin, D. Wolverson, J.J. Davies, M. Emam-Ismail, J. Heffernan, A.H. Kean S.W. Bland and G. Duggan, Semicond. Sci. Technol. **15** (2000), to be published

[36] private communication S.P. Najda

[37] E. Cohen and M.D. Sturge, Phys. Rev. B **25** (1982) 3828

[38] A.G. Abdukadyrov, S.D. Baranovskii, S. Yu. Verbin, E.L. Ivchenko, A. Yu. Naumov and A.N. Reznitskii, Sov. Phys. JETP **71** (1990) 1155

[39] U. Kops, R.G. Ulbrich, M. Berkard, C. Geng, F. Scholz and M. Schweizer, Phys. Stat. Sol. (a) **164** (1997) 159

[40] U. Kops, P.G. Blome, M. Wenderoth, R.G. Ulbrich, C. Geng and F. Scholz, Phys. Rev. B **61** (2000) 1992

[41] U. Dörr, H. Kalt, D.J. Mowbray and C.C. Button, Appl. Phys. Lett. **72** (1998) 821

Conclusion

The behaviour of electrons, holes and excitons in binary, ternary and quaternary wide-bandgap II-VI and III-V semiconductor alloys have been investigated, using photoluminescence, resonant vibrational Raman scattering and spin-flip Raman scattering spectroscopies. The emission energies of the alloys spanned almost the entire visible spectrum (3.1 eV to 2.3 eV). The continuous wave excitation in the desired spectral range was achieved after considerable effort using tuneable dye lasers. The $\boldsymbol{k \cdot p}$ approximation was employed throughout the study for the interpretation of the magneto-optical spectroscopic results.

An excellent illustrative example of a binary alloy was provided by ZnSe, which exhibits all of the characteristic optical features commonly associated with binary alloys, such as narrow excitonic emission lines and donor-acceptor pair luminescence; in addition, strain, introduced by a relatively small lattice mismatch for epitaxial ZnSe on GaAs substrates, and the compensation process have been studied extensively. Furthermore the principle investigative technique SFRS has a proven ability in the examination of the excitonic features of ZnSe. The ZnSe material examined using PL and SFRS was produced using a variety of growth techniques and had a wide range of crystal qualities, doping concentrations and dopant species. Despite variation in the impurity species and crystal quality the electron SFRS signal was invariably detected, in resonance with the free-exciton or shallow donor, with its characteristic gyromagnetic ratio in ZnSe. The insensitivity of the electron gyromagnetic ratio to the chemical species of shallow donor and to the local environment was attributed to the extended nature of the electron wavefunction. This is also manifest in the magnetic field dependence of the shallow donor SFRS, which revealed that the FWHM is independent the field strength and that the integrated signal intensity was only weakly field dependent. In contrast the magnetic field dependence of acceptor bound hole SFRS was found to differ significantly between specimens, although the systematic trends were the same, that is, the FWHM suffered field dependent inhomogeneous broadening, whilst the integrated intensity displayed a quadratic field dependence, but remained finite at zero field. These results reflect the greater sensitivity of the hole to its local environment, produced by the relatively small extent of the hole wavefunction. Thus the magnetic field dependence of the electron and hole bound to neutral impurity centres was established.

In earlier work a model was developed, based on the Luttinger spin Hamiltonian and the Bir and Pikus strain Hamiltonian, that accounted for the variation of the SFRS signals with the orientation of the magnetic field in biaxially strained material. This model enabled the valence band spin Hamiltonian parameters for nitrogen acceptors to be deduced, together with the sign and magnitude of the strain within the epilayer. The model predicted isotropic behaviour for conduction-band related states and manifestly different anisotropic behaviours for the light and heavy hole valence band states, thus, enabling the different valence band states to be distinguished. It was also demonstrated that precise determination of the strain splitting was also possible for layers in which the strain splitting was too small for the excitonic transitions involving the light and heavy hole states to be resolved by PL and PLE. Thus, it was demonstrated that hole SFRS provides an extremely sensitive probe of small strains.

The alternative p-type dopants lithium and phosphorus in ZnSe were investigated. The presence of an anomalous PL feature in phosphorus-doped ZnSe has been the subject of controversy. In this study SFRS was instrumental in the identification of the PL feature, suggesting that it formed as a consequence of the existence of a compensating phosphorus shallow donor centre. Although further work is required to confirm these findings, this result is significant, because the existing models of compensation are nitrogen specific and little attention has been paid to the alternative p-type dopants. Selective excitation and a SFRS resonance profile enable the binding energy, which is slightly larger than the principal substitutional donors, to be estimated. The first observation of the lithium acceptor spin-flip signal has also been reported, with acceptor spin-Hamiltonian parameters similar to those determined for nitrogen acceptors in unstrained ZnSe epilayers. This agreement is not coincidental, since both nitrogen and lithium have similar binding energy depths. In order to gain a deeper insight into the p-type doping and compensation processes in ZnSe it is essential that further studies of alternative dopants are conducted.

The introduction of small amounts of isoelectronic impurities was found to have a dramatic effect on the band-edge luminescence in the II-VI and III-V alloys examined. The random distribution of atoms on their respective sublattices in the alloy systems introduces new physics not found in elemental or binary semiconductors, which strongly influences the optical properties of the semiconductor. The narrow emission lines observed in the PL spectra of binary materials are strongly modified and pronounced inhomogeneous broadening of the

excitonic features resulted. Crucially, SFRS signals were found not to suffer from this broadening and sharp spectral SFRS features were observed for excitation in resonance with the inhomogeneously broadened luminescence. A striking feature of ternary and quaternary SFRS spectra was the simultaneous observation of conduction and valence -band related signals, presenting the difficulty of the definitive identification of these signals. This does not occur in binary material for which the excitonic centre transition energies are distinct and well-defined. The problem was overcome in the alloys by exploiting of the sensitivity of the hole SFRS signals to strain. The presence of a small strain or its deliberate introduction, via the removal of the substrate, enabled the unambiguous identification of SFRS signals. The deliberate introduction of strain in a p-type GaInP epilayer enabled the definitive identification of the electron and hole SFRS signals. Thus, analysis of the anisotropic hole SFRS signal provides an extremely powerful method for identifying the origin of the observed signals; in addition to precisely determining the strain in the near latticed matched epilayers.

The influence of substrate orientation on the PL and SFRS from GaInP was also examined. The near-Gaussian PL lineshape was found to be broadened symmetrically with increased substrate misorientation. The observed behaviour was attributed to the dependence of domain size on substrate orientation, implying, in this instance, that the domain size determined the excitonic linewidth. These findings were in agreement with the phenomenological explanation offered by Zunger *et al.* The SFRS electron gyromagnetic ratio was found to be completely insensitive to the substrate orientation, despite a significant change in the bandgap energy, possibly indicating that the lateral extent of the ordered domains is on a scale less than that of the excitonic radius in the MBE material.

The first measurements of the compositional dependence of the electron and hole gyromagnetic ratio in the quaternary alloy system $(Al_xGa_{1-x})_{0.52}In_{0.48}P$, in the range $0<x<0.5$, were reported. Reasonable agreement was found using three-band $\boldsymbol{k \cdot p}$ theory between the predicted compositional dependence of electron gyromagnetic ratio and the experimentally measured values, enabling discrimination between different sets of bandstructure parameters reported in the literature. However, as expected the agreement was poorer for the hole dependence. Despite a pronounced change in the bandgap, variation of the spin-orbit splitting and the energy momentum

matrix element conspired to produce only a weak compositional dependence of the electron and hole gyromagnetic ratios. In contrast the trend in compositional dependence of the electron gyromagnetic ratio in the quaternary alloy system ZnMgSSe was found to be a pronounce function of the bandgap energy. This was also adequately described using $\boldsymbol{k}\cdot\boldsymbol{p}$ theory, although a five-band third-order expression was required. Many important bandstructure parameters essential for the $\boldsymbol{k}\cdot\boldsymbol{p}$ calculation are as yet undetermined for these alloys and were estimated using simple arguments based on other II-VI and III-V materials. A further interesting comparison between the alloy systems concerns the feature observed on the low energy side of the dominant excitonic emission band in the PL spectra. Observation of analogous features in both ZnMgSSe and AlGaInP alloys corresponding closely in each case to the dominant vibrational modes of the respective alloy, strongly suggest the identification of the feature with a phonon replica.

In addition to the features observed in ternary alloys new field dependent phenomena were observed in the quaternary alloys. Previously unreported signals were observed in resonance with the broad luminescence emission band of the quaternary alloys ZnMgSSe and AlGaInP. In both alloys the signals exhibit analogous behaviour. A preparatory investigation conducted on the II-VI quaternary alloy ZnMgSSe indicated that the new signals were neither doping nor interface related. Whilst a more comprehensive study of the alloy AlGaInP demonstrated that the signals were observed for a variety of different compositions, strain states and states of ordering. The new signals were observed in juxtaposition to the commonly detected impurity bound or free-excitonic SFRS signals. The new signals exhibited a distinct magnetic field dependent behaviour different from that previously reported for impurity bound centres. The linewidth of the new signals were broader than the previously observed SFRS signals, the Raman shift remained finite when extrapolated to zero field and the integrated intensity displayed a quadratic field dependence, such that, the new signals were not observed below a threshold magnetic field strength. An excitonic model was proposed, which accounted for all of the observed magnetic field dependent behaviour in terms of intra-excitonic transitions between electric-dipole allowed and forbidden states of an isotropic exchange-coupled electron-hole pair in the presence of a biaxial strain. The proposed excitonic model required four parameters, the electron and hole gyromagnetic ratios, which had been determined earlier in this investigation, the strain

energy, which had also been previously determined, and the excitonic exchange splitting energy, which was undetermined for both alloys, but was expected to be of the order of a few meV by analogy with bulk binary alloys. The successful application of this excitonic model in conjunction with other experimental observations indicated that the correct interpretation of the findings was that of exciton localisation by alloy fluctuations. The observed magneto-optical signals were therefore attributed to acoustic-phonon mediated spin-flip transitions within a weakly localised exciton. Further support for this hypothesis came from the observed dependence of the exitonic luminescence linewidth and lineshape on the aluminium content of the MBE-grown AlGaInP alloys. This could be accounted for qualitatively using the model of band-edge smearing proposed by Baranovskii *et al.* This model also naturally accounted for the observed Stokes shift between the PLE and the PL. Finally, attempts to model the data using a crystal field splitting, central to the phenomenological explanation proposed by Zunger *et al* for ordered systems, resulted in pronounced anisotropic angle dependent behaviour, relative to the orientation of the magnetic field and the growth axis, which was not observed experimentally.

The emergence of the excitonic signals in the phosphide-based material was intimately linked to the increase in the aluminium content and the broadening of the excitonic luminescence. A marked transition occurred at which the signal attributed to bound exciton electron SFRS diminished and the excitonic signals became dominant. The transition from the bound exciton regime to that of excitons localised by potential fluctuations was attributed to quenching of the bound exciton states by the fast exciton localisation at alloy fluctuations. Significantly, no such transition was observed in the p-doped AlGaInP grown by MOVPE, for which the PL and SFRS spectra exhibited compositional dependent behaviour that could be attributed to bound excitonic processes.

The highly selective nature of SFRS, in resonance with the excitonic emission band, enabled excitons at varying degrees of localisation to be detected. The excitation dependence of the exchange splitting, determined using the excitonic model, was found to depend linearly on the localisation depth in the AlGaInP material grown by MBE. A simple model put forward accounting for this linear dependence implied that the excitons were localised by a weak two-dimensional confining potential. The model was found to predict correctly the order of magnitude of the gradient of the exchange energy as a function of localisation energy for CdSe/ZnSe system, reported

elsewhere, and to provide a reasonable estimate of the three-dimensional exchange constant in AlGaInP, given the experimentally obtained gradient. The fact that the experimentally determined exchange constant corresponds closely to the bulk value in III-V materials and not to those of the low-dimensional systems, further supports the assertion that the excitons are weakly localised and not subject to strong confinement. This is entirely consistent with the nature of localisation by potential fluctuations. The extrapolation of the exchange energy as a function of excitation energy for two specimens with the same composition, but different degrees of ordering converged to the same point, which corresponded closely to the peak in the absorption. This convergence may indicate the existence of an excitonic mobility edge, below which the localised character of the excitonic wavefunction leads to the relaxation of the k-selection rule, enabling transitions within the exciton to become observable through acoustic-phonon assisted SFRS. Previous to these measurements, the existence of the mobility edge had never been satisfactorily established experimentally. In contrast to the above findings the excitation dependence of the excitonic signal in ZnMgSSe was found to be independent of excitation energy. However, unlike the MBE-grown phosphide-based material, which has only cation substitution, the ZnMgSSe material is subject to both cation and anion isoelectronic substitution. The latter is therefore believed to result in stronger excitonic localisation.

Measurements indicate that alloys have a well defined energy bandstructure analogous to those of conventional binary semiconductors, implying that any variation in the nominal alloy composition or crystal structure occurs on a dimension significantly smaller than the excitonic radius. Conversely, the phonon Raman scattering results show the clear presence of interactions between optical phonons and binary semiconductor vibrational modes, indicating that on the scale of the unit cell alloys do not behave like the homogeneous materials of the virtual crystal approximation. This is supported by EXAFS studies. The detailed microstructure of the alloys examined is not fully understood. In GaInP the effects of long-range ordering are well established and the existence of antiphase boundaries in partially ordered material has been shown to form disc-like islands and these islands have been correlated with the detection of localised excitonic emission by micro-PL measurements. In AlGaInP the tendency to order may increase with increasing aluminium content, though, further work is required to confirm this. The alloy ZnMgSSe does not exhibit long-range order, despite the theoretical prediction of large

ordering effects in virtually all III-V and II-VI alloys. The role of short-range order in both alloys has received little or no attention. In terms of growth method it is widely accepted that MOVPE-grown material exhibits a greater propensity to spontaneously long-range order, than material grown by MBE. Interestingly, the partially ordered AlGaInP MOVPE material examined in this study did not exhibit the intra-excitonic signals: this may be related to the fact that this material was doped and doping, in sufficient quantities, is known to prevent ordering. Excitonic signals were detected in doped ZnMgSSe material; however, they were notably weaker than those detected in the undoped ZnMgSSe barrier samples. The issues relating to the microstructure are complex, involving: doping, domain size and long and short -range ordering. The two-dimensional nature of the antiphase boundaries may account for the observed linear dependence of the exchange splitting observed in the MBE-grown AlGaInP material and the presence of impurity dopants may be responsible for the absence of excitonic signals in the partially ordered p-type MOVPE material. However, given the ad hoc nature of the samples examined and the current level of knowledge concerning the alloy microstructure, it is not possible to differentiate between the various contributing factors and identify with certainty the origin of localisation. It is therefore apparent that the determination of the detailed microstructure is essential in order to obtain a complete understanding of these alloys.

It is evident that SFRS spectroscopy is now a well established technique in the study of electron, hole and excitonic features in binary, ternary and quaternary wide-bandgap II-VI and III-V alloys. SFRS has played a decisive role in augmenting investigations of material issues involved with growth and doping. Fundamental to the success of the technique is the highly resonant nature of the process and the consequent selectivity, which has enabled the precise determination of the excitation energy of the centre under investigation, the determination of important bandstructure parameters and the strain splitting in the epilayer to be determined in small sample volumes. Furthermore, the ability to determine the excitonic exchange energy, analysis of anisotropic hole identifying signals and the determination of small strains, coupled with the ability to obtain spectral information on a scale much finer than the inhomogeneous PL linewidth in alloys systems, make SFRS a powerful tool in the investigation of the epitaxially grown latticed matched heterostructures essential for device fabrication.

To interpret the spectroscopic results presented in this thesis required a thorough understanding of the fundamental properties of the materials involved. The $\boldsymbol{k \cdot p}$ theory has provided an essential insight into the nature of the binary, ternary and quaternary semiconductor alloys and has proved successful in predicting their behaviour, thus providing a rigorous test of the $\boldsymbol{k \cdot p}$ bandstructure theory and confirming the validity of applying the method to wide-bandgap alloys.

The nature of excitonic localisation unites the somewhat disparate elements of this thesis. This localisation may take place via excitons binding to impurity centres, as predominantly occurs in binary alloys, or as has been argued, by exciton localisation at potential fluctuations in ternary and quaternary alloys. Compelling evidence has been presented to justify the latter assertion, indicating that the magneto-optical signals observed are indeed derived from intra-excitonic transitions produced by excitons weakly localised at potential fluctuations. Crucially, analogous features were observed in two distinct alloy systems, indicating that the observed phenomena are indeed a general feature of alloy systems.

References

[Baranovskii] S.D. Baranovskii and A.L. Efros, Sov. Phys. Semicond. **12** (1978) 1328

[Zunger] A. Zunger and S. Mahajan, '*Atomic Ordering and Phase Separation in Epitaxial III-V Alloys in Handbook on Semiconductors*', Eds. T. Moss and S. Mahajan, vol. 3, ch. 19, (Elsevier Science, Amsterdam, 1994)

Appendix A – Group tables

Table A1 Character table and basis functions for T_d.

T_d	E	$\overline{E}$	$8C_3$	$6\overline{S}_4$	$3C_2$ / $3\overline{C}_2$	$6S_4$	$6\overline{S}_4$	$6\sigma_d$ / $6\overline{\sigma}_d$	Basis
Γ_1	1	1	1	1	1	1	1	1	R or xyz
Γ_2	1	1	1	1	1	-1	-1	-1	$S_x S_y S_z$
Γ_3	2	2	-1	-1	2	0	0	0	$(2z^2-x^2-y^2)$, $\sqrt{3}(x^2-y^2)$
Γ_4	3	3	0	0	-1	1	1	-1	S_x, S_y, S_z
Γ_5	3	3	0	0	-1	-1	-1	1	x, y, z
Γ_6	2	-2	1	-1	0	$\sqrt{2}$	$-\sqrt{2}$	0	$\phi(1/2, -1/2)$, $\phi(1/2, 1/2)$
Γ_7	2	-2	1	-1	0	$-\sqrt{2}$	$\sqrt{2}$	0	$\Gamma_6 \times \Gamma_2$
Γ_8	4	-4	-1	1	0	0	0	0	$\phi(3/2, -3/2)$, $\phi(3/2, -1/2)$ $\phi(3/2, 1/2)$, $\phi(3/2, 3/2)$

Table A2 Multiplication table for T_d.

Γ_1	Γ_2	Γ_3	Γ_4	Γ_5	Γ_6	Γ_7	Γ_8	
Γ_1	Γ_2	Γ_3	Γ_4	Γ_5	Γ_6	Γ_7	Γ_8	Γ_1
	Γ_1	Γ_3	Γ_5	Γ_4	Γ_7	Γ_6	Γ_8	Γ_2
		$\Gamma_1+\Gamma_2+\Gamma_3$	$\Gamma_4+\Gamma_5$	$\Gamma_4+\Gamma_5$	Γ_8	Γ_8	$\Gamma_6+\Gamma_7+\Gamma_8$	Γ_3
			$\Gamma_1+\Gamma_3+\Gamma_4+\Gamma_5$	$\Gamma_2+\Gamma_3+\Gamma_4+\Gamma_5$	$\Gamma_6+\Gamma_8$	$\Gamma_7+\Gamma_8$	$\Gamma_6+\Gamma_7+2\Gamma_8$	Γ_4
				$\Gamma_1+\Gamma_3+\Gamma_4+\Gamma_5$	$\Gamma_7+\Gamma_8$	$\Gamma_6+\Gamma_8$	$\Gamma_6+\Gamma_7+2\Gamma_8$	Γ_5
					$\Gamma_1+\Gamma_4$	$\Gamma_2+\Gamma_5$	$\Gamma_3+\Gamma_4+\Gamma_5$	Γ_6
						$\Gamma_1+\Gamma_4$	$\Gamma_3+\Gamma_4+\Gamma_5$	Γ_7
							$\Gamma_1+\Gamma_2+\Gamma_3$ $+2\Gamma_4+2\Gamma_5$	Γ_8

Appendix B – Sample details

Sample	Source	Growth method	Layer thickness	Main dopant
1389	Regensburg	MOVPE	0.6 μm	*N*
ZSe 13	Lecce	MOVPE	0.8 μm	N
EPI-649	Valbonne	MBE	2.2 μm	P
N116	NEWI	MOVPE	1.8 μm	N
K106	Berlin	VPT	3x3x1 mm	Li
K5	Berlin	VPT	2x2x1 mm	Li
K52	Berlin	VPT	3x1x1 mm	*Li*
U117	Berlin	VPT	3x1x1 mm	Li
K79a	Kyoto	MOVPE	2.5 μm	N
S207	Bremen	MBE	0.5 μm	Cl & N

Table B1 Sample details of ZnSe bulk and epitaxial material, grown by various methods including vapour phase transport (VPT).

Sample	N_D (cm^{-3})	$N_D - N_A$ (cm^{-3})	GaP Cell Temperature(^{0}C)	-ray rocking curve FWHM (arc s)
S116	$1x10^{15}$	$3x10^{14}$	660	-
S117	$1x10^{17}$	$3x10^{16}$	800	170
S119	$1x10^{19}$	$3x10^{18}$	980	190

Table B2. Details of co-doped ZnSe:Ga:P epilayers referred to in section 4.1. The specimens were grown in Bremen by MBE, with an epilayer thickness of 1.7 μm.

Sample	$Zn_{1-x}Mg_xS_ySe_{1-y}$ x	y	$N_A - N_D$ ($10^{17}cm^{-3}$)	Thickness (μm)	Rocking curve FWHM(arc s)	Growth method
MS-p327	0.14	0	~2	1	661	MBE
ZS-p219	0	0.27	~2	1	463	MBE
ZS-p220	0.10	0.22	~1	1	210	MBE
S54	0.07	0.12	-	-	-	MOVPE

Table B3 p-type ZnMgSSe epilayers doped with nitrogen. All samples grown in Bremen, with the exception of MOVPE specimen which was grown in Kyoto.

Sample	$Zn_{1-x}Mg_xS_ySe_{1-y}$ Barrier x	Barrier y	Barrier thickness (nm)	ZnSe SQW width (nm)	Growth technique
S0086	0.11	0.20	400	20	MBE
S0085	0.11	0.20	400	10	MBE
S0084	0.11	0.20	400	5	MBE

Table B4 ZnSe single quantum wells (SQW) with undoped ZnMgSSe barriers. Grown at Bremen on GaAs substrates overgrown with a GaAs buffer layer and a 5 nm ZnSe buffer layer.

Sample	Aluminium composition	Substrate Orientation	Doping / $\times 10^{17}$ cm^{-3}	Grower	Growth Technique
S830	0.0	0	undoped	Sharp	MBE
S837	0.0	7	undoped	Sharp	MBE
S8310	0.0	10	undoped	Sharp	MBE
S83	0.0	15	undoped	Sharp	MBE
S271	0.2	15	undoped	Sharp	MBE
S167	0.3	10	undoped	Sharp	MBE
S870	0.4	0	undoped	Sharp	MBE
S87	0.4	15	undoped	Sharp	MBE
S88	0.5	15	undoped	Sharp	MBE
S89	0.7	15	undoped	Sharp	MBE
S90	0.85	15	undoped	Sharp	MBE
S85	1.0	15	undoped	Sharp	MBE
52539C	0.0	-	1-2	EPI	MOVPE
52541C	0.18	-	1-2	EPI	MOVPE
52542C	0.25	-	1-2	EPI	MOVPE
52543C	0.31	-	1-2	EPI	MOVPE
52580C	0.39	-	1-2	EPI	MOVPE
52581C	0.46	-	1-2	EPI	MOVPE

Table B5 MBE and MOVPE $(Al_xGa_{1-x})_{0.52}In_{0.48}P$ epilayers. The undoped MBE material was produced by Sharp Laboratories of Europe Ltd. The p-type MOVPE material was produced by Epitaxial Products International Ltd (EPI) and doped using Zn.

Appendix C – AlGaInP Vibrational Raman Spectra

The compositional dependence of the vibrational Raman spectra in GaInP has been extensively studied[1-3]; however, AlGaInP has received less attention[4,5]. Results obtained from vibrational Raman studies are presented here for $(Al_xGa_{1-x})_{0.52}In_{0.48}P$ epilayers grown by MBE, in the composition range $0<x<0.5$; similar results were also obtain for the MOVPE material.

Presented in figure C1 are the 'out-going' vibrational Raman spectra, normalized to the InP-like mode intensity, exhibited by MBE grown $(Al_xGa_{1-x})_{0.52}In_{0.48}P$ at 1.5 K. The spectra were obtained by direct resonant excitation of the excitonic emission band. The Raman peaks at 449, 385 and 365 cm^{-1} correspond to AlP, GaP and InP-like LO-phonon modes[4,5], respectively. The weaker peak at 329 cm^{-1} has been identified as the InP-like TO-phonon mode[5] and is normally forbidden by the Raman

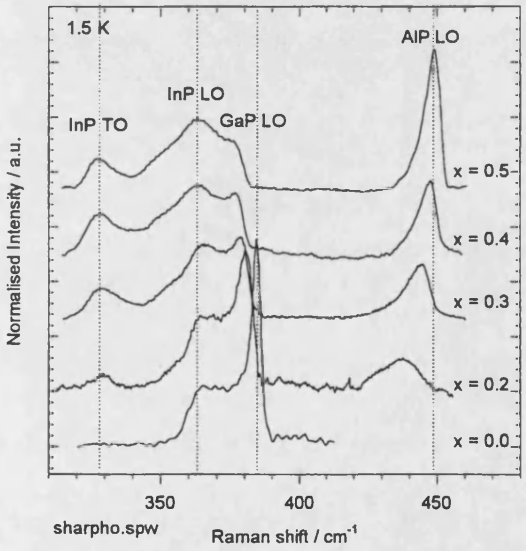

Figure C1 Low temperature resonant vibrational Raman Spectra of MBE $(Al_xGa_{1-x})_{0.52}In_{0.48}P$ epilayers, for the compositions indicated on the diagram.

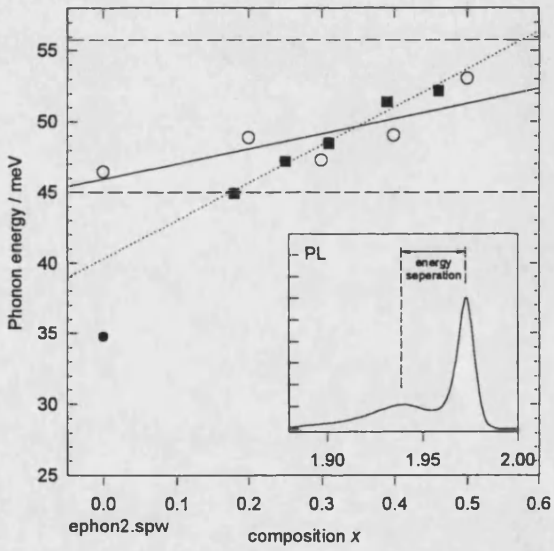

Figure C2 Compositional dependence of the energy separation between the dominant and unidentified PL feature (see inset), for MBE (cirlces) and MOVPE (squares) epilayers.

selection rules in backscattering geometry for zincblende-type crystals; however, its presence is attributed to the relaxation of the ***k***-conservation law due to alloy disorder. The AlP-like and InP-like modes display a distinctive asymmetric lineshape, which in some studies has been correlated with long-range CuPt-type ordering[6] and explained[7] in terms of the zone folding of the *L* point phonon leading to the formation of the shoulder on the low energy side of the zone centre phonon mode. However, this asymmetric lineshape is also observed in ZnSe-based materials[8-10], for example the ZnSe-like phonon mode in ZnMgSe (inset figure 3.2.1) exhibits a distinct asymmetry,

despite the fact that these alloys do not manifest a strong tendency to exhibit long-range order. In the latter case the low energy tail has been attributed to substitutional disorder in the so-called spatial correlation model[11]. According to this model breakdown of the k-selection rule occurs, due to the presence of substitutional disorder, enabling contributions to be made from modes of the LO branch whose wavevector is in the vicinity of $k = 0$[12].

Figure C2 shows the compositional dependence of the energy difference between the peak position of the dominant excitonic emission in the PL band and the weaker feature to lower energy (see inset), for MBE (open circles) and MOVPE (filled circles) grown $(Al_xGa_{1-x})_{0.52}In_{0.48}P$ material. The energy difference displays a linear dependence with composition for both types of material, within the energy ranges corresponding to the AlP-like and InP-like mode energies of 56 and 45 meV, respectively. The linear dependence is in accord with the change in intensity of the respective phonon modes with composition, as shown in figure C1, implying that the lower energy PL feature is a phonon replica. Observation of an analogous feature in the PL spectra of the ZnMgSSe alloy separated by an energy corresponding closely to the dominant ZnSe-like mode, supports this identification.

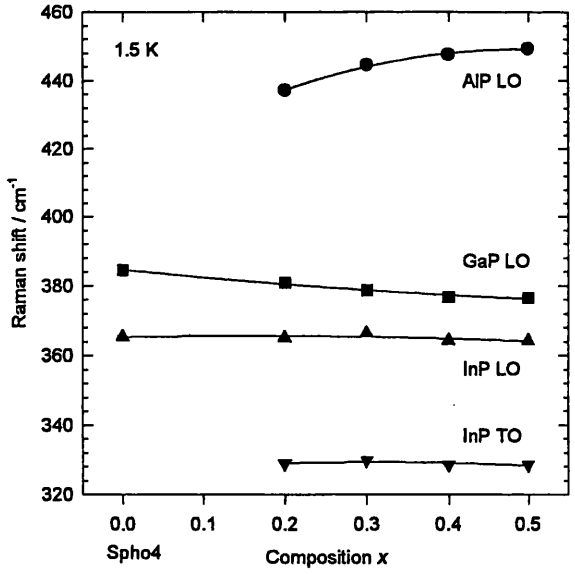

Figure C3 Compositional dependence of phonon modes

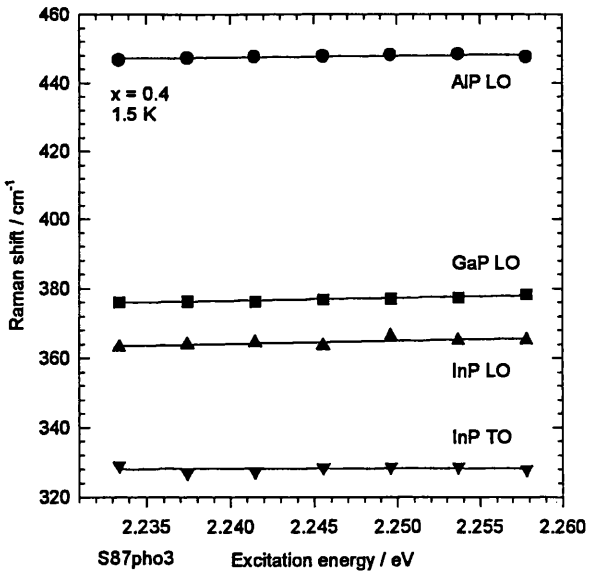

Figure C4 Excitation dependence of phonon modes

The compositional dependence of the observed modes is presented in figure C3. It is evident from this figure that the pronounced dependence of the AlP and GaP-like modes provide an opportunity to determine the composition from the Raman shift of the modes. Unfortunately, for the technologically more significant wider bandgap compositions, $0.3<x<0.5$, the variation is small. Therefore, accurate determination of

composition in this important range may be impracticable using vibrational Raman spectroscopy.

Finally, in an endeavour to determine if compositional variation was directly responsible for the broad excitonic linewidth, vibrational Raman scattering as a function of excitation energy was attempted in resonance with the excitonic emission band, for the specimen with x = 0.4. The results are shown in figure C4. No discernable variation was detected, indicating that vibrational modes are either independent of excitation energy or that the change in composition is too small to be detected using this method. Considering the small variational dependence of the mode Raman shift as a function of composition the latter point seems likely.

The origin of the asymmetric phonon mode lineshape is currently ambiguous and interpretation of vibrational Raman spectra will remain contentious until this issue is resolved. Difficulties in AlGaInP are further compounded, because for the technologically important compositions the rate of change of mode frequency with composition is small, indicating that vibrational Raman studies may not be useful for these compositions. It is evident that the correct interpretation of the Raman spectra is dependent on a more complete understanding of the microstructure of the alloy.

[1] R. Beserman, C. Hirlimann, M. Balkanski and J. Chevallier, Semicond. Sci. Comm. **20** (1976) 485

[2] M. Kondow and S. Minagawa, J. App. Phys. **64** (1988) 793

[3] G.C. Jiang, Y Chang, L.B. Chang, Y.D. Juang, W.L. Lu, L.S. Lu and K.H. Chang, J. App. Phys. **78** (1995) 2886

[4] M. Kondow, S. Minagawa and S. Satoh, App. Phys. Lett. **51** (1987) 2001

[5] M. Kubo, M. Mannoh, Y. Takahashi and M. Ogura, APL **52** (1988) 715

[6] M.P. Halsall, A.D.F. Dunbar and U. Bangert, J. App. Phys. **85** (1999) 199

[7] F. Alsina, N. Mestres, J. Pascual, C. Geng, P. Ernst and F. Scholz, PRB **53** (1996) 12994

[8] E. Oh, S.D. Lee, H.D. Jung, M.D. Kim, H.S. Park, B.J. Kim and T.I. Kim, 22nd Int. Symp. Compound. Semiconductors, Korea, IOP Publishing Ltd 1996

[9] K. Hayashi, N. Sawaki and I. Akasaki, Jap. J. Appl. Phys. **30** (1991) 501

[10] E. Oh and A.K. Ramdas, J. Electronic Materials **23** (1994) 307

[11] P. Parayanthal and F. Pollack, Phys. Rev. Lett. **52** (1984) 1822

[12] B. Jusserand and J. Sapriel, Phys. Rev. B **24** (1981) 7194

Appendix D – Lithium doped ZnSe

It was reported in section 4.2 that two of the lithium-doped crystals, samples U17 and K5, exhibited additional signals in resonance with the D^0X and FE, which to the best of our knowledge have not previously been reported in the literature. In this appendix the SFRS results are presented and a tentative interpretation is given in terms of an excitonic exchange interaction.

High field SFRS spectra[1] obtained in resonance with D^0X from the bulk lithium-doped ZnSe sample U17 are presented in figure D1. At 14 Tesla five previously unreported features are observed, signals A to E. A further signal, designated F (not shown), is also observed to higher Raman shift than signal C. The observation of anti-Stokes lines for signals D and E suggests that these signals were not an artefact of the measurement process; however, it is difficult to discern any systematic trend with so few data points. The FWHM of signals D and E is 0.42 ± 0.12 cm^{-1} which is

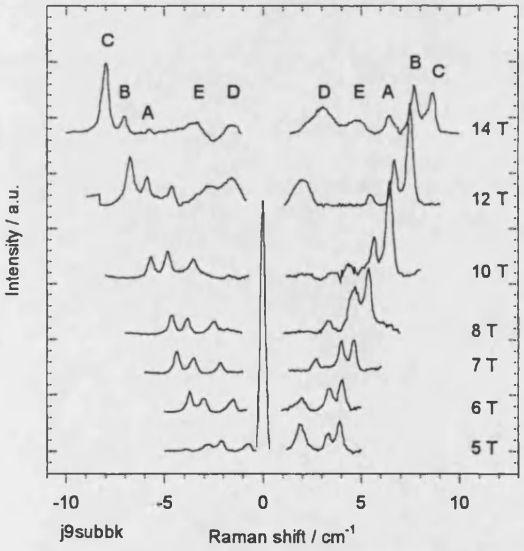

Figure D1 High field Stokes and anti-Stokes SFRS spectra in resonance with the neutral donor bound exciton, excitation energy 2.7978 eV. Arrows indicate the position of Al and Ga D^0X.

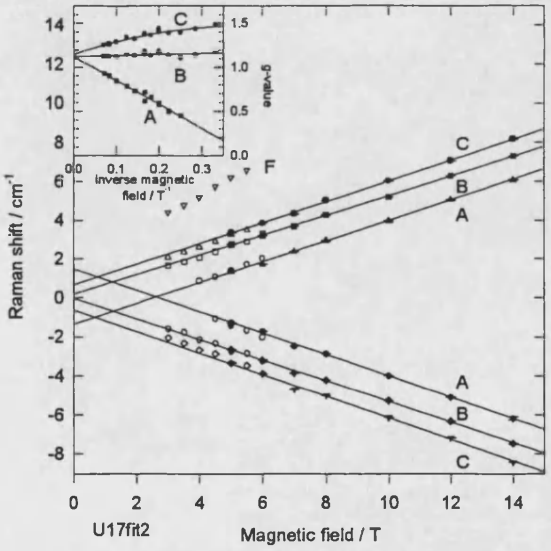

Figure D2 Magnetic field dependent data. Solid lines linear regression fit to data. Inset shows Raman shift divided by field strength plotted against inverse magnetic field.

significantly broader than the FWHM of signals A to C of 0.18 ± 0.03 cm^{-1}. No SFRS signals were observed in zero field. The fitted data from the SFRS spectra are presented in figure D2. Extrapolation of the high field data (solid lines) clearly demonstrates that signals A, C and F do not converge to the origin, whilst signal B behaves in accordance with equation (1.38). The inset, figure D2, shows the Raman shift of each data point divided by its magnetic field strength plotted against the inverse magnetic field (the solid lines are a guide to the eye). From this inset it is

clear that signal B is independent of the magnetic field, whilst signals A and C are manifestly field dependent. Furthermore, extrapolation of the data indicates that all three lines converge at the free electron g-value in the high field limit.

The SFRS resonance profile, figure D3, is reproduced here for the D^0X and FE regions, with intensity plotted on a logarithmic scale. The data points are fitted using equation (1.39). In the vicinity of D^0X, signal B could not be fitted satisfactorily with a single peak, instead two peaks were required. The two peaks correspond closely to the energetic positions of the Al and Ga D^0X lines[2], indicated in the figure by arrows. The presence of Al and Ga donor impurities in these samples was established in earlier work[3]. The resonance position of signals A and C is, to within the experimental resolution, also coincident with that of the Ga D^0X line at 2.7978 ± 0.0001 eV. All three SFRS signals appear in resonance with the FE.

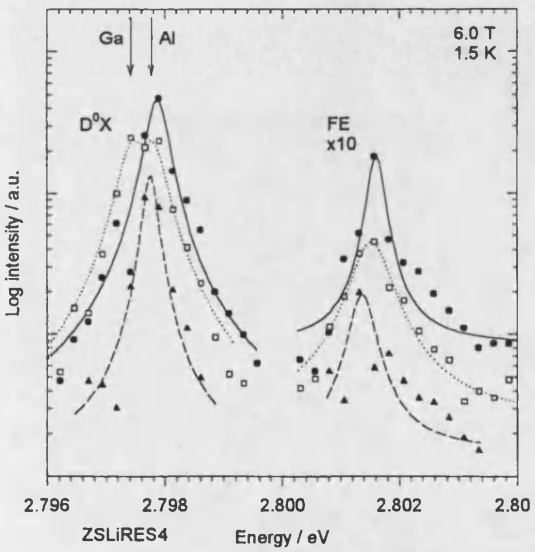

Figure D3 Resonance profile of SFRS signals in the vicinity of neutral donor bound exciton and free-exciton. Triangles, squares and circle correspond to signals A, B and C, respectively.

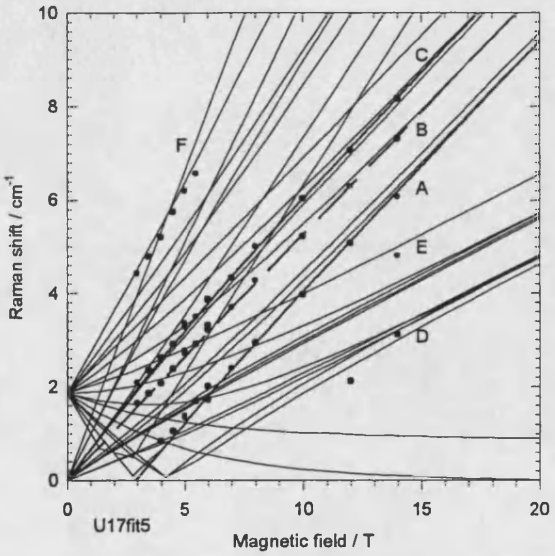

Figure D4 Stokes field dependent data fitted according to the excitonic model, equation 5.1 (dotted and solid lines). Magnetic field dependence of electron SFRS in resonance with D^0X (dashed line).

The field dependent behaviour of signal B enable it to be attributed to shallow donor SFRS, however, the unusual field dependent behaviour of signals A and C rules out their respective interpretations as SFRS signals stemming from a electrons or holes bound to neutral centres or electron SFRS from a deep compensating donor. Therefore, the origin of these signals requires further investigation.

The model required to describe the above observations must introduce an energy splitting of a few tenths of an meV; several interactions are capable of producing such a splitting, these are: strain, coulombic, crystal field and exchange interactions. Angle

dependent measurements, figure 4.2.7, indicate that the strain in these bulk samples is negligible and therefore the strain splitting model cannot be invoked. It is equally unlikely that such a small splitting would result from a coulombic interaction, since the exciton binding energy is 19 meV in ZnSe[4], unless the interaction exclusively involved the higher excited states. The crystal field interaction[5] lifts the fivefold degeneracy of the $F = 2$ manifold without splitting the $F = 1$ manifold, but shifts it with respect to the $F = 2$ manifold, introducing a crystal field splitting, Δ_{cf}, between the $F = 1$ and $F = 2$ states. The Hamiltonian describing the $F = 2$ manifold can be expressed in the following form[6]:

$$H_{cf} = \Delta_{cf}\left[35J_z^4 - 15J_z^2 + 36I + \frac{5}{2}\left(J_+^4 + J_-^4\right)\right] \qquad \text{(D.1}$$

However, the above Hamiltonian introduces pronounced anisotropic angular dependence as a function of the magnetic field orientation; this behaviour was not observed experimentally, figure 4.2.7. Therefore, serious consideration must be given to the exchange interaction model. The simplest exchange interaction model capable of yielding electron g-values at high fields is that of two coupled, but spatially separate, centres of spin 1/2 with identical, isotropic g-values. However, it can be shown that this model does not lead to field dependent g-values. The next level of complexity describes an exchange-coupled electron-hole pair, equation 5.1. Figure D4 shows the Stokes SFRS transitions determined using the excitonic model, dotted and solid lines, for an isotropic exchange interaction in the absence of strain, the dashed line corresponding to the spin-flip of a electron bound to a neutral donor complex, signal B, is also included. The parameters required to obtain this fit were g_e = 1.14, g_h = 0.56 and δ_1 = 0.11 meV, which are consistent with those previously determined (see sections 3.1 and 4.2). Thus the data is interpreted as the superposition of the commonly observed spin-flip of an electron bound to a neutral donor complex together with excitonic SFRS transitions.

The excitonic model provides a reasonable description of the data, particularly the high field data, and has the scope to account for all of the lines present. However, the solution is not necessarily unique and does not identify the centre responsible for the excitonic interaction. Consideration of this latter point could be given to interactions involving, the two observed donor species, interstitial lithium donors[7], isoelectronic impurities[8] and even excited states of A^0X or ionised donor centre[9]. Further, models

involving additional particles or high-excited states[10] cannot be ruled out, but their investigation is beyond this present work.

[1] private communication O.Z. Karimov

[2] M. Isshiki, T. Kyotani, K. Masumoto, W. Uchida and S. Suto Phys. Rev. B **36** (1987) 2568

[3] U. W. Pohl, G. H. Kudlek, A. Klimakow and A. Hoffmann, J. Cryst. Growth **138** (1994) 385

[4] M. Isshiki, K.S. Park, Y. Furukawa and W. Uchida, J. Cryst. Growth **117** (1992) 410

[5] P.J. Dean and R.A. Faulkner, Phys. Rev. B **185** (1969) 1064

[6] H. Watanabe, "*Operator Methods in Ligand Field Theory*", (Prentice-Hall 1966)

[7] G.F. Neumark, Phys. Rev. B **37** (1988) 1778

[8] K. Shahzad, K.S. Jones, P.D. Lowen and R.M. Park, Phys. Rev. B **43** (1991) 9247

[9] J.L. Merz, H. Kukimoto, K. Nassau and J.W. Shiever, Phys. Rev. B **6** (1972) 545

[10] U. W. Pohl, D. Wiesmann, G. H. Kudlek, B. Litzenburger and A. Hoffmann, J. Cryst. Growth **159** (1996) 414